PHOTODEGRADATION OF TETRACYCLINE AND TRIMETHOPRIM IN WASTEWATER USING SENSITIZED GRAPHITE CARBON NITRIDE ZINC FERRITE COMPOSITE

By

Mutuma Humphrey Samuel

A Thesis Submitted to the School of Engineering, Department of Chemical & Process Engineering in Partial Fulfillment of the Requirements for the Award of the degree of Master of Science in Chemical Engineering

Moi University

2023

DECLARATION

Declaration by Candidate

I declare that this thesis is my original work and has not been submitted for the award of a degree in any other university. No part of this thesis may be reproduced without the prior written permission of the author and/or Moi University.

Signed:_____ Date:_____

Mutuma Humphrey Samuel

MSC/5519/21

Declaration by the Supervisors

This thesis has been submitted for examination with our approval as university supervisors.

Signed:_____ Date:_____

Prof. Eng. Milton M'Arimi

Department of Chemical & Process Engineering,

School of Engineering,

Moi University, Kenya

Signed:_____ Date:_____

Dr. Cleophas Achisa Mecha

Department of Chemical & Process Engineering,

School of Engineering,

Moi University, Eldoret, Kenya

DEDICATION

This project is dedicated to my dear wife Damaris Kabirithu for the emotional support, encouraging words and understanding as I undertook the challenging task of research. Moreover, I dedicate this project to my daughter Ladasha Kairuthi for bearing with me as I devoted a lot of time running experiments.

Finally, I dedicate this work to the department of Chemical Engineering, Moi University for the material, technical and moral support during the course of research

ACKNOWLEDGEMENTS

I thank the Almighty God for guiding me throughout this research journey. Truly, his grace has been sufficient in enabling the completion of this work. Glory be to God!

My sincere gratitude and admiration for my project supervisors: Dr. Cleophas Achisa and Prof. Eng. Milton Arimi. Their unwavering support, guidance and positive criticism at every phase of the project has been highly exceptional. Respect to all lecturers in Chemical engineering department, their inputs and recommendations heavily influenced this project. Special thanks to Mr. Paul Lagat the laboratory technician, Chemical & Process Engineering, Moi University. His assistance in the lab was very helpful in materialization of this project.

Special token of appreciation to Kenya's National Research Fund [Grant number 2/MMC/825] for funding this project under the Sustainable Technologies for Potable Water Treatment programme. Honestly, without the funding implementation of this research project would have been seriously hampered. I am also indebted to Nairobi Technical Training Institute, Deputy Principal academic Purity Mutea for allowing me to use the workshops for equipment fabrication.

Finally, many thanks to my collegues and friends from various department who I met in the course of the studies. I highly appreciate their encouragement, comradeship and motivation. Without you the journey would have been lonely.

ABSTRACT

The presence of emerging contaminants such as antibiotics in wastewaters pose a great challenge in water reuse. Multicomponent photocatalysts such as $ZnFe_2O_4$-g-C_3N_4 (ZF-GCN) are a promising alternative for complete mineralization of antibiotics at mild conditions. The effect of dye-sensitizers in improving the performance of photocatalysts is not adequately assessed and limited knowledge exists on the removal of antibiotics in real wastewater matrices. The main objective of this study was to evaluate the degradation of trimethoprim and tetracycline using Eosin Y sensitized ZF-GCN in a solar parabolic trough reactor. The specific objectives were to: synthesize and characterize the physical and chemical properties of ZF-GCN photocatalyst; determine optimum parameters for degradation of synthetic water containing antibiotics; and evaluate the photodegradation of antibiotics in real wastewater (RWW) and assess the effect of competing ions. The study synthesized four composites of ZF-GCN at 0, 5, 15 and 25wt% loading of the $ZnFe_2O_4$ using a three-step procedure as follows: direct annealing of melamine to yield bulk g-C_3N_4 which was thermally and ultrasonic exfoliated to yield g-C_3N_4 nanosheets; a hydrothermal-precipitation reaction of g-C_3N_4, $FeCl_3.6H_2O$, $ZnCl_2.2H_2O$ and ammonia to yield ZF-GCN; dye sensitization of resultant composite with Eosin Y dye using a mixing-adsorption method. The photocatalysts were characterized using: X-Ray diffraction (XRD), scanning electron microscope-energy dispersive spectroscopy (SEM-EDX), UV-vis analysis and Pl-spectra. The composites exhibited the structural and crystalline phases of the pure photocatalysts on XRD and FTIR studies. Furthermore, the composites displayed a reduction in bandgap and suppressed charge recombination in the UV-vis and PL-spectra, respectively. This was evidence for successful creation of heterojunction. The following variables were investigated: pollutant dosage (10-25mg/l), catalyst dose (0.4-1.2g/l) and pH (4-10). The effect of competing ions was studied at various salt concentrations (100, 300, 500mg/l) in real wastewater. The central composite design was used in generating two quadratic polynomial models for degradation and TOC removal as the responses. The predicted R^2 values for both models was >0.95, which signified their high accuracy in predicting the responses. The analysis of variance results revealed that all the factors were highly significant in affecting degradation and TOC removal for tetracycline while for trimethoprim, only pollutant dose and catalyst dose were the most significant factors. The optimum parameters for trimethoprim was (pollutant dose=10mg/l, pH = 7.19, catalyst = 0.72g/l, Degradation=89.52%, TOC=49.12%) while for tetracycline was (pollutant dose=10mg/l, pH=6.88, catalyst=0.737g/l, Degradation=96.07%, TOC=65.25%). Sulphate ions had the highest inhibition effect on tetracycline degradation among the three anions. Hydroxyl radical scavenging and competition for catalyst active sites could be the reason. In conclusion, a dye-sensitized photocatalyst is a potentially effective method for eliminating antibiotics in different wastewater matrices. However, it is recommended that a pretreatment step for anion removal be included in the PTR system to reduce their scavenging effects when treating real wastewater.

TABLE OF CONTENTS

LIST OF TABLES

LIST OF FIGURES

ABBREVIATIONS

ANOVA	Analysis of Variance
AOP	Advanced Oxidation Process
CCD	Central composite design
COD	Chemical oxygen demand
EDS	Energy dispersive spectroscopy
EY-25%ZF-GCN	Eosin Y sensitized photocatalyst
EPA	Environmental protection agency
F-value	Fisher value
FTIR	Fourier transform infrared spectroscopy
FTU	Formazine turbidity unit [1FTU = 1NTU]
LC/MS	Liquid chromatography mass spectrometry
KEBS	Kenya Bureau of Standards
NEMA	National Environmental Management Authority
NOM	Natural organic matter
pKa	Acid dissociation constant
PL	Photoluminescence spectra
PTR	Parabolic trough Reactor
RSM	Response surface methodology
RWW	Real wastewater
SEM-EDX	Scanning electron microscope
SW	Synthetic wastewater
TMP	Trimethoprim
TTC	Tetracycline
TOC	Total Organic Carbon
UNEP	United Nations Environmental Programme
UWWTP	Urban Wastewater treatment plant
WWTP	Wastewater Treatment Plant
WHO	World Health Organization
ZF-GCN	Zinc Ferrite Graphite carbon nitride

CHAPTER 1

INTRODUCTION

1.1 Background of Study

Currently, the world faces acute shortage of clean water for both domestic and commercial uses. Despite of the popular opinion that 70% of total earth surface is covered by water, only 2.5% of the world's water is freshwater and only 0.25-0.49% of this can be directly consumed (Suresh et al., 2021). The leading factors to water shortages include; climate change, intensification of agriculture, population increase and rapid industrialization (Kageche & Kipkirui, 2020). The existing water bodies face uncontrolled release of harmful substances, which make them unusable. Estimates by the United Nations put by 2030, 250 million Africans will not have adequate water to survive on (Guide, 2005). Currently, sub-Saharan Africa lags behind other regions in accessibility to clean water at 10-40 liters of water per person against 600 liters per person in Europe and America. Within Kenya there is water scarcity and poor waste disposal, with only a sewerage cover of 17% (K'oreje et al., 2020). Therefore, water scarcity is a major concern in Kenya.

Recently, some contaminants that in the past were not monitored have brought great concern, and these pollutants have been labeled as "emerging pollutants." According to the EPA, emerging pollutants are any man-made or naturally occurring compound that is not frequently monitored or regulated by the existing environmental bodies and has suspected adverse effects to humans and the ecosystem (Kageche & Kipkirui, 2020). In Kenya, the emerging pollutants are generated mainly by pharmaceutical products, personal care products, and new generations of pesticides (Otieno et al., 2020). Pharmaceuticals are the most notorious among pollutants of emerging concern. Furthermore, they have been linked to increasing the resistance of bacteria against

drugs. Besides, some have been noted to disrupt the endocrine systems in humans and animals (Kidd & Zoeller, 2012).

The fate of pharmaceuticals is poorly understood. However, their daily use makes them environmentally persistent (Olatunde et al., 2020). Antibiotics will be explored in this study due to their frequent detection in wastewater and their common use in the treatment of infectious diseases (Ngigi et al., 2020). Furthermore, their presence at sub-inhibitory ranges in aquatic systems has been frequently linked with the transmission of antibiotic-resistant genes and the ever-increasing bacterial resistance against antibiotics (Mpatani et al., 2021). Hence, the occurrence of pharmaceutically active compounds at concentrations below their sub-inhibitory levels may promote bacterial mutations (Kairigo et al., 2020). Unfortunately, no regulations exist on the maximum contaminant limits for pharmaceuticals by both international bodies (WHO, EPA) and national entities (NEMA, KEBS) (Kamba et al., 2017; Tiejun, 2022).

Among the antibiotics, trimethoprim and tetracycline are selected for this study due to their frequent detection in aquatic systems at high concentrations and their low degradation rates by WWTP (Koreje et al., 2016; Kairigo et al., 2020; Muriuki et al., 2020; Ngumba et al., 2016). For instance, a study carried out on wastewater treatment plants in Nyeri, Meru and Machakos, found high mean effluent concentration of trimethoprim and tetracycline in the order of 60.7µg/l and 15.8µg/l respectively (Muriuki et al., 2020). The possible reason for the low removal efficiencies could be due to their high solubility in water, complex molecular structure, hence resistance to biological and chemical treatments and their polar nature, which makes it difficult for their adsorption in the soil (Feng, 2014). Furthermore, trimethoprim has broad-spectrum uses in treating various human infections. Hence huge volumes are excreted

daily by the general population (Mpatani et al., 2021). On the other hand, tetracycline is a multipurpose antibiotic extensively applied for treating infections caused by gram-negative and gram-positive bacteria in both humans and animals (Balakrishnan et al., 2023). This antibiotic can only be partially metabolized in the human body, is chemically stable in water matrices, and has antibacterial properties which hinder its elimination by biological/chemical systems (Deng et al., 2018; Li et al., 2022a). Therefore, the development of an efficient treatment method for these two pollutants remains a priority.

Advanced oxidation processes (AOPs) are increasingly explored as alternatives to conventional treatment plants for eliminating emerging pollutants. The AOPs generate powerful hydroxyl/oxide radicals that can mineralize recalcitrant pollutants to yield carbon dioxide and water (Khan et al., 2020). Besides, these processes generate less sludge than conventional processes in case of partial mineralization of pollutants (Koreje et al., 2016). Various AOP processes exist namely, hydrogen peroxide, ozone, ultraviolet light, photocatalysis, Fenton process, and ultra-sonication (Fast et al., 2017). However, despite their high effectiveness and powerful nature, AOPs still suffer from several limitations. These include: increased costs due to the use of large volumes of reagents, safety risks during production and transport of some reagents like ozone, and high energy consumption among others (Khan et al., 2020).

Heterogenous photocatalysis is a promising advanced oxidation process capable of mineralizing emerging pollutants using visible light at mild conditions of temperature, pressure, and pH (Abeer., 2022). The reaction involves a solid semiconductor material that is excited by light photons, which generates electron/hole pairs that diffuse to the surface. Photogenerated electrons are scavenged by O^{2-} to generate superoxide radicals.

Furthermore, the holes produced can directly oxidize water to produce •OH radicals, which directly attack and mineralize organic molecules (Berkani et al., 2021). Common semiconductors used include: metal oxides (TiO_2, CeO_2, ZnO, Cu_2O, In_2O_3, $BiVO_4$, WO_3), metal sulfides (ZnS, CuS, MoS_2), metal ferrites (Fe_3O_4, $ZnFe_2O_4$, $CoFe_2O_4$, $CuFe_2O_4$) and carbonaceous materials (Zhao et al., 2022). Among the metal semiconductors, TiO_2 is the most popularly used in photocatalytic applications due to its outstanding photocatalytic properties (Patel et al., 2021). However, since most photocatalysts are metal oxides there is an attempt to reduce the metal content in photocatalysts in order to reduce the potential risk of heavy metal pollution. Hence, non-metal semiconductors are increasingly explored.

Graphite carbon nitride (g-C_3N_4) is one of the potential photocatalysts due to its favorable properties such as; a moderate band gap energy, sensitive to visible light up to 460nm, a suitable conduction and valence band for oxidation, and is a metal-free n-type semiconductor (Ismael, 2020). The band gap energy of graphite carbon nitride is 2.7eV, and the energy location of its conduction and valence band is -1.1 and +1.6eV, respectively (Darkwah & Ao, 2018). Furthermore, it has the dual advantage of eliminating pollutants through a synergistic mechanism of adsorption and photocatalysis. Due to these desirable properties, g-C_3N_4 is a promising green photocatalyst. Nevertheless, previous studies using g-C_3N_4 for pollutant degradation have obtained unsatisfactory results due to limited optical response to visible light and poor photogenerated charge separation due to rapid recombination (Huong et al., 2023). One potential method of improving the photocatalytic activity of g-C_3N_4 is by constructing a heterojunction with a photocatalyst such as zinc ferrite.

$ZnFe_2O_4$ is a p-type semiconductor that belongs to the spinel ferrite family and has widely been investigated in visible light degradation of emerging pollutants (Chen et al., 2016; Rong et al., 2020). Its narrow bandgap of ~1.9eV ensures that it can utilize a wide spectrum of solar irradiation. Furthermore, the Fe^{3+} present in its structure reacts with peroxide in a Fenton-like process to yield hydroxyl radicals that decompose organic molecules. However, bare $ZnFe_2O_4$ still suffers from fast recombination of photogenerated charge and photo-corrosion effects in the presence of light, which decreases its photocatalytic performance (Sonu et al., 2021). Therefore, coupling a n-type semiconductor such as g-C_3N_4 to the p-type $ZnFe_2O_4$ will be an effective method of addressing the weaknesses faced by each photocatalyst. The created heterojunction works by creating an inbuilt electric field at the junction interface, which decreases the electron-hole pairs recombination by driving the respective charges in opposite directions which increases the redox potential of the photocatalyst (Chowdhury et al., 2021; Kumar et al., 2020). The resulting composite has desirable properties such as decreased charge recombination, extended visible light absorption, and enhanced photocatalytic activity (Palanivel et al., 2019; Vidyasagar et al., 2018).

Nevertheless, most previous studies have worked on exfoliation techniques and creating composites as the main modification for g-C_3N_4. This research has attempted to study the effect of dye sensitization on the best-performing $ZnFe_2O_4$/g-C_3N_4 composites. Dye sensitization is a promising approach since dye molecules can be excited at long wavelengths by visible light photons to produce electrons from its HOMO band (highest occupied molecular orbital), which is passed to its LUMO band (lowest unoccupied molecular orbital) and subsequently injected to the conduction band of the semiconductor (Diaz-angulo et al., 2019; Musa & Gaya, 2019). These injected electrons then react with adsorbed oxygen molecules on the surface of the photocatalyst to form

superoxide, hydroxyl and other active species (You, 2016). Eosin Y is an anthracene-based dye with a high optical absorption coefficient necessary for the absorption of visible light at long light wavelengths (Li et al., 2019). Furthermore, due to its low cost it can be used as a potential sensitizer.

1.2 Problem Statement

The United Nations sustainable development goal number six advocates for the availability and sustainable management of water resources and sanitation facilities (Guppy et al., 2017). However, Kenya risks failing to meet this goal because it is listed as a water scarce nation (United Nations, 2020), whose population has limited access to clean water. In Kenya, only 57% of the urban population and 51% of the rural population have access to safe water (Priority & Plan, 2022). The water scarcity problem in Kenya is further worsened by the elevated pollution levels of water bodies by both domestic and industrial sources. A considerable amount of these effluents consist of emerging pollutants, with pharmaceutical compounds, pesticides and personal care products being the most notorious (Kageche & Kipkirui, 2020). Recently, antibiotics have raised great concern due to their association with antibiotic-resistant bacteria and transmission of antibiotic resistance genes. The tertiary units of wastewater treatment plants in Kenya are mainly trickling bed filters and wastewater stabilization pans, which consequently have low efficiencies in eliminating target emerging pollutants (K'oreje et al., 2018; Muriuki et al., 2020). These deficiencies could be due to the complex organic structures of emerging pollutants and their existent in complex water matrices that tend to be resistant to biochemical treatment. Consequently, there is a need for the development of alternative post-treatment method for municipal wastewater to address these challenges. Heterogeneous photocatalysis is a promising advanced oxidation process that can be potentially effective in treating recalcitrant

antibiotics. This research seeks to exploit the synergistic effects of dye-sensitized zinc ferrite-graphite carbon nitride composite in degrading antibiotics. The advantage of combining the two semiconductors is that visible light can be utilized up to 600nm and a p-n heterojunction is created, enhancing charge separation. Therefore, abundant reactive oxygen species ($^{\bullet}O_2^-$, •OH) can be generated efficiently, and consequently more organic pollutants are degraded. Heterogeneous photocatalysis is beneficial compared to conventional methods since there is little usage of toxic chemicals and if complete pollutant degradation is achieved, no sludge will be generated (Hartmann et al., 2010).

1.3 Objectives

1.3.1 General Objective

The aim of this study was to evaluate the degradation of trimethoprim and tetracycline using visible light photocatalysis.

1.3.2 Specific Objectives

1. To synthesize $ZnFe_2O_4$-g-C_3N_4 photocatalyst and characterize its physical and chemical properties.
2. To determine optimum parameters: catalyst dosage, solution pH, initial pollutant concentration, and dopant loading for degradation of synthetic water containing trimethoprim and tetracycline.
3. To evaluate the photodegradation of the target contaminants in real wastewater and assess the effect of competing ions (SO_4^{2-}, Cl^-, NO_3^-).

1.4 Research Questions

1. What is the surface composition, structural nature, and morphological characteristics of the photocatalyst synthesized?

2. What are the optimum operating parameters of the photodegradation process?
3. What is the performance of the photocatalyst in the degradation of real wastewater under visible light irradiation?

1.5 Justification

The widespread detection of antibiotics in aquatic systems has generated great concern from environmental bodies. Residual amounts of antibiotics may increase the proliferation of antimicrobial drug resistance. Unfortunately, conventional water treatment plants have poor removal efficiencies for pharmaceutical residues and can be detected in concentrations ranging from ngL^{-1} to μgL^{-1} (Waleng & Nomngongo, 2022). These plants were initially designed to eliminate BOD, COD, and pathogens (Sgroi et al., 2018). Furthermore, pharmaceutical residues may have complex molecular structures; polar nature could be toxic to metabolic bacteria (Jia et al., 2022; Peng et al., 2023). Therefore, a solar-driven heterogenous photocatalytic system (PTR/$ZnFe_2O_4$-g-C_3N_4) is a promising alternative to conventional methods. This system is operated at mild conditions, has high mineralization rates, and is non-selective in degrading emerging pollutants (Gusain et al., 2020). Besides, the use of such systems could result in potential cost-savings considering the abundant solar light and cheap photocatalytic materials. Hence, such a project could appeal to environmentalist since the risk of anti-microbial proliferation posed by pharmaceutical residues is eliminated.

1.6 Significance of the Study

Sustainable development goal number 6 advocates for access to clean water and sanitation facilities. This work researched on solving this goal by studying the removal of antibiotics from synthetic and real wastewater matrices using a solar reactor. Regression models were developed for both pollutants, validated by experimental data

with little variation. The significance of this study is to contribute to knowledge on the behavior of antibiotics removal from water matrices at various levels of anions. Furthermore, results obtained from this research can provide a basis for scale-up of the PTR to treat large volumes of contaminated water.

1.7 Scope of the Study

This study evaluated two model pollutants (trimethoprim and tetracycline) commonly found in wastewater matrices of Kenyan water bodies. The study focused on optimization of three independent variables (pollutant dose, pH and catalyst dose) for the degradation of model pollutants. The Moi University WWTP was sampled to study the behavior of model pollutants in a real wastewater matrix.

1.8 Outline of Research

This research is comprised of five chapters. These chapters include: introduction, literature review, materials and methods, results and discussions and conclusions.

CHAPTER 2

LITERATURE REVIEW

2.1 Introduction

Faced with a global water crisis and growing concerns about environmental preservation, attempts are being made towards water recycling (Eniola et al., 2022). However, wastewater treatment plants face diverse recalcitrant emerging pollutants that must be removed before safe reuse. Among the emerging contaminants, pharmaceuticals are increasingly detected in aquatic environments due to improper treatment by wastewater treatment facilities (Aghalari et al., 2020). Therefore, there is increasing effort by the scientific community to develop novel wastewater treatment systems. Advanced oxidation processes have increasingly generated interest as a possible alternative treatment method for emerging pollutants. Consequently, this chapter explores the current situation of water use, classes of emerging contaminants, conventional wastewater treatment methods, and various AOPs. Besides, the strength and limitations of each method is probed.

2.2 Current Situation of Water Use

Sustainable development goal number six advocates for the availability and sustainable management of water resources and sanitation facilities (Reid, 2020). However, little has been achieved by many governments across the world in increasing the access to clean water. By 2035, 40% of the world population will live in severely water-stressed environments (United Nations, 2020). Further, the world's population is set to balloon to 9.7 billion by 2050, which will seriously aggravate water scarcity. A country is said to be water scarce if the per capita water available is less than $1000m^3$. Water scarcity is influenced by two factors: water quantity and water quality (Vliet et al., 2021). Water

scarcity has been influenced by global warming, urbanization, population growth, water pollution, and mismanagement of water resources.

Elevated water pollution levels by domestic and industrial sources, coupled with inefficiencies in pollutant removal by WWTP, have contributed to the persistent problem of water scarcity. For instance, 15-18 billion m^3 of freshwater sources are contaminated annually during the extraction of fossil fuels, while agricultural activities contribute to 40% of organic pollutants in water. Approximately 80% of wastewater returns to the aquatic ecosystem without proper treatment (Reid, 2020). Kenya is a water-scarce nation with annual per capita water consumption of less than $500m^3$ and a mean annual rainfall of 680mm (Priority & Plan, 2022; USAID, 2020). Previous studies have shown that only 59% of Kenyans have daily access to clean water (Unicef, 2020). The accelerated rate of urbanization in Kenya creates pressure on water resources due to the increased demand for both domestic and industrial consumption. Further, the waste production rate has grown and, when coupled with inadequate wastewater treatment facilities, leads to effluent disposal to river systems (Mulwa et al., 2021). For Kenya to achieve sustainable development goals, water scarcity is a priority that should be addressed.

2.3 Emerging Pollutants in Waste Water

2.3.1 Introduction

According to Norman Network, emerging pollutants can be “any natural or synthetic chemicals or pathogens that are detected in the environment but are not routinely monitored, have no legislation as regarding their maximum levels and are suspected to have adverse ecological effects (Teodosiu et al., 2018)”. Every year bodies, like the EPA receive approximately one thousand manufacturing notices of new chemicals,

many of which are pharmaceuticals and micro-plastics (Damania et al., 2019). For a contaminant to be classified as an emerging pollutant, it should meet at least one of the criteria below;

(a) A new chemical compound recently introduced into the environment (Haddaoui, 2021).
(b) Chemical substances that exist in environment for a longtime but are not proven to be potentially harmful (Teodosiu et al., 2018).
(c) Compounds that have been released over periods but are now detected due to advancements in detection techniques (Haddaoui, 2021).

Recently, the world has turned its attention to emerging pollutants. The highest concerns are pharmaceutical compounds and microplastics. The emergence of drug-resistant bacteria, antifungal-resistant fungi and amoeba, and drug-resistant micro-parasites shows the relationship between emerging pollutants and sanitation related pathogens (Damania et al., 2019).

The emerging pollutants mostly found in African waters include; pharmaceuticals, personal care products, hormones, pesticides, flame retardants, microplastics, etc. Nevertheless, most of these compounds are not new and due to the advancement of sensitive analytical techniques, they are now frequently detected (Karpińska & Kotowska, 2021). The most popular methods of analyzing the transformational products include; gas chromatography coupled mass spectrometry (GC-MS), liquid chromatography coupled mass spectrometry (LC-MS), liquid chromatography tandem mass spectrometry (LC-MS/MS) and nuclear magnetic resonance spectroscopy (NMR) (Teodosiu et al., 2018).

2.3.2 Classes of Emerging Pollutants

Emerging pollutants are commonly classified into four categories; pharmaceuticals, personal care products, pesticides/endocrine disruptors and industrial chemicals, as shown in Figure 2.1.

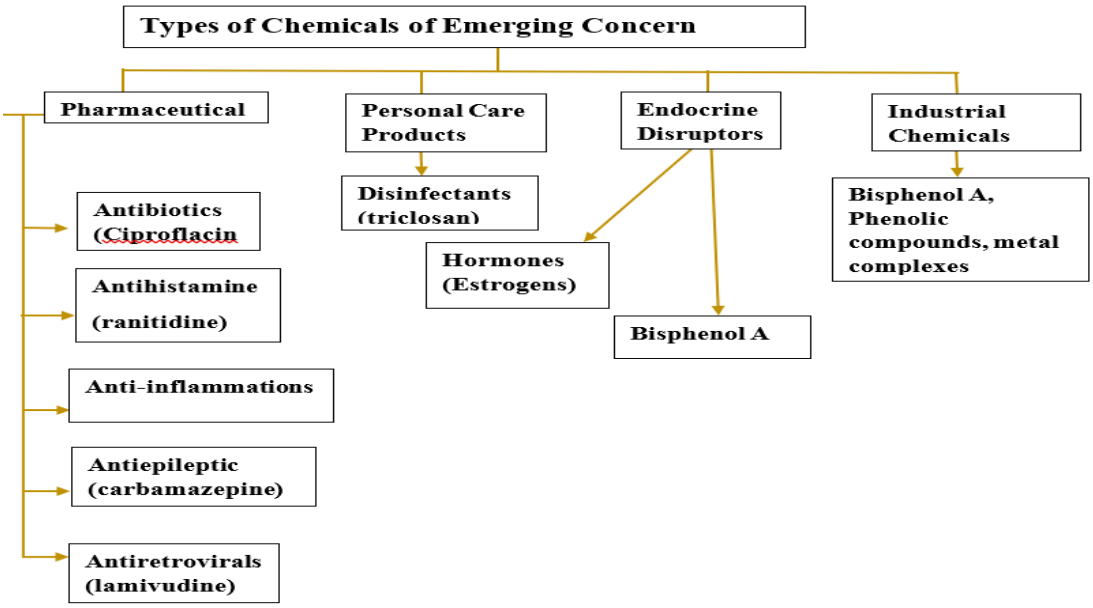

Figure 2.1: Classification of Emerging Pollutants (Patel et al., 2020)

2.3.2.1 Pharmaceuticals

Pharmaceutical contaminants have in several researches been detected in drinking water, effluent of wastewater treatment plants, open drains and in aquatic ecosystems (Ahmed et al., 2021). Pharmaceutical compounds can be classified into various classes, such as; analgesics, antibiotics, lipid regulators, β-blockers, hormones etc. During wastewater treatment, some pharmaceutical compounds have been noted to react with chlorine, forming extremely recalcitrant by-products(Ahmed et al., 2021).

In developing nations, Kenya included, antibiotics are the most frequently detected pharmaceuticals due to their widespread use for treating infectious illnesses. Antibiotics are difficult to treat because they contain complex structural composition, are ionizable and contain different pKa values. Antibiotics have been associated with the emergence

and propagation of antibiotic-resistance bacteria (Ngigi et al., 2020). According to the World Bank predictions, drug-resistant bacteria could kill 10 million people annually and impoverish 28 million others if no urgent measures are taken (Patel et al., 2021). Therefore, there is a need to address this threat, which may hinder global sustainable development. Common antibiotics found in Kenyan waters include; tetracycline, trimethoprim, spiramycin, erythromycin, sulfamethoxazole, sulfadoxine, etc. (Ngigi et al., 2020).

Hormones are another notable group of pharmaceuticals with potential androgenic and estrogenic effects (Ahmed et al., 2021). For instance, the feminization of male fish has been recorded in Ontario, Canada when the estrogen concentration of the lake is at 5-6ng/l. Therefore, pharmaceutical compounds in general, need to be monitored so as to establish their effects.

2.3.2.2 Personal Care Products

Personal care products consist of some active and inactive compounds; they are different from pharmaceuticals in that they are applied directly to the body (Patel et al., 2020). Prominent examples of personal care products include; sunscreens, toothpaste, toiletries, sunscreen, synthetic hormones, fragrances, etc.

Most personal care products such as, toothpaste, air fresheners, lotions contain a disinfectant such as triclosan and chloroprene. According to an extensive study in the US beginning in 2002, triclosan has consistently been linked with an increase in antibiotic resistance, genotoxic and endocrine disrupting. Moreover, triclosan is banned in the US and limited in Europe (Ahmed et al., 2021).

2.3.2.3 Endocrine Disruptors

Endocrine-disrupting chemicals interfere with the functioning of the endocrine system of an organism. Endocrine disrupting chemicals can be natural hormones or synthetic hormones (Kudłak et al., 2015). They work by linking up with oestrogenic receptors and interfering with hormonal functioning. The effects of endocrine disruptors are not well documented in humans. However, for aquatic organisms, effects like retardation of reproductive systems, poor embryonic development, inhibition of hormonal growth and feminization of fish have been recorded (Abdulrazaq et al., 2021). Common endocrine disruptors include; bisphenol A, steroid sex hormones, chlorinated organic pesticides, pharmaceutical residue, polyaromatic hydrocarbons, metal complexes, etc.

2.3.2.4 Industrial Chemicals

Industrial chemicals of emerging concern fall under various categories, such as plasticizers, flame retardants, fuel additives and polycyclic hydrocarbons. Plasticizers have become popular recently due to their high demand in the construction industry for improving the plasticity of gypsum, clay and concrete. Most chemicals in this group are potential endocrine disruptors. For instance, Bisphenol A is a well-known plasticizer with an annual production of 10.6million metric tons. Its effects on the ecosystem are poorly understood (Ahmed et al., 2021).

2.3.3 Target Contaminants

2.3.3.1 Trimethoprim

Trimethoprim is an antibiotic of the trimethoxybenzylpyrimidine group, a potent therapeutic agent (González et al., 2019). Besides, it is among the 14 pharmaceuticals with a risk quotient higher than 10 (Mpatani et al., 2021). The molecular structure of trimethoprim is shown in Figure 2.2. It has a molecular formula of $C_{14}H_{18}N_4O_3$, a

molecular weight of 290.3, maximum solubility in water is 400mg/L and a pKa value of 7.1 (Ljubas et al., 2023).

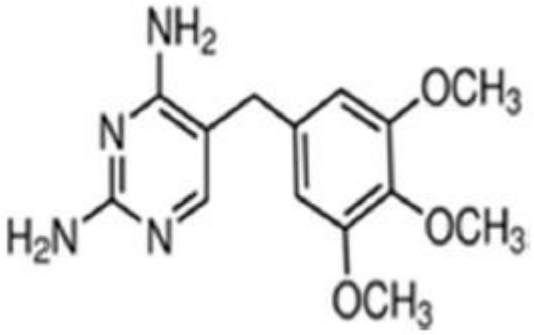

Figure 2.2: Structure of Trimethoprim (PubChem, 2020)

Trimethoprim antibiotic has broad-spectrum applications in human treatment, including; urinary tract, intestinal and respiratory systems. Furthermore, it is also offered as a combination drug with sulfamethoxazole for combating HIV infections (Mpatani et al., 2021). Despite its wide applications, trimethoprim is poorly metabolized in the human body, and at least 80% is excreted with human waste.

2.3.3.2 Tetracycline

Tetracycline is an antibiotic frequently detected in Kenyan water bodies due to its large-scale use for treatment of multiple infections in humans and livestock (Ciğeroğlu et al., 2023). The molecular structure of tetracycline is shown in Figure 2.3. Its molecular formula is $C_{22}H_{25}N_2O_8$ and has a molecular weight of 480.9. The maximum solubility in water is 1330mg/L and has three pKa values (pKa_1 = 3.3, pKa_2 = 7.7, pKa_3 = 9.25) (Zhou et al., 2022). Approximately 50% of tetracycline is released in aquatic systems in its unmetabolized states, hence posing a risk to the proliferation of antibiotic resistance genes (Li et al., 2022b).

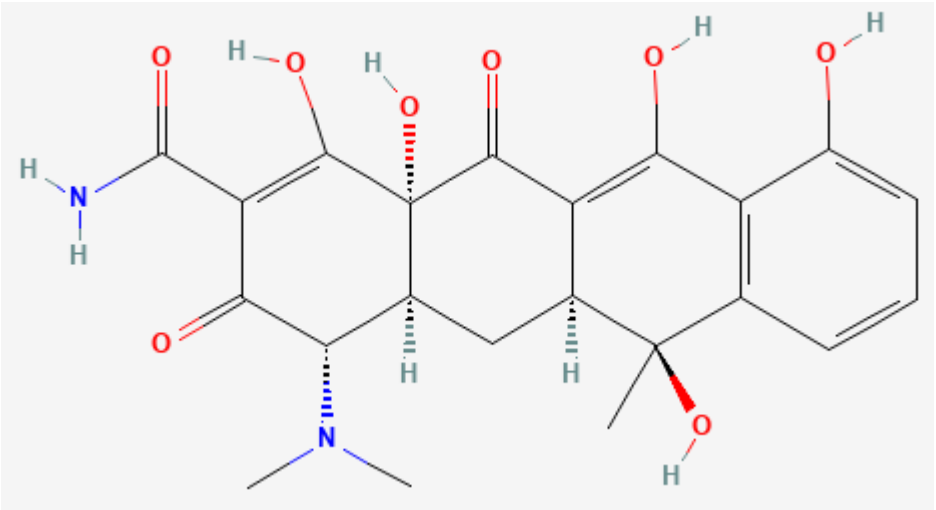

Figure 2.3: Structure of Tetracycline (Zhou et al., 2022)

2.4 Conventional Treatment Plants

Most conventional wastewater treatment plants consist of three basic units: (1) primary treatment section, which eliminates suspended materials; (2) secondary treatment section, which combines chemical and biological treatment methods; (3) tertiary treatment section, which arrests pollutants not degraded by the previous steps (Hazra et al., 2022). The most common conventional processes used in municipal wastewater treatments include; conventional activated sludge, membrane bioreactors, adsorption treatment, aerated lagoons, constructed wetlands, and waste stabilization ponds (Aghalari et al., 2020). These processes use physical, chemical, and biological means to remove pollutants.

2.4.1 Constructed Wetlands

Constructed wetlands (CWs) are engineered ecosystems consisting of plants, microbes and filler substrates designed to mimic natural wetlands. They can be classified according to flow regime as follows: (a) Free water surface, (b) horizontal subsurface flow, (c) vertical subsurface flow, (d) hybrid systems (Gorito et al., 2017; Lv et al., 2022). This technology utilizes plant and microbial species to create a biofilm structure that detoxifies organic pollutants (Hazra, et al., 2022). The most common bacterial

species are aerobic, anaerobic, denitrifying, and ammonia-oxidizing bacteria. Hence, these microbes utilize the pollutant as a substrate, aiding in decontamination. Additionally, CWs incorporate a wide variety of degradation pathways namely; sorption, hydrolysis, precipitation, photodegradation and plant uptake (Yan et al., 2018). Therefore, due to these synergistic interactions, CWs are highly efficient in degrading emerging pollutants but at low concentrations not exceeding 500µg/l.

Furthermore, (Carvalho et al., 2013) reported 94% and 98% removal efficiency for tetracycline and enrofloxacin, respectively using a CW. However, constructed wetlands, like other biological systems suffer from low pollutant removal efficiencies when handling complex organic compounds (Tawfik, et al., 2022). For instance, Massimiliano et al. studied the removal efficiencies of five pharmaceuticals using four CW configurations. He found that all configurations could effectively remove BOD, total nitrogen and caffeine. However, no configuration could eliminate sucralose, a known recalcitrant compound (Sgroi et al., 2018). Therefore, CWs must be combined with other technologies to effectively remove recalcitrant compounds.

2.4.2 Waste Stabilization Ponds

Waste Stabilization ponds (WSP), commonly known as lagoons, are shallow ponds used as a low-cost treatment technology for domestic and industrial wastewater. WSPs can be divided into three types namely, the anaerobic, facultative and maturation pond. The anaerobic and facultative ponds are the primary and secondary treatment stages, respectively. Besides, most BOD and nutrients are removed at these ponds (Desye et al., 2022). On the other hand, the maturation pond serves as the polishing step, where pathogens are eliminated before disposal (Gruchlik et al., 2018).

WSPs handle various emerging pollutants such as pharmaceuticals, personal care products, pathogens and heavy metals. These plants depend on a complex biodegradation mechanism by bacteria and algae, sorption and photodegradation to eliminate pollutants. Therefore, WSP's efficiencies depend on solar irradiance, temperature, pH, oxygen concentration and the geometry of the pond (Desye et al., 2022). Furthermore, operational parameters such as short hydraulic retention time may severely impede the removal of recalcitrant micropollutants (Gruchlik et al., 2018).

Kumar et al. studied the removal of various antibiotics (diclofenac, paracetamol, erythromycin), endocrine disruptors(17beta-estradiol) and pesticides (malathion, carbaryl, DDT and Aldrin). The results revealed that paracetamol and carbaryl had removal efficiencies <75%, while 17beta-estradiol ranged between 50-75%. However, most pesticides had low removal efficiencies ranging between 18-41% (Kumar & Kumar, 2020). The poor removal rates for pesticides such as aldrin could be attributed to the recalcitrant organochlorine bonds. Such compounds can only be eliminated by photodegradation and sorption processes. Besides, most pesticides are highly hydrophobic in water.

2.4.3 Adsorption

Adsorption is a technique for wastewater decontamination that exploits the strong attractive forces between adsorbent and pollutant. This technology is widely preferred due to its high porosity, reusability of adsorbent, and large specific surface area. Common adsorbents include; clay, zeolites, activated carbons, and carbon nanotubes. Activated carbons are the most widely used adsorbents and can be in powder or granulated forms. The mechanism of action for pollutant adsorption involves ion exchange, van der Waal forces, hydrogen bonding, electrostatic, and dipole interaction

(Eniola et al., 2022). Nevertheless, adsorption suffers from several setbacks namely; adsorption preconcentrates the pollutant from the liquid phase and transfers it to the adsorbent media with no degradation, which will require final disposal (Rodr et al., 2022), and the synthesis of adsorbents is energy intensive with a huge carbon footprint and hence unsustainable (Rout et al., 2021).

Alnajrani et al. studied the adsorption of four antibiotics using a polymer of intrinsic micro-porosity (PIM) adsorbent. The results showed that large disparities existed in the adsorption capacities among the target pollutants. The adsorption capacities were 33, 189, 213 and 257mg/g for ciprofloxacin, amoxicillin, doxycycline, penicillin, respectively (Alnajrani & Alsager, 2020). Similarly, Zeng et al. studied the adsorption of doxycycline and ciprofloxacin using biochar (Ajala & Akinnawo, 2023). The results showed that doxycycline (170.36 - 432.90mg/g) had higher adsorption capacities than ciprofloxacin (48.80-131.58mg/g) at a temperature range of 298 - 318K. These studies suggest that adsorbents may have different selectivity for target molecules, which could be a significant limitation of adsorption. Therefore, there is a need to combine adsorption with other treatment methods.

2.4.4 Conventional Activated Sludge

Conventional Activated sludge (CAS) is a secondary treatment technique that uses a biofilm to biodegrade organic pollutants. These treatment plants are very common in many parts of the world and are designed primarily to remove organics and nutrients (Shukla & Ahammad, 2023). Biodegradation involves metabolic reactions by microorganisms such as carboxylation, glycosylation, hydrogenation, and ring cleavage. The pollutant can be fully mineralized or converted into transformational products during the degradation process. Hence, the degree of mineralization depends

on factors such as reactor operation conditions, the nature of the pollutant, and the sludge properties (Rout et al., 2021).

Activated sludge reactors are preferred due to their low construction costs, are environmentally friendlier than chlorination and cheap operating costs (Mareai et al., 2020). However, they generate a lot of sludge that requires secondary treatment, have high power consumption and frequent biomass washout in the reactor, which leads to poor performance (Arman et al., 2021). Furthermore, the CAS reactor has low mineralization efficiency for emerging pollutants since some transformational products formed can be more toxic than the parent group (Rout et al., 2021).

Shukla & Ahammad (2023), compared the performance of a modified trickling filter (MTF) and a CAS in the degradation of emerging pollutants. The results revealed that the removal of diclofenac and mefenamic was (>50%) for the MTF system and below 45% for the CAS system. Furthermore, only 11% removal was observed in the CAS for recalcitrant carbamazepine as compared to 42% reduction in the MTF. Similarly, a study by (Martínez-orgániz et al., 2021) found carbamazepine to be persistent in a CAS plant in Mexico. These findings suggest the deficiencies of CAS in eliminating recalcitrant pollutants.

2.4.5 Membrane Bioreactors

Membrane bioreactors (MBR) are a secondary wastewater treatment method, introduced initially to replace the conventional activated sludge. These reactors blend the principles of anaerobic biodegradation and membrane separation to yield high-quality effluent (Rout et al., 2021; Sengupta et al., 2022). Common membrane types include; ultrafiltration, nanofiltration, and microfiltration. MBRs are attractive to many WWTPs due to their high efficiency in removing the BOD and COD, effective at high

organic loading of mixed liquor suspended solids and generating less sludge than CAS (Arman et al., 2021). Furthermore, MBR is effective in brackish water reclamation for agricultural reuse. However, MBRs are prone to membrane fouling, which greatly affects their stability and performance over time (Khastoo et al., 2021; Qu, 2019). Besides, MBRs produce a concentrated pollutant effluent, which may necessitate secondary treatment and disposal.

Aerobic treatment systems degrade pharmaceutical pollutants mainly by biosorption and biodegradation. The aerobic treatment technologies currently in use include; activated sludge, total reflux sludge reactor process, and moving bed biofilm reactor (Eniola et al., 2022). Aerobic reactors are more effective than anaerobic reactors, however, they handle only effluents with low organic loading. On the other hand, anaerobic reactors are advantageous since they generate less sludge, are effective at high organic loads, and have little operating costs.

Kamaz et al (2019), investigated the removal of acetaminophen, atrazine, amoxicillin and estrone in an MBR system. Within 4 hours, 90% of acetaminophen and amoxicillin were eliminated in the anoxic and aerobic tanks. Moreover, at time 0, a 90% removal was observed for estrone, which was attributed to absorption by microorganisms. However, for atrazine, only 20% was initially removed by absorption. Besides, there was no significant change in its concentration even after 12 hours of reaction. These findings suggest that the MBR system is deficient in the removal of persistent micropollutants.

In conclusion, no single conventional method can completely remove emerging pollutants. Some pollutants such as carbamazepine, aldrin and sucralose are known recalcitrant pollutants which are persistent in multiple treatment methods. Besides,

most conventional systems generate excess sludge, have high power requirements and are highly selective to certain emerging pollutants. Therefore, these systems need to be supplemented with alternative treatment methods.

2.5 Advanced Oxidation Processes

Advanced oxidation processes (AOP) are a class of bio-friendly treatment processes that involve the generation of strong reactive oxygen species ($^{\bullet}O_2^-$, $^{\bullet}OH$) from hydrogen peroxide or dissolved oxygen (Ma et al., 2021), which react with organic carbons, degrading them to simpler molecules or complete mineralization to form CO_2 and H_2O. Partial degradation of molecules yields smaller molecules than the parent contaminant, which can be electron-poorer and are easier to treat in subsequent steps (Coha et al., 2021).

Several researchers have used AOP methods to degrade organic pollutants. AOPs can be divided into two classes: (1) chemical oxidation methods, which consist of ozonation, UV, Fenton processes, electrochemical oxidations methods and sonolysis and (2) photochemical methods, which are a combination of chemical methods and UV/Solar light (Akbari et al., 2021).

However, it's noteworthy that a single AOP method is not sufficient alone in treating real wastewater due to; (1) high organic loading and complex wastewater matrix; (2) the presence of competing ions (Cl^-, CO_3^{2-}, NO_3^-) that may scavenge the reactive oxygen species; (3) the inherent limitations of a specific AOP (Ma, et al., 2021). Therefore, different AOPs must be combined to improve the oxidation efficiency of pollutants by fast generation of radicals, extend the operating parameters of the AOP technology and address the limitation of the AOP method.

2.5.1 Chemical Oxidation Methods

2.5.1.1 Ozonation

In recent times, the ozonation process has been employed in recent times in treating industrial wastewater owing to its high reactivity when treating recalcitrant compounds (Gautam et al., 2020). Ozone has an oxidation potential of 2.07V and is a strong oxidizing agent that can directly oxidize pollutants and kill pathogens (Coha et al., 2021).

Ozonation works by two mechanisms: (1) Direct oxidation of organic molecules by electrophilic attacks, which convert them to smaller molecules. For example, ozone readily attacks the C=C double bonds, aromatic compounds, alcohols and alkenes and breaks them into smaller molecules such as ketones, carboxylic acids and aldehydes (Ikehata & Li, 2018); (2) indirect oxidation by oxidizing water to generate hydroxyl radicals that are even stronger oxidant than ozone. These radicals degrade organic pollutants non-selectively at high reaction rates (Akbari et al., 2021).

During reactions, hydroxyl radicals attack both organic and inorganic substrates by several reactions. These reactions include; electrophilic addition, hydrogen abstraction, electron transfer reactions and radical-radical reactions (Ikehata & Li, 2018). Ozonation is preferred to the Fenton process since it is environmentally friendly. However, indirect ozone reactions are terminated by hydroxyl radical scavengers, namely, carbonates, bicarbonate, tert-butanol and humic substances.

The following equations give the mechanism of reactions;

$$O_2 + H_2O = 2 \bullet OH + O_2 \quad \text{Equation 2.1}$$

$$O_3 + 2OH^- = 2 \bullet O_2^- + H_2O \quad \text{Equation 2.2}$$

$$O_3 + HO_2 \bullet = 2O_2 + \bullet OH \quad \text{Equation 2.3}$$

$O_3 + \bullet OH = O_2 + HO_2 \bullet$ ---------- Equation 2.4

Budi et al., (2022), studied the degradation of ciprofloxacin in a bubble column operated in two configurations, namely; the aerobic-pump-based ozonation (APO) and the flow ozonation (FO). The APO system achieved a higher pollutant removal efficiency of 83.5% in 600 minutes, while the FO yield was 60.9%. Besides, a similar trend was observed for the TOC removal with 68% and 30% yield for the APO and FO systems, respectively. The difference in removal for the two systems was attributed to the higher efficiency of the APO system in generating ozone microbubbles.

Benefits of Ozonation

Ozonation is characterized by several benefits, which include; (1) Ozone is the disinfectant of choice for treating drinking water due to its high cell lytic activity that kills pathogens (Mishra et al., 2017), (2) Ozone is capable of removing colour, taste and odor from wastewater, (3) Ozone has high oxidizing potentials and can oxidize a wide variety of organic pollutants. Furthermore, ozone is two times more powerful and 3,000times faster than chlorine (Tripathi & Hussain, 2021).

Drawbacks of the Ozonation process

The ozonation process suffers from the following weaknesses: (1) Ozone readily reacts with bromide ions present in some wastewaters to form the potentially carcinogenic bromate ions (BrO_3^-) (Coha et al., 2021), (2) Ozone has low oxidation rates for ammonia and chlorinated pollutants such as; trihalomethanes, chlorobenzenes (Mishra et al., 2017), (3) Ozone doesn't fully mineralize organic pollutants but reduces it into smaller chains (Gautam, et al., 2020).

To address these deficiencies, ozone is combined with other AOPs such as hydrogen peroxide, UV light and catalyst. The combined processes are outlined below;

a) Ozone/H_2O_2

The combination of ozone and hydrogen peroxide represents the most widely studied and implemented advanced oxidation processes (Ikehata & Li, 2018). Studies have found that low concentrations of hydrogen peroxide in ozone form hydroperoxide (HO_2^-), which rapidly accelerates ozone decomposition in water, increasing the yield of hydroxyl radicals (Gautam, et al., 2020). The reaction constant for this reaction is very large. Hence, O_3/H_2O_2 is a very effective process for degrading organic pollutants. The subsequent reactions can be illustrated as shown below;

$$H_2O_2 = HO_2^- + H^+ \quad \text{Equation 2.5}$$

$$HO_2^- + O_3 = \bullet OH + O^{2-} + O_2 \quad \text{Equation 2.6}$$

Adil et al., (2020), performed a comparative study of the degradation of trimethoprim and sulfamethoxazole using O_3, O_3/H_2O_2 and O_3/S_2O_8 systems. The results showed that the use of oxidant alone resulted in negligible degradation for both pollutants. However, a degradation efficiency of 90% was observed at 6, 6.7 and 8 minutes for O_3/H_2O_2, O_3/S_2O_8 and O_3, respectively. A similar trend was also observed for sulfamethoxazole, with 90% removal achieved at 6.3, 6.8 and 7.4 min for O_3/H_2O_2, O_3/S_2O_8 and O_3, respectively. Likewise, the O_3/H_2O_2 system had the highest TOC removal rates for all systems. This was evidence of the high efficiency of O_3/H_2O_2 in eliminating antibiotics.

b) Ozone/UV

When UV light is irradiated on the dissolved ozone molecules, they readily absorb UV at an optimum wavelength of 260nm (Ikehata & Li, 2018). The ozone molecules then undergo photolysis reaction to generate hydrogen peroxide. The resultant hydrogen

peroxide molecules can either undergo another photolysis reaction to generate hydroxyl radicals or initiate the decomposition of ozone, as shown in the reaction below;

$$O_3 + H_2O + hv = H_2O_2 + O_2 \quad \text{Equation 2.7}$$

$$H_2O_2 + hv = 2 \bullet OH \quad \text{Equation 2.8}$$

$$H_2O_2 + \bullet OH = HO_2^- + H_2O \quad \text{Equation 2.9}$$

(Souza et al., 2022), investigated the removal of four anti-cancer drugs (doxorubicin, daunorubicin, epirubicin and irinotecan) using UV/Ozone. After 60 minutes of reaction using UV irradiation alone, the degradation rates were 55.6%, 88.3%, 97.3% and 99% for irinotecan, daunorubicin, doxorubicin, and epirubicin, respectively. However, on combining UV/Ozone treatment, 100% removal was observed for all the pollutants. These findings were evidence of the superior effect of ozone on the UV-photolysis process.

Drawbacks of Ozone/UV

The Ozone/UV process has some significant challenges namely; (1) The process is highly energy intensive due to the use of UV-light for photolysis, (2) Huge concentrations of ozone are needed for the complete mineralization of target pollutants (Ikehata & Li, 2018; Gautam et al., 2020).

c) Ozone/Catalyst

Both homogeneous and heterogeneous catalysts can improve ozonation reactions. Besides hydrogen peroxide, most transition metal ions (Co^{2+}, Mn^{2+}, Zn^{2+}, Cu^{2+} and Ni^{2+}) have been found to be efficient homogeneous ozone catalysts (Ikehata & Li, 2018). For instance, cobalt ions are oxidized by ozone to yield hydroxide radicals.

$$O_3 + Co^{2+} + H_2O = \bullet OH + CoOH^{2+} + O_2 \quad \text{Equation 2.10}$$

On the other hand, heterogeneous catalysts consisting of metal oxides have promising potential in eliminating refractory pollutants (Rekhate & Srivastava, 2020). Metal oxides used include; TiO_2, MnO_2, Fe_2O_3, $MgFe_2O_4$, $ZnFe_2O_4$, Ru/Ce_2O_3 and supported metal oxides. Metal catalysts are preferred because they possess active D-electronic structure. This structure facilitates electron transfer from the catalyst to pollutants, hence lowering the activation energy needed for ozonation. Metal catalysts have been found to enhance the degradation of fatty acids.

The mechanism for catalytic ozonation is a two-step process as follows; (1) interfacial reaction mechanism where catalysts use their large surface area to adsorb organic pollutants forming a complex that is oxidized by hydroxyl radicals; (2) the hydroxyl mechanism suggests that catalysts increase solubility of ozone in the medium and acts as initiators for ozone decomposition (Rekhate & Srivastava, 2020).

The heterogeneous based catalysts have been studied under UV light and successfully treated high strength industrial waste effluents (Ikehata & Li, 2018). For instance, (S. Zhang et al., 2022) investigated the removal of methyl orange from textile wastewater using O_3/Mn/Mg/Ce ternary catalyst. At optimum conditions, there was 96% and 48.7% methyl orange degradation and COD removal, respectively. However, for a purely ozone-catalyzed system, the pollutant removal efficiency was 31.2% and negligible COD removal. This showed a remarkable improvement on degradation after the addition of catalyst.

Benefits of Ozone/Catalyst

The following benefits are associated with ozone coupled with catalyst; (1) consumes less ozone compared to other combinations and offers a cost-effective method for pollutants degradation, (2) higher degradation efficiencies can be achieved towards

organochlorides as compared to other ozonation methods, (3) coupling ozone to photocatalysts controls the formation of bromate which is a carcinogen compound, (4) photocatalytic ozonation can be used for disinfection of wastewater since the hydroxyl radical leads to oxidative destruction of pathogens cell wall (Rekhate & Srivastava, 2020).

Drawbacks of Ozone/catalyst

Most heterogeneous catalysts have low photo-efficiencies in the visible light spectrum and thus require UV light for maximum effectiveness in generating hydroxyl radicals (Ikehata & Li, 2018; Rekhate & Srivastava, 2020).

2.5.1.2 Sonolysis

This process involves the application of ultrasound in a solution at a frequency range of 20kHz-10MHz (Mishra et al., 2017). When vapour bubbles in the solution experience a pressure drop, their size increases rapidly up to a critical pressure magnitude. At this point, the critical pressure of the bubble is lower than the vapour pressure of the solution. Therefore, the bubble implodes, generating high temperature of approximately 4700^{o}C and a pressure of 600 bars (Roy et al., 2022). Due to these intense conditions, water molecules dissociate into hydrogen and hydroxyl radicals. In addition, extreme conditions can break the organic and chemical bonds of pollutants. Hydroxyl radicals produced are now responsible for the degradation of the organic pollutants present in the solution (Mishra et al., 2017).

(P. Liu et al., 2023), studied the effect of ultrasonic frequency on sonolytic degradation of sulfamonomethoxine sodium (SMM) in water and milk. The ultrasonic frequency was studied at 40, 80, 120 and 500kHz. The results showed that the removal of SMM increased with increasing frequency from 7.8–31.6% for 40 -120kHz, respectively. A

similar trend was also observed for the degradation of SMM in milk. The removal efficiency ranged between 6.3–14.6%. The improved degradation at higher frequencies was attributed to the increased generation of microbubbles resulting in intense cavitation. This consequently resulted in enhanced generation of reactive oxygen species.

Advantages of the Sonolysis Process

Sonolysis process has the following benefits: (1) It operates in a mild environment while treating toxic wastes, (2) It has the ability to treat cloudy water containing suspensions (Mishra et al., 2017; Gautam et al., 2020).

Drawbacks

The sonolysis process has the following drawbacks: (1) the power dissipation and time period for complete degradation is high, hence uneconomical, (2) high cost of installation when this process is applied for complex wastewater treatment, (3) low degradation and mineralization efficiency of pollutants is obtained during the process (Gautam, et al., 2020).

2.5.1.3 Electrochemical Advanced Oxidation Processes

Electrochemical oxidation processes use electrode reactions to degrade organic pollutants. Different electrochemical processes exist, the most prominent ones include; electrooxidation, photo-electrocatalysis and electro-Fenton. Electrochemical oxidation processes are effective methods for treating pharmaceutical wastewater (Roy et al., 2022).

a) Electrooxidation

Contaminant degradation in electrooxidation may occur through, direct and indirect oxidation (da Silva et al., 2021). Direct oxidation involves electron transfer from the

organic pollutant to the anode. For indirect oxidation, hydroxide and oxide radicals are generated at the anode; they then diffuse to the bulk fluid and attack the organic molecules.

The oxidation path to be either direct or indirect depends on the electrode material used (Silva, et al., 2021). Electrodes types are classified into active and non-active anodes. The most common non-active anodes include; boron-doped diamond, antimony and lead oxides. Non-active anodes oxidize water to generate the physisorbed hydroxyl radicals. The hydroxyl radical then reacts with the pollutant, resulting to full mineralization or some intermediates. The weak physisorption of hydroxyl radical can react in the fluid diffusion layer improving complete mineralization.

The equations taking place at the anode can be illustrated as follows;

$$M + H_2O = M[\bullet OH] + H^+ + e^- \quad \text{Equation 2.11}$$

$$M[\bullet OH] + R = M + RO + H^+ + e^- \quad \text{Equation 2.12}$$

$$M[\bullet OH] + H_2O = M + O_2 + 3H^+ + 3e^- \quad \text{Equation 2.13}$$

Where M=anode and M[•OH] =hydroxyl radical adsorbed on the anode

Active anodes mainly consist of platinum, mixed metal oxides and dimensionally stable anodes (Silva, et al., 2021). Nevertheless, active anodes have a strong interaction with the hydroxyl radical. Thus, the generated hydroxyl radical is chemisorbed, which hinders reaction with pollutants at the anode surface.

The presence of competing ions such as chloride and sulphates are seen to be advantageous. For instance, boron doped diamond reduces both chlorides and sulfates

into active chlorine species (Cl_2, HClO) and persulfate ($S_2O_8^{2-}$, SO_4^{2-}), which can be utilized in degrading organic pollutants (da Silva et al., 2021).

Liu et al. investigated the degradation of three antibiotics using electrochemical oxidation. The removal efficiency of the pollutants was as follows: paracetamol (68.7%) < diclofenac (86.3%) < sulfamethoxazole (96.7%). The poor removal efficiency of paracetamol was attributed to its neutral molecules, which hindered mass transport to the electrode surface (Liu et al., 2021). On the other hand, the high degradation of SMX was attributed to the synergy between hydroxyl and free chlorine radicals.

Benefits of Electrochemical Oxidation

The electrochemical oxidation process offers several advantages namely, (1) Has high efficiency in the removal of recalcitrant pollutants, (2) the process requires simple equipment setup, hence cheaper installation costs, (3) efficient utilization of electrical power by the process (Gautam, et al., 2020).

Drawbacks of Electrochemical Oxidation

The process suffers several shortcomings, which include; (1) electrochemical oxidation operates best at low pH hence acidic conditions must be maintained, (2) electrodes used are highly expensive e.g boron doped diamond, (3) the process generates sludge which may lead to secondary pollution, (3) high chemical consumption during the process (Gautam, et al., 2020).

b) Photoelectrochemical oxidation

Recently, photoelectrochemical processes have received attention as a possible solution for the treatment of dye-laden wastewater. This method combines photocatalytic

oxidation, and electrochemical processes and uses a semiconductor as the anode with UV or sun assisted illumination (Silva et al., 2021; Ma et al., 2021). Photoelectrochemical oxidation has more than two options for generating hydroxyl radicals. One method is the generation of radicals by heterogeneous photocatalysis, and the other is electrochemical oxidation as illustrated earlier (Silva et al., 2021).

The most common semiconductors used in photoelectrochemical oxidation are TiO_2 and ZnO. When illuminated with light photons, these semiconductors have one electron transferred from valence band to conduction band. This, in turn generates a positive hole, which is responsible for oxidizing a water molecule to produce hydroxyl radicals (Silva et al., 2021). However, it should be noted that the semiconductors face the drawback of charge recombination. The semiconductors have been improved by doping with transition metals. However, best performance has been observed by using rare earth metal oxides such as RuO_2, WO_3, and CeO_2.

The reaction occurring at the semiconductor is as follows;

$$TiO_2 + hv < 387nm = e_{CB^-} + h_{VB^+} \quad \text{Equation 2.14}$$

$$H_2O + h_{VB^+} = \bullet OH + H^+ \quad \text{Equation 2.15}$$

$$e_{CB^-} + O_2 = \bullet O_2^- \quad \text{Equation 2.16}$$

Using the semiconductor as the photoanode is advantageous in that application of external electric field polarizes the semiconductor, minimizing electron and hole recombination (Silva et al., 2021). Also, more electrons can be transported using the external circuit, increasing the process's oxidation rates.

Mahhumane et al., (2022), fabricated a Z-scheme composite of Bi_2WO_6/TiO_2 and immobilized it on the surface of a titanium oxide photoanode. The setup was used for photoelectrocatalytic (PEC) degradation of paracetamol using sunlight. The results showed that the PEC process achieved 84% pollutant degradation and 72% TOC removal. However, when the study was run with only solar light, the pollutant removal efficiency and TOC removal were 42% and 30%, respectively. This showed the synergistic interaction between sunlight and the electrochemical process.

Benefits of Photoelectrochemical Oxidation

The photoelectrochemical process has the following benefits: (1) has high efficiency in degrading recalcitrant compounds; (2) combines advantages of catalytic oxidation and electrochemical oxidation; (3) is potent in disinfection of water (Silva et al., 2021; Roy et al., 2022).

Drawbacks of Photoelectrochemical Oxidation

The photoelectrochemical process suffers the following setbacks: (1) High energy consumption for electrooxidation processes; (2) the semiconductor anode requires expensive rare earth metal as dopants e.g RuO_2; (3) the process functions best at low pH values (Mishra et al., 2017; Roy et al., 2022).

2.5.1.4 Fenton Processes

a) Classical Fenton

Fenton process can be used to treat complex industrial wastewaters due to its efficiency as an advanced treatment method. Nevertheless, this method can achieve the removal of toxicity, color and COD reduction from a wastewater sample (Gautam et al., 2022). Fenton's process consists of two reagents; hydrogen peroxide and Fe^{2+}. At acidic pH, Fe^{2+} initiates a catalytic reaction that decomposes hydrogen peroxide, leading to the

production of hydroxyl radicals. The hydroxyl radical attacks the organic pollutant, forming a hydrocarbon radical chain, which is critical in the regeneration of the Fe^{2+}. Fenton's process takes place by a radical mechanism. Hence all reactions stated below occur simultaneously.

$$Fe^{2+} + H_2O_2 = Fe^{3+} + OH^- + \bullet OH \quad \text{Equation 2.17}$$

$$Fe^{3+} + H_2O_2 = Fe^{2+} + HO_2\bullet + H^+ \quad \text{Equation 2.18}$$

$$Fe^{2+} + \bullet OH = Fe^{3+} + OH^- \quad \text{Equation 2.19}$$

$$Fe^{3+} + HO_2\bullet = Fe^{2+} + O_2 + H^+ \quad \text{Equation 2.20}$$

$$\text{Organic pollutant} + \bullet OH = \text{Degraded product} \quad \text{Equation 2.21}$$

However, Fenton's Process is affected by other process factors such as temperature, pH, Fe^{2+}/H_2O_2 ratio and competing ions. Low pH is important for the regeneration of Fe^{2+} from Fe^{3+}. However, parasitic reactions are of concern since they cause Fe^{3+} to be precipitated as hydroxide. Consequently, this yields iron sludge, thus pH should be well controlled for reaction selectivity (Coha et al., 2021). Fe^{2+}/H_2O_2 ratio also affects the reaction and should be at optimum since high ratios favor scavenging reactions.

(Adamek et al., 2022), investigated the effects of pH and Fe^{2+}/H_2O_2 ratio on the degradation of sulfathiazole. The optimum pH was obtained at pH $2-4$, which achieved 95% sulfathiazole removal in 30 minutes. However, at pH 6.5, the pollutant degradation was completely inhibited due to hydrolysis of Fe^{2+} to insoluble $Fe(OH)_3$. Similarly, the optimum H_2O_2/Fe^{2+} ratio was 20, yielding 90% pollutant removal with 38% undecomposed peroxide. Ratios of 50 - 100 lead to decreased pollutant removal due to competing reactions between peroxide and •OH radical.

Benefits of Classical Fenton Process

The main benefits associated with the Classical Fenton process include; (1) Classical Fenton process has the shortest reaction time amongst all the AOPs, (2) a high degree

of mineralization is achieved using the Fenton process, (3) Less costs are required to setup and maintain the classical Fenton process (Coha et al., 2021; Gautam et al., 2020).

Drawbacks of Fenton Process

The main drawbacks associated with Fenton process include; (1) the process must be operated at a low pH in the range of 2-3 for optimum degradation, (2) the process generates a high amount of sludge, which may be potentially more toxic than initial contaminants, (3) Slow regeneration rate of Fe^{2+} from Fe^{3+} and loss of catalyst due to metal leaching (Coha et al., 2021; Gautam et al., 2020)

b) PhotoFenton

The method uses UV light to address the problem of low regeneration rates of Fe^{2+} by the Fenton process (Ameta et al., 2018). During reaction, hydrogen peroxide undergoes photolysis in UV light generating a hydroxyl radical. UV irradiation also aids in the photocatalytic reduction of Fe^{3+} to form Fe^{2+}, and in the process, hydroxyl radicals are generated. The reaction sequence is illustrated as shown below;

$$Fe^{3+} + H_2O + hv = Fe^{2+} + H^+ + \bullet OH \quad \text{Equation 2.22}$$

$$Fe^{3+} + H_2O_2 + hv = Fe^{2+} + HO_2\bullet + H^+ \quad \text{Equation 2.23}$$

The photo-Fenton process gives optimum degradation at pH 3, since the Fe^{3+} ions are most soluble at these conditions and the $Fe(OH)^{2+}$ are highly photoactive (Ameta et al., 2018). Furthermore, a study conducted by Alalm et al. on a solar photo-Fenton process ($FeSO_4/H_2O_2$/compound parabolic collector) supported this argument. The study involved the degradation of four pharmaceuticals (ampicillin, amoxicillin, diclofenac and paracetamol). The results revealed that the optimum pH was 3 since 100% removal for all the pollutants was achieved. However, when the pH was raised to 10, the degradation efficiency of the pollutants decreased drastically. The decrease in

degradation at high pH levels was attributed to precipitation of iron ions into hydroxide, which inhibited the Fenton process (Alalm et al., 2015).

Benefits of Photo-Fenton

The main benefits associated with photo-Fenton process include; (1) the process has higher rates of reaction compared to classical Fenton process, (2) the process has increased levels of biodegrading, detoxification and COD removal rates as compared to Classical Fenton (Ameta et al., 2018; Gautam et al., 2020).

Drawbacks of PhotoFenton

The main drawbacks associated with photo-Fenton process include; (1) UV light must be operated for a long time for the process to be effective, (2) it must be still operated at low pH in the range of 2-3 for optimum degradation, (3) high energy consumption of the UV light which is uneconomical (Ameta et al., 2018; Gautam et al., 2020).

c) Electro-Fenton

The electro-Fenton process combines classical Fenton and electrochemical oxidation processes. Recently, this process has gained popularity due to its relative ease of degradation for persistent organic pollutants. At the cathode electrode, Fe^{3+} is reduced to Fe^{2+} and hydroxyl radical is generated (Coha et al., 2021). Also, hydrogen peroxide can be generated at the cathode through the reduction of oxygen hence air should be continuously circulated in the cell during reaction (Gautam et al., 2022). Then, Fe^{2+} in the solution medium reacts with hydrogen peroxide, generating hydroxyl radicals that can attack the pollutant.

$$O_2 + 2H^+ + 2e^- = H_2O_2 \quad \text{Equation 2.24}$$

$$Fe^{3+} + H_2O_2 = Fe^{2+} + OH^- + \bullet OH \quad \text{Equation 2.25}$$

Moratalla et al., (2022), investigated the degradation of penicillin G using an Electro-Fenton process (Goethite/UVC/BDD). The study compared the performance of a

boron-doped diamond anode and a mixed metal oxide. The maximum degradation was observed at pH 3. The BDD anode achieved complete antibiotic degradation, while the MMO anode achieved 75.5%. However, there was insignificant TOC removal (<5%) for both anodes due to the accumulation of transformational products.

Benefits of ElectroFenton

The main benefits associated with the Electro-Fenton process include; (1) the process can achieve complete mineralization of the organic pollutant, (2) less reagents are needed since the process can generate hydrogen peroxide in-situ, (3) hydroxyl radical for this process is generated by two pathways (Coha et al., 2021).

Drawbacks of ElectroFenton

The main drawbacks associated with ElectroFenton process include; (1) the process must still be operated at acidic pH ranges just like classical Fenton, (2) reactions may suffer from concentration polarization at the electrodes which may inhibit the generation of hydroxyl radicals, (3) process has significant high operational and maintenance costs (Gautam et al., 2022).

2.5.2 Heterogeneous processes

Homogeneous Fenton processes, despite various modifications, still remain unattractive for commercial applications due to the leaching of iron ions, generating sludge and the requirement for a narrow pH range; all these factors require post-treatment which can be expensive (Thomas et al., 2021). Therefore, several researchers have examined the use of iron species immobilized on solid supports, which are known as heterogeneous Fenton Processes (Ameta et al., 2018). Heterogeneous processes are attractive since no sludge is generated, they are functional at neutral pH, and there is reduced leaching of iron ions to the medium (Thomas et al., 2021).

2.5.2.1 Iron Oxide

Iron oxides consist of haematites, magnetite, ferrihydrite, goethite, lepidocrocite and shwertmannite. Due to their semiconducting abilities, non-toxicity and biodegradable nature, iron oxides have been explored as photocatalysts (Thomas et al., 2021). The reaction mechanism of iron oxides is as follows;

$$\text{Iron oxide} + \text{hv} = \text{Iron oxide}\,(\text{h}+, \text{e}-) \quad \text{Equation 2.26}$$

$$e_{CB}^{-} + O_2 = \bullet O_2^{-} \quad \text{Equation 2.27}$$

$$h_{VB}^{+} + H_2O = H^{+} + \bullet OH \quad \text{Equation 2.28}$$

$$h_{VB}^{+} + OH^{-} = \bullet OH \quad \text{Equation 2.29}$$

$$H_2O_2 + e^{-} = \bullet OH + OH^{-} \quad \text{Equation 2.30}$$

$$Fe^{3+} + e^{-} = Fe^{2+} \quad \text{Equation 2.31}$$

$$\text{Organic Pollutant} + OH = \text{Degraded Product} \quad \text{Equation 2.32}$$

$$Fe^{3+} + \text{hv} + OH^{-} = Fe^{2+} + \bullet OH \quad \text{Equation 2.33}$$

Demirezen et al., (2019), studied the photodegradation of amoxicillin using green synthesized iron particles. The results showed that the highest pollutant removal of 99% was achieved at pH 2 and 200minutes reaction time. However, at alkaline pH 8 and 11, the removal efficiencies dropped drastically due to the suspected formation of a passive oxide layer on the surface of the catalyst. This showed the sensitivity of pure iron oxide to pH.

2.5.2.2 Ferrites

Ferrites are compounds synthesized by doping transition metals with iron oxides to form a spinel structure. The most common spinel ferrites include; Fe_3O_4, $CuFe_2O_4$, $CoFe_2O_4$, $MnFe_2O_4$, $NiFe_2O_4$, and $ZnFe_2O_4$. The general formulae of ferrites are $M_xFe_{3-x}O_4$, where M represents transition metal. Ferrites are promising photocatalysts because they have narrow band gaps, are chemically stable and can be easily separated from

solution due to their ferromagnetic properties (Thomas et al., 2021). In addition, spinel ferrites have high adsorption capacities for both cations and anions due to high surface area to volume ratio, which is a desirable catalyst property (Kefeni & Mamba, 2020).

Most mainstream photocatalysts such as TiO_2, ZnS and ZnO face several drawbacks such as; (1) high band gap energy, which requires short wavelengths for photoexcitation, (2) rapid recombination of charge carriers, (3) difficulty in recovery from bulk medium after treatment (Kefeni & Mamba, 2020). Consequently, there is a focus on spinel ferrites since they offer an improvement in photocatalytic activity in the visible light spectrum. Besides, they can enhance the magnetic separation of the photocatalysts.

Zinc ferrite is a p-type semiconductor that belongs to the spinel ferrites family. It has Zn^{2+} occupying a tetrahedral site while Fe^{3+} occupies an octahedral site. Among the spinel ferrites, zinc ferrite showed the highest photocatalytic activity towards dye degradation. The order of performance of the spinel species was Zn > Co > Cu > Ni > Cd > Cr (Kefeni & Mamba, 2020). Furthermore, zinc ferrites can adsorb both cations and anions to its photocatalytic surface, which fastens the degradation rate of any pollutants (Kefeni & Mamba, 2020)

Deficiencies of Ferrites

It is important to note that spinel ferrites have exhibited some major shortcomings, which include; (1) fast recombination of photogenerated charge as observed in $ZnFe_2O_4$, which decreases photocatalytic performance; (2) Zinc ferrites suffer from photo-corrosion effects in the presence of light; (3) highly acidic or alkaline environment limits their photocatalytic efficiencies; (4) leaching of Zn^{2+} and Fe^{3+} (Sonu

et al., 2021). These shortcomings need to be addressed for spinel ferrites to offer alternative wastewater treatment away from traditional photocatalysts.

2.5.2.3 Methods of Improving Spinel Ferrites

a) Construction of Heterojunction with photocatalyst

Heterojunctions are interfaces between two semiconductors characterized by uneven band structures and some generated band orientations (Sonu et al., 2021). Coupling a p-type spinel ferrites to a n-type semiconductor to form a type-II heterojunction is a promising way of decreasing charge recombination (Palanivel et al., 2019). This is because, at the junction interface, there exists a difference in chemical potential between the two semiconductors, leading to band bending (Jindal et al., 2021). Consequently, an inbuilt electric field is created, which decreases the electron-hole pairs recombination by driving the respective charges in opposite directions which increases the redox potential of the photocatalyst (Chowdhury et al., 2021; Kumar et al., 2020).

Heterojunctions formed by $ZnFe_2O_4$/g-C_3N_4 can be either Type II or Z-scheme heterojunctions. The heterojunction type depends on the band edge positions of the coupled semiconductors (Kumar et al., 2020). For instance, the Z-scheme is a derivative of the type-II heterojunction and is formed as a result of surface defects in $ZnFe_2O_4$/g-C_3N_4 structure. This causes an energy bend in the photocatalyst, hence realignment of band edge positions (Palanivel et al., 2019). Table 2.1 compares the band gaps of g-C_3N_4 and $ZnFe_2O_4$ with common semiconductors and superoxide radicals.

Table 2.1: Conduction band/valence band potentials of various semiconductors

Photocatalyst	Conduction Band(eV)	Valence Band(eV)	Source
g-C_3N_4	-1.1	+1.6	(Darkwah & Ao, 2018)
$ZnFe_2O_4$	-1.5 +0.27	+0.4 +2.16	(Kumar et al., 2020; Palanivel et al., 2019)
ZnO	-0.3	+2.94	(Sun et al., 2018)
TiO_2	-0.32	+2.88	(Sun et al., 2018)
ZnS	-1.04	+2.56	(Hayat et al., 2021)
H_2O/•OH	+1.99		(Palanivel et al., 2019)
O_2/•O_2^-	-0.33		(Palanivel et al., 2019)

b) Working Mechanism of Heterojunction

For type II heterojunction, visible light irradiation generates electrons/hole pairs in g-C_3N_4 and $ZnFe_2O_4$. Figure 2.4 shows a type-II heterojunction for g-C_3N_4 and $ZnFe_2O_4$. Its reaction scheme involves electrons generated by $ZnFe_2O_4$ (CB = -1.5eV) are repelled by the high negative charge and migrate through the heterojunction to the conduction band of g-C_3N_4 (CB = -1.1eV), which is less negative (Borthakur & Saikia, 2019). Reduction of oxygen molecules to yield superoxide can now occur at the surface of g-C_3N_4 CB since its reduction potential is higher than that of oxygen molecules. However, the holes are repelled by the valence band of g-C_3N_4 (VB = +1.6eV) and transferred to the $ZnFe_2O_4$ (VB = +0.4eV) valence band that has less positive charge. However, photooxidation reaction is impossible at $ZnFe_2O_4$ valence band because oxidation potential is less than the standard redox potential of H_2O/·OH (Chowdhury et al., 2021). Therefore, this charge transfer process across the heterojunction leads to charge separation, hence a decrease in recombination of photogenerated charge (Chen et al., 2016).

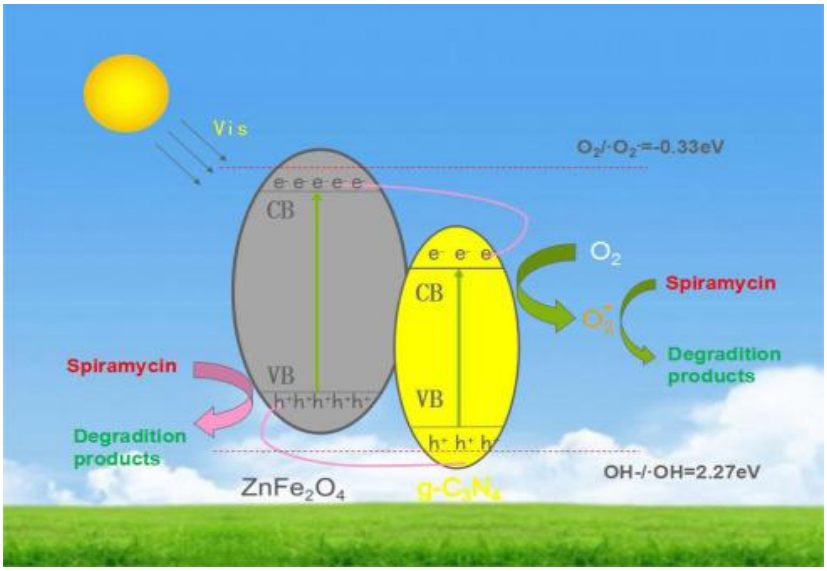

Figure 2.4: Type II heterojunction between $ZnFe_2O_4$/g-C_3N_4 (Chen et al., 2016)

The possible reaction mechanism of the composite with a dye is illustrated as follows;

$H_2O = H^+ + OH^-$ ……..……..…… Equation 2.34

$ZnFe_2O_4$/g-C_3N_4 + hv = (h+) + (e-)…….....…. Equation 2.35

O_2 + e- = $^{\bullet}O_2^-$…….....……..…… Equation 2.36

e- + $\bullet O_2^-$ + $2H^+$ =H_2O_2…….....…… Equation 2.37

$^{\bullet}O_2^-$ + H_2O_2 = $\bullet OH^{\cdot}$ + OH-…….....…… Equation 2.38

OH^- + h^+ = •OH …….....…… Equation 2.39

•OH + dye = degraded pollutant…….....…… Equation 2.40

$^{\bullet}O_2^-$ + dye = degraded pollutant…….....…… Equation 2.41

2.5.2.4 Graphite carbon nitride

Recently, there has been attempt to reduce the metal content in photocatalysts to reduce the potential risk of heavy metal pollution. Hence, non-metal semiconductors such as graphite carbon nitride are increasingly explored. G-C_3N_4 has favorable properties such as; a moderate band gap energy, and is sensitive to visible light up to 460nm. Furthermore, it has suitable conduction and valence bands for oxidation and is a metal-free n-type semiconductor (Ismael, 2020). The band gap energy of graphite carbon

nitride is 2.7eV, and the energy location of its conduction and valence band is -1.1 and +1.6eV, respectively (Darkwah & Ao, 2018). Moreover, it has the dual advantage of eliminating pollutants through a synergistic mechanism of adsorption and photocatalysis. Due to these desirable properties, g-C_3N_4 is a promising green photocatalyst.

Graphite carbon nitride can be synthesized through various routes. They include; hydrothermal treatment, solvothermal treatment, solid-state reactions, chemical vapor deposition and physical vapor deposition. Nitrogen-rich precursors such as; melamine, cyanamide, urea and thiourea are polymerized in the synthesis reactions (Darkwah & Ao, 2018). The resultant compound is in bulk form and has a layered 3-D planar structure, just like graphite.

However, bulk graphite carbon nitride has the following drawbacks: (1) has high rates of recombination of photogenerated charge carriers, (2) has low specific surface area, (3) has poor quantum yields due to limited electronic transitions. These drawbacks stem from structural defects due to stacking of g-C_3N_4 layers during poly-condensation (Rono et al., 2020).

However, the bulk layers can easily be separated into 2-D structures when sufficient energy is applied to break weak van der Waal forces between the layers. Various studies have synthesized ultrathin nanosheets from bulk g-C_3N_4 using exfoliation techniques. The exfoliation strategies commonly used include; chemical exfoliation using strong acids, ultrasonic exfoliation using methanol solution and thermal exfoliation using high temperatures (Rono et al., 2020). The resultant nanosheets have higher specific surface area, hence increased reaction sites. Furthermore, they have lower recombination rates of electrons/holes due to reduced diffusion paths, hence better electronic properties.

Thus, exfoliation of bulk g-C_3N_4 to form nanosheets effectively improves its photocatalytic activity.

2.6 Motivation for Selecting Heterogeneous Photocatalysis

Heterogeneous photocatalysis has displayed various benefits as compared to other advanced oxidation processes. They include; (1) the process is environmentally friendly and has little consumption of chemicals, (2) complete mineralization of recalcitrant compounds can be realized, (3) the process is economical since it requires simple equipment features and it can use solar energy as opposed to UV, (4) the process can operate at wide pH range (Ahmed et al., 2021; Sun et al., 2018). These advantages make heterogeneous catalysis an attractive method unlike other AOP processes.

Among the heterogeneous photocatalysts, conventional photocatalysts such as; ZnO, TiO_2, CdS and ZnS have widely been studied and have shown superior photocatalytic activity. However, some drawbacks exist that limits their commercial applications, such as; (1) Large band gap energy, hence only sensitive to UV-light; (2) Some catalyst like ZnO are amphoteric and must operate at neutral pH; (3) Difficulty in catalyst recovery at the end of treatment. This approach necessitates immobilization of photocatalysts in solid supports, which decreases their active area (Palanivel et al., 2019; Wang et al., 2020). Consequently, researchers have explored other alternative photocatalysts.

Nevertheless, single photocatalytic systems have inadequate photocatalytic performance and are often inferior to multicomponent photocatalysts (Duc et al., 2023). Therefore, there is an increasing trend to combine multiple photocatalysts to form composites. The heterojunctions formed by the composite are potentially effective due to their effective separation of photogenerated charges and the synergistic effects of using multiple catalysts (Sun et al., 2018). This research focused on constructing a

heterojunction between zinc ferrite and graphite carbon nitride. Two factors influenced the choice of the two semiconductors; (1) charge separation, a zinc ferrite-graphite carbon nitride combination forms a p-n type-II/z-scheme heterojunction which can maintain a highly oxidative valence band and a highly reductive conduction band that can efficiently generate reactive oxygen species, (2) Extension of visible light spectrum, the composite of zinc ferrite/graphite carbon nitride can absorb solar radiation upto 600nm this is due to bathochromic shift that is facilitated by zinc ferrite (Kefeni & Mamba, 2020).

2.7 Summary of Literature Review and Knowledge Gaps

Based on the literature review, several contaminants of emerging concern were identified at the outlet of different WWTPs. Some known recalcitrant pollutants such as carbamazepine, sucralose and atrazine resisted degradation in various conventional systems (K'oreje et al., 2018; Sgroi et al., 2018; Shukla & Ahammad, 2023). This pointed out to some knowledge gaps in regards to removal of recalcitrant pollutant. Different advanced oxidation methods were explored. For instance, chemical advanced oxidation methods involving ozone, hydrogen peroxide, electrochemical oxidation, Fenton process, ultrasonication and irradiation, which showed high efficiencies in degrading pollutants. However, some notable drawbacks were identified such as; requirements of low pH and leaching of catalyst for Fenton process, high chemical requirements for ozone process, low degradation efficiency for Ultrasonication when used alone. Some of these deficiencies in literature were addressed by employing a combination of methods and development of solid-based catalysts to address leaching. For photochemical processes, emphasis was on heterogeneous photocatalyst. Graphite carbon nitride was explored in detail as a potential photocatalysts. Its key advantages included; photosensitive to visible light, chemical stability, ease of synthesis from

precursor materials and is metal-free. However, g-C_3N_4 still had limitations, which hindered its applicability as a potential post-treatment method. The photocatalyst had rapid recombination of charge carriers, this shortcoming was addressed by doping with zinc ferrite in the research. Pristine g-C_3N_4 had a low surface area; this drawback was addressed by ultrasonic exfoliation of the catalyst to form nanostructures. Besides, the semiconductor was mostly studied using dyes as a model pollutant (Wang et al, 2022). Therefore, more studies were needed with emerging pollutants. Finally, despite g-C_3N_4 being photosensitive in visible light, it had poor light absorption. This drawback was addressed by dye-sensitization and the construction of a heterojunction with $ZnFe_2O_4$. Furthermore, few studies in literature have assessed the effects of dye-sensitized semiconductors since majority of studies focus on solar cells and water splitting (Zhang et al., 2020).

CHAPTER 3

MATERIALS AND METHODS

3.1 Materials

All reagents used in this study were of analytical grade and used without any further purification. Melamine powder (Sigma-Aldrich), deionized water, dilute ammonia solution, Iron (III) chloride hexahydrate (Sigma-Aldrich), Zinc (II) chloride dehydrate (RD HAEN), Eosin Y-dye (Kobian Chemicals), Ethanol, tetracycline (Universal Corporation), 0.2M HCl (Kobian chemicals), 0.2M NaOH (Kobian chemicals), NaCl, Na_2SO_4, $NaNO_3$

3.2 Equipment

Ultraviolet vis spectrophotometer (UV-1800, Shimadzu), digital weighing balance (Scaltec, Germany), centrifuge (Itettich Zentrifugen, Germany), muffle furnace (Carbolite Gero Furnace, ELF 11/14), TOC/TN analyzer (Multi N/C 2100, Analytica Jena), magnetic stirrer (Pro Scientific), Solar radiometer (PCE-SPM1, PCE instruments), Portable pH/conductivity meter (Sension+PH3, HACH), oven (Daihan Labtech, LDO-150), turbidimeter (Paqualab^{TM} Photometer, ELE International), solar parabolic reactor, digital pen thermometer, light meter and peristaltic pump

3.3 Synthesis of Photocatalyst

3.3.1 Preparation of g-C_3N_4

Graphite carbon nitride (g-C_3N_4) was synthesized using methods adapted from (Jo et al., 2020; Rong et al., 2020; Xu et al., 2018). The modification implemented were thermal and ultrasonic exfoliation of bulk graphite carbon nitride to obtain nanosheets. In a typical experiment, 20 grams of melamine powder was placed in a closed alumina crucible. The crucible was then heated at 550^{o}C at a heating rate of 5^{o}C/minute for 4hours in a furnace. The resultant product was then finely ground into powder and then

reheated to 550^{o}C for 2hours in open air to obtain g-C_3N_4 nanosheets. The graphite carbon nitride formed was then ultrasonically dispersed in 200ml of water for 15hours. The resultant suspension was then centrifuged at 150 rpm to aid in the separation of any un-exfoliated graphite carbon nitride. The supernatant solution was then oven dried at 70^{o}C for 24hours to obtain pure graphite carbon nitride. The obtained graphite carbon nitride was then ground into fine powder.

3.3.2 Preparation of $ZnFe_2O_4$/g-C_3N_4

The preparation of $ZnFe_2O_4$/g-C_3N_4 photocatalyst followed a coprecipitation procedure with the method adapted from (Jo et al., 2020; Renukadevi & Jeyakumari, 2020; Rong et al., 2020). In a typical experiment, 20grams of graphite carbon nitride were ultrasonically dispersed for 30minutes in 100ml of water. $FeCl_3.6H_2O$ (0.0124M) and $ZnCl_2.2H_2O$ (0.0248M) were then added to the graphite carbon nitride and then stirred using a magnetic stirrer for one hour. After the metal salts dissolved completely, the reaction mixture was then heated at 80^{o}C. Ammonium hydroxide was then added drop-wise periodically to adjust pH to 10 to aid in precipitation. The mixture was then stirred for another 4hrs and then allowed to precipitate. The generated precipitate was then washed first with deionized water, followed by ethanol for three times and then dried at 80^{o}C overnight in a vacuum oven. Finally, the synthesized composite was annealed at 500^{o}C for 2hours to improve the crystal structure. Other hybrids of $ZnFe_2O_4$-g-C_3N_4 were synthesized using the same procedure at different weight ratios of 5, 15 and 25%.

3.3.3 Dye sensitization of $ZnFe_2O_4$/g-C_3N_4

The dye sensitization experiment used mixing and adsorption with the method adapted from (Chen et al., 2021; Musa & Gaya, 2019). In a typical experiment, 10grams of photocatalyst was added to 100ml of ethanol solution and then stirred magnetically for thirty minutes to ensure even mixing. Half a gram of Eosin Y dye was then added to

the slurry and then stirred for 24hours. The resultant solid residue was subsequently rinsed thrice with deionized water, followed by 99% ethanol. The washed solid precipitate was oven dried at 80ºC for 8hours to obtain dye sensitized photocatalyst which was then stored in amber bottles. Figure 3.1 summarizes the process route used in synthesizing the photocatalysts.

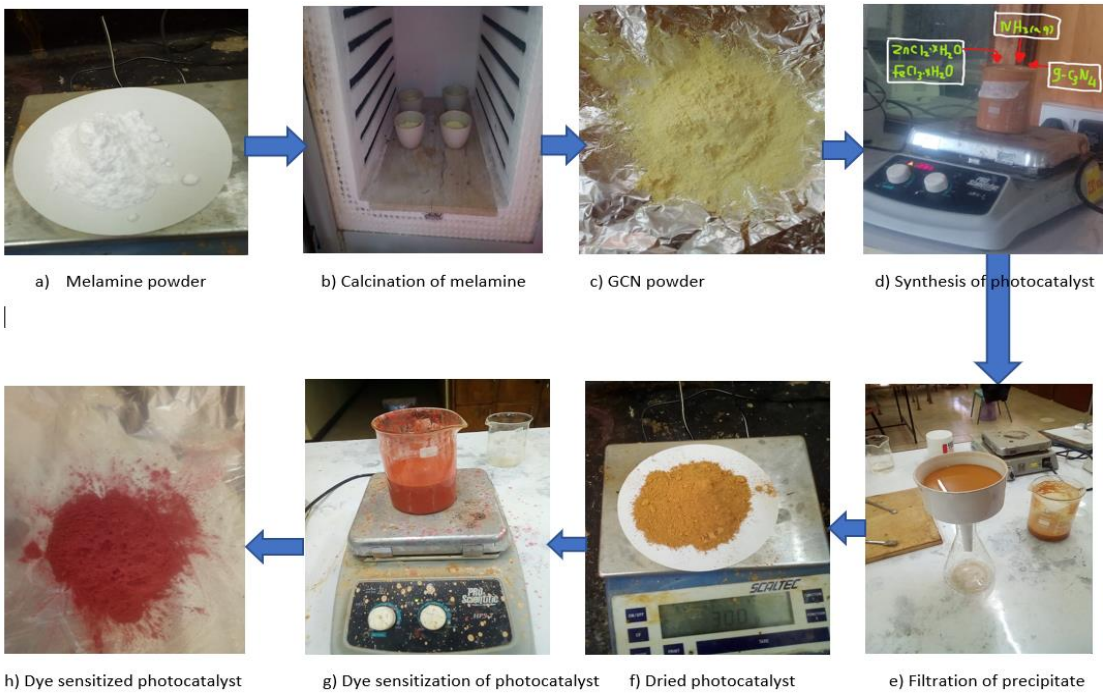

Figure 3.1: A summarized process route used in synthesizing of photocatalyst (5, 15 and 25% ZF-GCN and EY-25%-ZF-GCN)

3.4 Characterization of Photocatalysts

3.4.1 XRD

The crystalline structure and patterns of the photocatalysts were analyzed using a Rigaku Altima III X-ray diffractometer equipped with Cu Kα radiation (λ=1.54178Å) at a scanning angle of 10-90º. The average crystallite sizes of the five composites were calculated using the Debye-Scherrer equation given by Equation 3.1 (Mekonnen, 2022).

$$D = \frac{K\lambda}{\beta cos\theta} \quad ---------- \quad Equation\ 3.1$$

Where D=crystallite size, K=shape factor of sphere taken as 0.9, β=full width at half maximum (FWHM) radians, λ=X-ray wavelength (0.154178nm), θ= Braggs angle.

3.4.2 FTIR

The functional groups and their vibration modes were determined using a Fourier transform infrared spectrometer (FT-IR, PerkinElmer Frontier) for the range 4000-500cm^{-1}.

3.4.3 SEM-EDX

The morphology, microstructure and the chemical composition of the photocatalyst was determined using a scanning electron microscope (SEM) equipped with an energy dispersive X-ray spectroscopy (SEM-EDS, Zeiss-Ultra 55) operating at 3KV. SEM is a procedure that involves focusing a strong electron beam on a sample. This causes electrons to interact with the surface so as to obtain the surface topography and microstructure of a sample.

3.4.4 UV-Vis

The optical absorption properties of the photocatalyst were determined using a UV-vis absorption spectrophotometer (Shimadzu, UV-1800) for the range 200-800 nm. A small sample of the photocatalyst was first ultrasonically suspended using distilled water in a 100ml beaker. This was then followed by a UV-vis wavelength scan in the 200-800nm wavelength. A tangent line was drawn from the descending absorption spectrum to obtain the tail absorption edge which can be used to calculate the band gap energy according to Equation 3.2 (Mecha et al., 2016; Mekonnen, 2022):

$$E_g = \frac{1240eV}{\lambda_{max}} \quad \text{---------- } Equation\ 3.2$$

3.4.5 PL-Spectra

The photoelectronic properties of the photocatalysts were determined using a photoluminescence spectrum (PL, Horiba LabRam HR) at an excitation wavelength of 266 and 550 nm.

3.5 Experimental Design

Design-Expert®13 software was used to generate the experimental design matrix and analyze the mathematical models. The RSM method is a statistical modelling approach that uses multiple regression to design experiments, study the interaction between the independent variables and predict the optimum parameters (Khoshnamvand et al., 2018; Marizcal-barba et al., 2022).

CCD was used to study the effect of three independent variables and their response to degradation and TOC removal. The variables are pollutant dose (A), pH (B) and catalyst dose (C). Each factor had 5-levels summarized in Table 3.1.

Table 3.1: Experimental levels and range of independent variables

	Levels				
Variables	-α (1.68)	-1	0	1	+α (1.68)
A: Pollutant Dose (mg/l)	4.88	10	17.5	25	30.11
B: pH	1.954	4	7	10	12.054
C: Catalyst Dose (g/L)	0.127	0.4	0.8	1.2	1.47

The annotations (-α) and (α) represent the extreme low and high levels while (0) is the center points for the five-level factorial design.

Pollutant degradation and TOC Removal were the two responses measured and used in generating separate regression equations. The mathematical relationship between the response (Y) and the chosen process variables was fitted using a general second order polynomial equation expressed as shown in Equation 3.3 (Abid et al., 2019).

$$Y = \beta_o + \sum_{i=1}^{3} \beta_i X_i + \sum_{i=1}^{3} \beta_i^2 X_i^2 + \sum_{i=1}^{3} \sum_{i=1}^{3} \beta_{ij} X_i X_j + \varepsilon ----Equation\ 3.3$$

Y = predicted response, β_o, β_i, β_i^2, β_{ij} are the constant coefficients, X_i are the independent variables and ε the experimental error. These coefficients were determined from the regression model obtained from Design expert and used to generate the

predicted responses (D. Zhang & Wang, 2018). Statistical analysis was then carried out for the fitted models using; ANOVA, residuals, p-value, F-value and adequate precision.

3.6 Desirability Function

The desirability function is a mathematical technique for calculating the optimal parameters for multiple responses. This method determines the global desirability by averaging the desirability function for each response using numerical optimization approach (Hosseini et al., 2022).

3.7 Sample collection and characterization of wastewater

The wastewater sample was collected from the exit point of pond 4 of the Moi University, WWTP using a 20l jerrycan. The sample was then transported immediately to the lab, filtered with a vacuum pump using a 45µm Whatman filter paper and stored at 4^{o}C. The temperature was determined at the sampling point from collected samples using a digital thermometer. The pH and conductivity of the sample were determined using a portable pH/conductivity meter. The turbidity was measured in the Civil engineering lab using a turbidimeter. The total organic carbon and total nitrogen were analyzed at the Chemical engineering labs using a TOC/TN analyzer.

3.8 Experimental Setup

The solar parabolic trough reactor (PTR) setup used in conducting the experiments is shown in Figure 3.2. The photoreactor consisted of a collector made of transparent borosilicate glass tube (diameter: 25mm, length: 80cm, thickness: 2mm) and an aluminum reflector. The collector was connected to a storage tank by plastic pipes and fittings. A magnetic stirrer was fitted below the feed tank to ensure the photocatalyst remains in suspension.

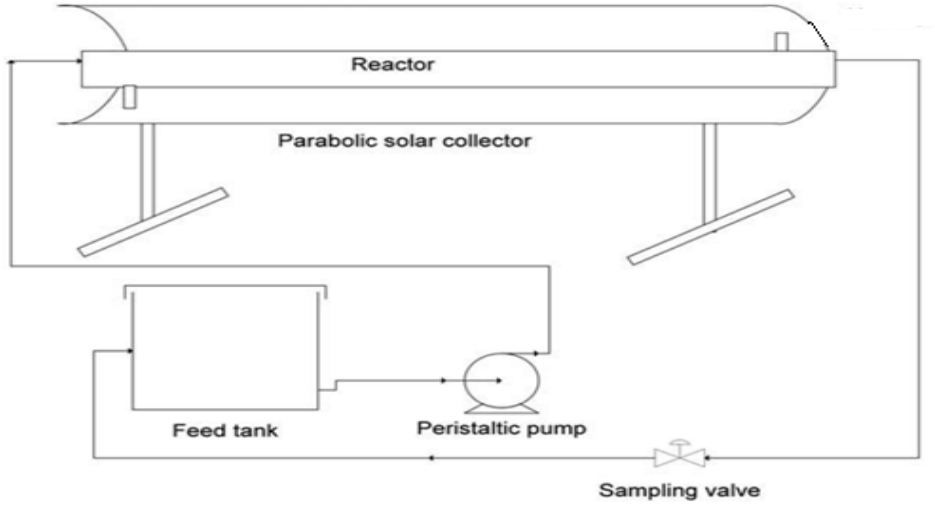

Figure 3.2: Setup diagram of the PTR reactor used in the experiments (Mecha et al., 2016)

3.9 Photocatalytic Experiments

The experiment was conducted during the sunny days of January -May 2023, at a solar irradiance of between 900-1050W/m^2. For a typical experiment, 0.7g of photocatalyst was mixed with 10mg/l of tetracycline dissolved in 1.5L of distilled water. The resultant mixture was then magnetically stirred for 15 minutes in a dark room to establish the adsorption-desorption equilibrium. The solution was then circulated around the PTR using a peristaltic pump at a flowrate of 1 LPM. A 5ml sample was then drawn at periodic intervals of 0, 30, 60 and 90minutes. The sample was then centrifuged and filtered using a 0.45µm syringe filter. The collected sample was then measured at 358nm (max absorbance for tetracycline) using a UV vis spectrophotometer. The concentration of tetracycline was then determined from the UV absorbance curves calibrated based on De Beers' law. The collected samples were also analyzed for total organic carbon using a TOC analyzer to confirm the degree of mineralization. Finally, the effects of coexisting ions such as (Cl^-, NO_3^- and SO_4^{2-}) was studied by dosing 100, 300, 500mg/l concentration of salts in the real waste water containing 20mg/l tetracycline and then comparing with blanks.

The tetracycline degradation efficiency was calculated according to Equation 3.4;

$$Degradation\ Efficiency(\%) = \frac{C_o - C_t}{C_o} * 100 - - - - - - - - - - - Equation\ 3.4$$

The degradation kinetics were analyzed using the pseudo-second order Equation 3.5:

$$\frac{1}{C_t} - \frac{1}{C_o} = k_{app} t - - - - - - - - - - - - - - - - Equation\ 3.5$$

where C_o= initial concentration, C_t= Concentration at time t (mg/l), k_{app}=apparent kinetic constant ($mg^{-1}.L.min^{-1}$)

The mineralization efficiency was determined by the Equation 3.6;

$$TOC\ removal\ (\%) = \left(1 - \frac{TOC_t}{TOC_o}\right) * 100 - - - - - - - - - Equation\ 3.6$$

where TOC_o= Initial TOC concentration, TOC_t= Final TOC concentration, mg/l

3.10 Limitations and Assumptions of the study

This study relied on natural sunlight, subject to solar intensity fluctuations due to cloud overcasts. Therefore, only sunny days were chosen to limit the influence of weather patterns on the experiments. The experiment was continuously monitored with a solar radiometer at an intensity of 900-1050W/m^2, and in case of cloud overcasts lasting more than 10 minutes the experiment was discarded.

The Moi University WWTP was conveniently sampled as a source of the wastewater matrix due to easy accessibility. It was assumed that the complexity of its water matrices is similar to that of a typical UWWTP.

CHAPTER 4

RESULTS & DISCUSSIONS

4.1 Characterization of the As-Synthesized Photocatalysts

4.1.1 Structural Analyses of Photocatalyst

a) XRD Analyses

The XRD patterns for pure g-C_3N_4, $ZnFe_2O_4$, and their hybrids were recorded at angle 2θ for the range between 10-90°, as shown in Figure 4.1.

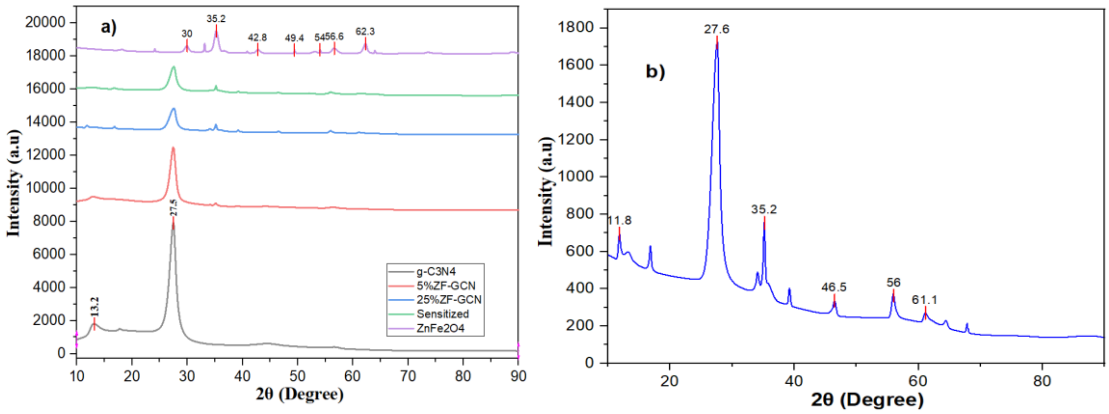

Figure 4.1: (a) XRD diffraction patterns for g-C_3N_4, $ZnFe_2O_4$ and hybrids (5%ZF-GCN, 25%ZF-GCN, EY-25%ZF-GCN) (b) 25%ZF-GCN showing the diffraction peaks of both photocatalysts

Pure g-C_3N_4 had a characteristic intense peak at 27.5°, this peak corresponds well to a width of 0.326nm and represents the crystallographic plane (002) according to (JCPDS98-1526) (L. Chen et al., 2016). This diffraction plane represents the interlayer packing of the graphitic melon network present in g-C_3N_4. Similarly, another smaller peak at 13.2° was observed in g-C_3N_4. This peak was indexed in the crystallographic plane (100) and was as a result of repeated s-triazine units packing. These results were within the literature values for g-C_3N_4, since most studies have found g-C_3N_4 to have two diffraction peaks ranging from 12.8-13.41° and 27.2-27.8° (Borthakur & Saikia, 2019; Jo et al., 2020).

Moreover, for $ZnFe_2O_4$ a series of small intense diffraction peaks were observed at 30.1°, 35.2°, 42.8°, 49.4°, 53.5°,56.6° and 62.3°. These peaks were well matched with the spinel ferrite structure (JCPDS77-0011) of crystallographic planes of (220), (311), (400), (422), (511), and (440) (Rong et al., 2020). Additionally, no impurity phases of Fe_2O_3 were identified in $ZnFe_2O_4$, which was evidence for the successful synthesis of the spinel ferrite structure and high degree of crystallinity. On the other hand, most diffraction peaks attributable to both pure $ZnFe_2O_4$ and g-C_3N_4 could be observed in the XRD patterns of the composites as shown in Figure 4.1b. However, for the 5%ZF-GCN composite only the 35.2° $ZnFe_2O_4$ peak could be observed, this agrees with literature since low quantities of $ZnFe_2O_4$ may not be detected by the XRD (Basaleh, 2021). Hence, the existence of both phases in the composites was evidence of the successful incorporation of $ZnFe_2O_4$ nanoparticles in the crystalline structure of g-C_3N_4, thus successful construction of the heterostructure.

Table 4.1 shows the crystallite sizes of the as-prepared photocatalysts.

Table 4.1: Average Crystallite size of photocatalysts

Photocatalyst	**2θ**	**FWHM**	**D(nm)**
g-C_3N_4	27.48	1.51334	5.103
$ZnFe_2O_4$	35.2	0.89038	8.511
5%ZF-GCN	27.48	1.34715	5.732
25%ZF-GCN	27.6	1.66573	4.635
Sensitized	27.56	1.59701	4.835

These results confirmed the formation of nanoparticles since the average crystal size ranged between 4.63-8.51nm. These values were comparable to the average crystallite size results obtained by Saeed et al. for $Mn_{0.6}Zn_{0.4}Fe_2O_4$/g-C_3N_4 photocatalyst which ranged between 5.8-6.96nm (Saeed et al., 2021).

Interestingly, the result show that by increasing the percentage of $ZnFe_2O_4$ in the composite there was significant suppression of g-C_3N_4 peaks while the intensity of $ZnFe_2O_4$ peaks steadily increased (Basaleh, 2021; Chen et al., 2016). For instance, the 13.2^o peak was almost completely diminished in the 25%ZF-GCN composite. Similarly, on close examination of the composite peaks, there was a slight shift to higher diffraction angles, which has also been reported in literature (Palanivel et al., 2019). Likewise, the g-C_3N_4 peak shifted slightly from 27.5^o to 27.6^o. These observations could suggest that by creating the heterostructure, there is a remarkable decrease in the overall crystallinity and dispersibility of the composite (Renukadevi & Jeyakumari, 2020). Moreover, these occurrences could be explained by the possible guest-host interaction between g-C_3N_4 and the metal ions. Nonetheless, the XRD spectra of Eosin Y-sensitized (25%ZF-GCN) and the unsensitized (25%ZF-GCN) hybrids were almost identical. This could imply that dye-sensitization at small concentrations has little effect on the crystalline structure of the composite, and they interact through van der waal or hydrogen bond as reported for similar studies involving dye-sensitization (You, 2016).

b) FTIR Analyses

The results for FTIR analysis for pure g-C_3N_4 and its composites gave intense peaks at 808cm^{-1} as shown in Figure 4.2.

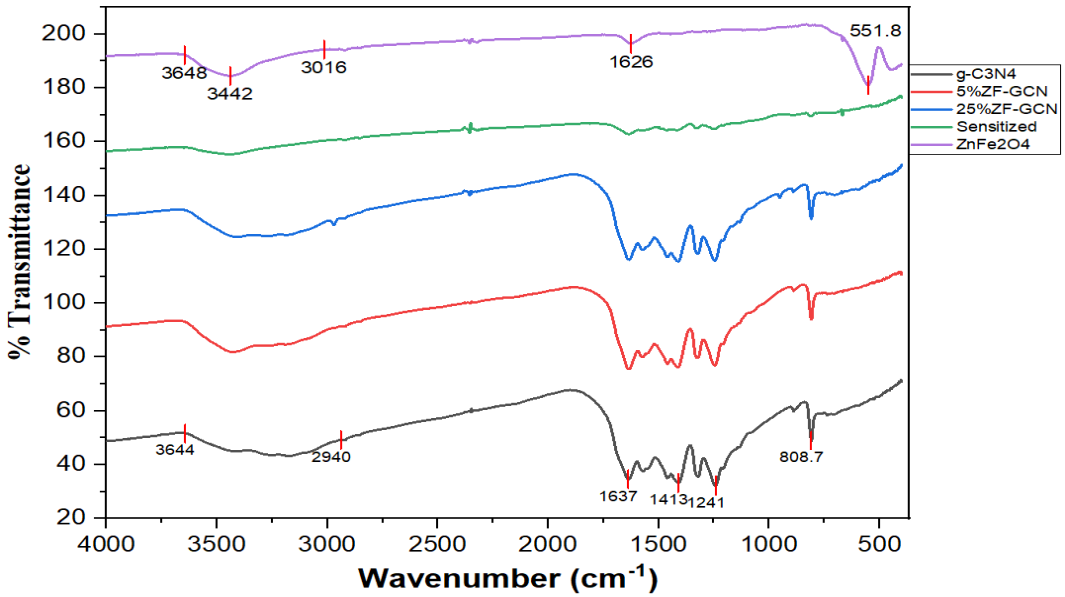

Figure 4.2: FTIR Spectra Analyses for g-C_3N_4, $ZnFe_2O_4$ and hybrids (5%ZF-GCN, 25%ZF-GCN, EY-25%ZF-GCN)

This was due to the stretching mode of carbon-nitrogen heterocycles attributed to the breathing mode of the s-triazine rings (Huang et al., 2020). Additionally, for g-C_3N_4 and its composites other characteristics peaks were noticed in the region between 1200-1600cm^{-1} region with specific peaks at 1241, 1325, 1413, 1455 and 1637cm^{-1}. These series of peaks were attributed to the aromatic stretching vibration of C=N heterocyclic ring as a consequence of heptazine repeating units (Gao & Wang, 2020). Also, another broad absorption peak was observed at between 2940-3644cm^{-1}. This could be due to the vibration of NH and NH_2 terminal groups at defect size or the breathing mode due to adsorbed water molecules (Li et al., 2022).

On the other hand, for $ZnFe_2O_4$, characteristic intense speaks were identified at 3442cm^{-1} and 1626cm^{-1}. These could be attributed to the vibration of the OH group on its surface due to the adsorbed water molecules. Besides, another intense peak was observed at 551.8cm^{-1} on the surface of $ZnFe_2O_4$. This is due to vibrational stretching of Fe-O due to the bond created between the tetrahedral Fe ion and the oxygen ion

(Jangam et al., 2021). Interestingly, it was observed that the composites possessed peaks for both photocatalysts however at intensities proportional to the concentration. This could be evidence of the successful incorporation of $ZnFe_2O_4$ in the g-C_3N_4 heterostructures. Similarly, the dye-sensitized composite displayed highly diminished peaks as compared to the other composites. This confirms that the Eosin Y structure physically bonded well with the composite.

4.1.2 Morphology and Chemical composition

a) **SEM**

Figure 4.3(A, B) shows the SEM images of g-C_3N_4.

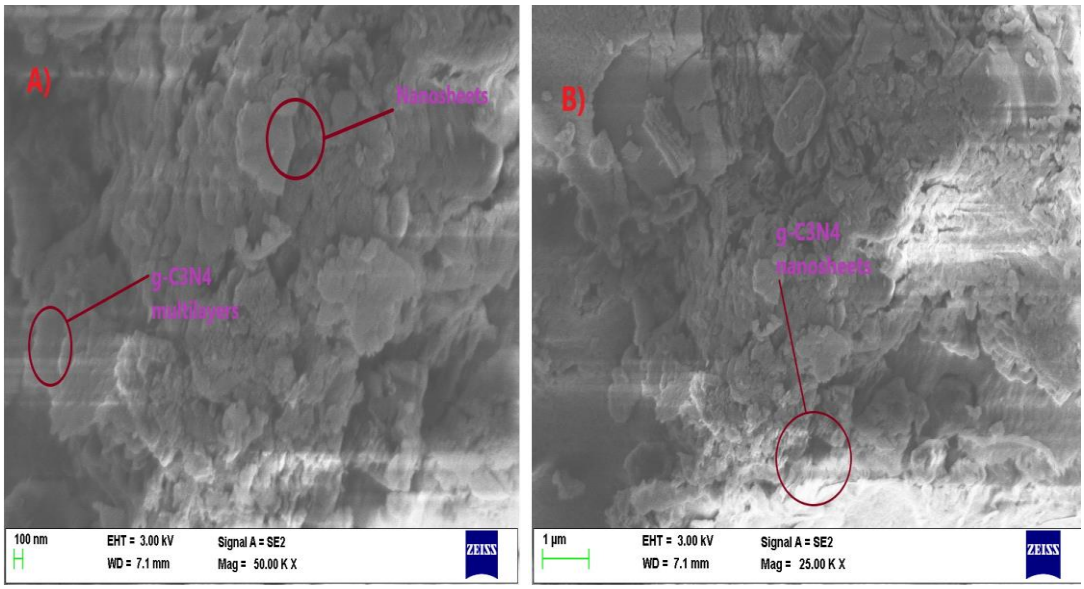

Figure 4.3: SEM images of (A, B) g-C_3N_4

The images showed a mesoporous nanosheets layers which was evidence of successful exfoliation unlike pristine g-C_3N_4 which has been reported to form bulk and multilayers structure (Huang et al., 2020).

Figure 4.4(C, D) shows the $ZnFe_2O_4$ images at different magnification (x100nm and x2000nm).

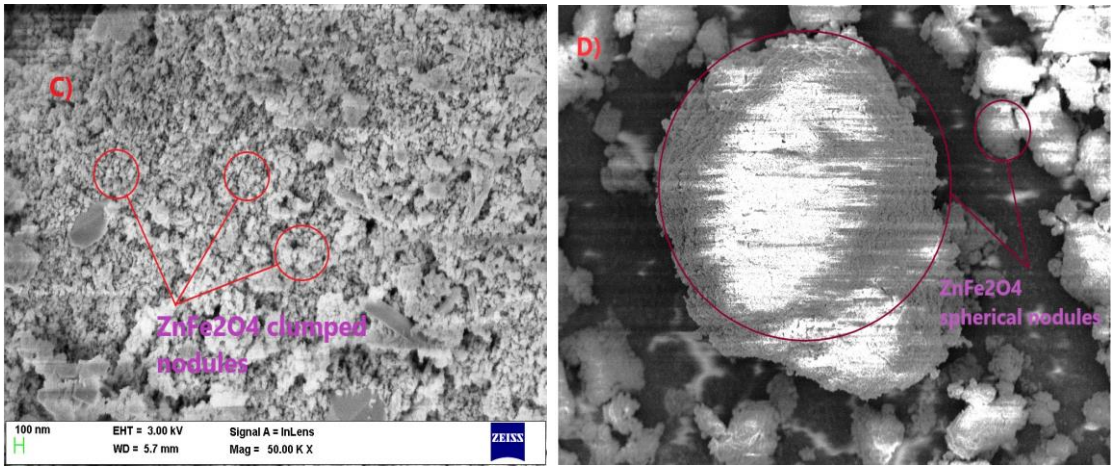

Figure 4.4: SEM images of (C, D) $ZnFe_2O_4$

It can be observed that $ZnFe_2O_4$ particles consisted of almost spherical nodules with a diameter ranging between 30.71nm and 50.97nm. These particles are highly agglomerated and interlock to form clusters, which could be attributed to the magnetic character of spinel ferrites (Jangam et al., 2021; Saeed et al., 2021).

Figure 4.5(E, F) shows the 25%ZF-GCN images at different magnification (x100nm and x1000nm).

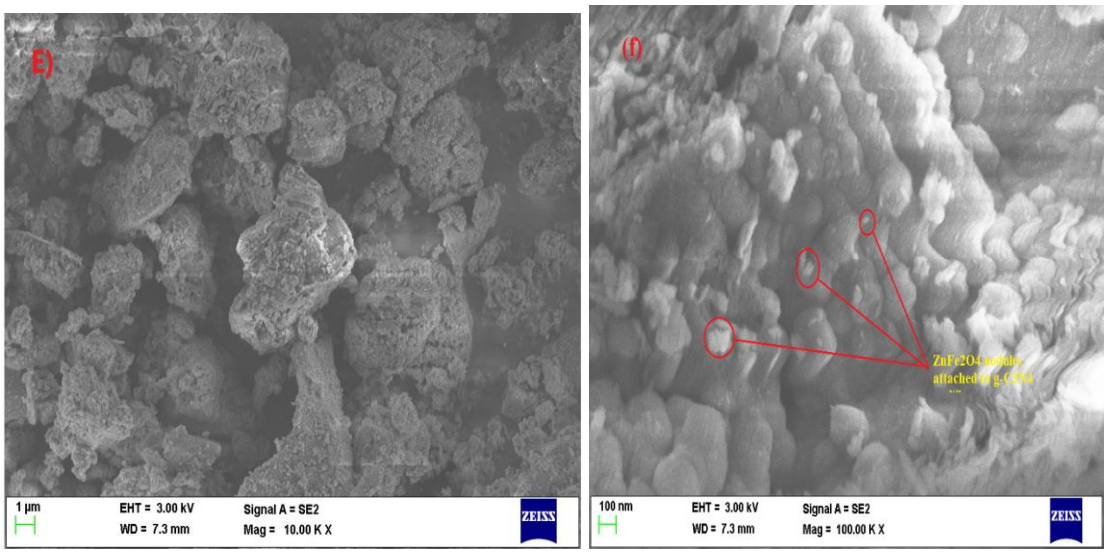

Figure 4.5: SEM images of (E, F) 25%ZF-GCN

It could be observed that $ZnFe_2O_4$ nanoparticles were well dispersed and attached to the sheet like layers of g-C_3N_4 (Basaleh, 2021). Hence, the incorporation of the ferrite

nanoparticles into the nanosheets confirmed the successful creation of the heterojunction between the two photocatalysts.

Figure 4.6(g, h) shows the images for the dye sensitized and 25%ZF-GCN composite.

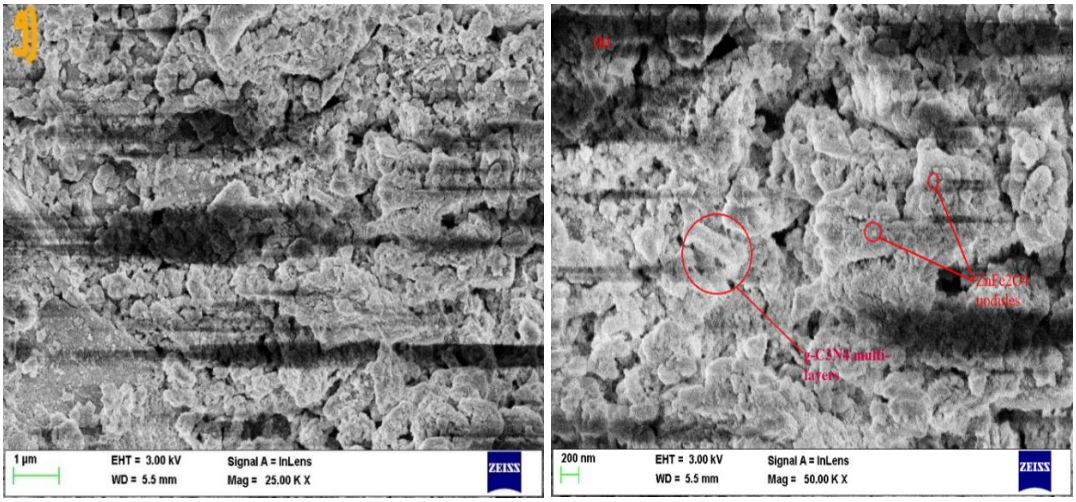

Figure 4.6: (G) Sensitised-25%ZF-GCN (H) 25%ZF-GCN

It is evident that no significant differences in the morphology exists between the dye-sensitized and 25%ZF-GCN composite. This indicates that Eosin-Y could not be detected on the surface of the composite using SEM. Furthermore, a similar study conducted by Chen and co-workers using g-C_3N_4 sensitized by indoline dye reported that the TEM images couldn't detect organic dyes on the surface of a sample (Chen et al., 2021).

b) **EDX Spectra**

The elemental purity of the synthesized photocatalyst was confirmed using Energy Dispersive X-ray spectroscopy (EDX). Figure 4.7a shows the EDX graph of g-C_3N_4, this confirmed its purity since carbon, nitrogen and oxygen peaks were dominant throughout.

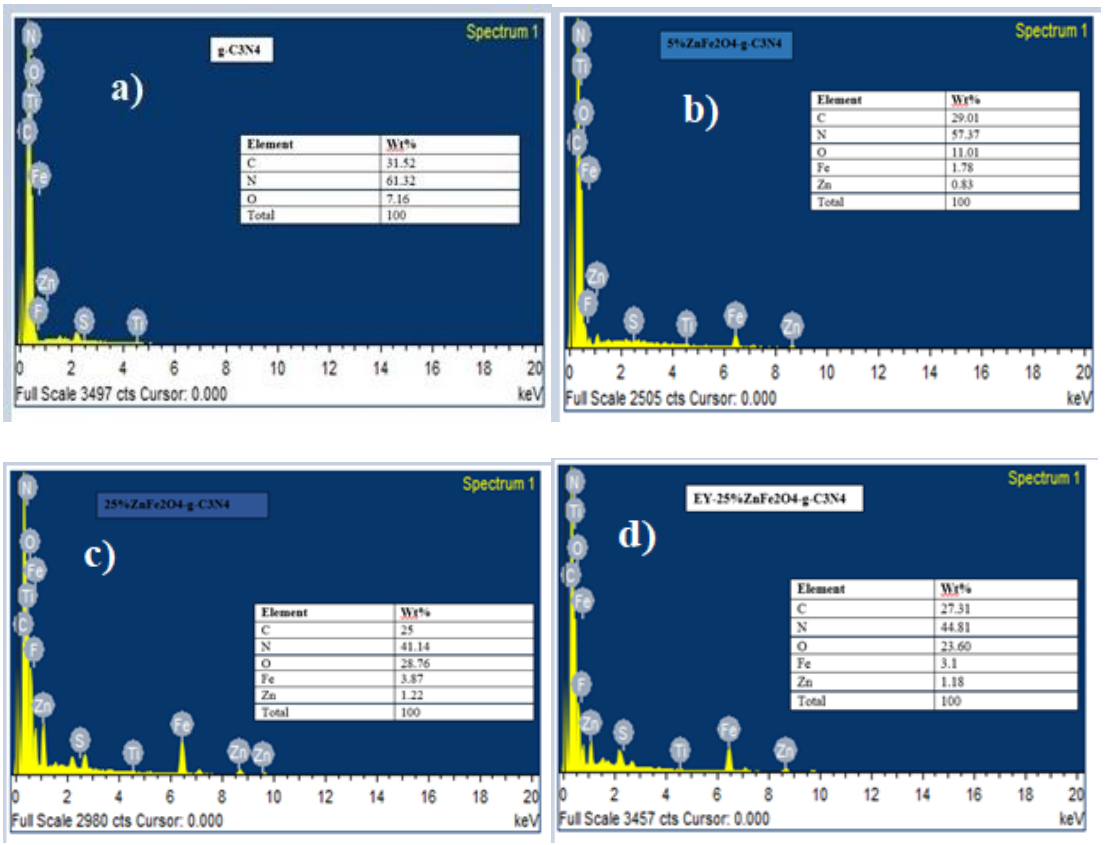

Figure 4.7: EDX images of (a) g-C_3N_4 (b) 5% $ZnFe_2O_4$/g-C_3N_4 (c) 25% $ZnFe_2O_4$/g-C_3N_4 (d) EY-25% $ZnFe_2O_4$/g-C_3N_4

Additionally, for all the composites (5%, 25%ZF-GCN and Sensitized) peaks of carbon, nitrogen, oxygen, iron and zinc were detected, which confirmed the successful formation of the heterostructures. This supported the SEM, XRD and FTIR analyses.

4.1.3 Optoelectronic Studies

a) **UV-Vis absorption Spectra**

A UV-vis spectrophotometer was used to determine the optical absorption of the photocatalyst samples. From Figure 4.8, it was evident that the synthesized composites had enhanced light absorption in the 400-650nm region as compared to either of the pure photocatalyst.

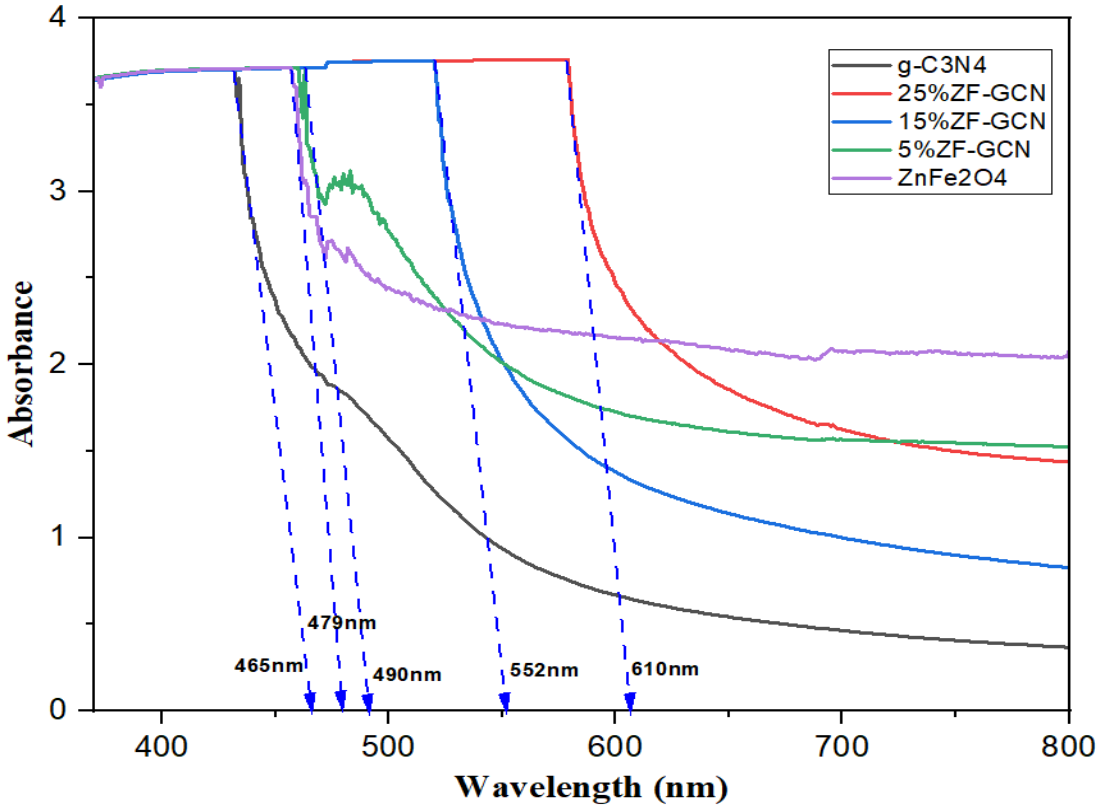

Figure 4.8: UV-vis spectra of graphite carbon nitride and zinc ferrite carbon nitride composite (5%, 15% and 25%)

The thermally exfoliated graphite carbon nitride nanosheets had a tail absorption of 465nm, this agreed with reported literature values (Chen et al., 2016). Interestingly, with increasing concentration of zinc ferrite in the composites there was a gradual red shift in visible light absorption towards higher wavelength. For instance, 5%ZF-GCN, 15%ZF-GCN and 25%ZF-GCN had corresponding tail absorption of 490nm, 555nm and 610nm. This corresponded to approximate band gaps of 2.53eV, 2.23eV and 2.03eV respectively, when calculated using Equation 3.2. This decrease in band gap could be possibly explained by the synergy achieved by creating a heterojunction between two semiconductors, which results in bandgap modulation and thus broadening of the absorption peak.

Similarly, it can also be observed by increasing the ratio of zinc ferrite in the composite there is a narrowing in bandgap, which consequently improves the visible light

absorption (Palanivel & Mani, 2020). Furthermore, there was a corresponding colour change of the composite from the light yellow colour characteristic of graphite carbon nitride to brown as the ferrite content is increased. However, the dye-sensitized composite displayed a similar peak to the 25%ZF-GCN. This could be explained by the maximum absorbance of Eosin-Y is at 550nm whose wavelength is lower than that of the composite, hence doesn't extend the visible range.

b) Photoluminescence Spectra

Apart from extending the visible light absorption spectrum of a photocatalyst, the performance of semiconductors can also be improved further by enhancing charge separation using a heterojunction as well as by inhibiting the recombination rates of electrons/holes pairs. Therefore, to understand the behavior of photo-excited charge mobility, recombination and transfer for the synthesized photocatalysts, photoluminescence studies were carried out. The photoluminescence (PL) measurements produces an emission peak whose intensity is directly proportional to radiative recombination of photogenerated charges (You, 2016). Hence, a stronger PL emission intensity indicates a higher probability for charge recombination while a weaker intensity indicates suppressed charge recombination (Huang et al., 2020). Figure 4.9(a, b) shows the PL spectra for g-C_3N_4, $ZnFe_2O_4$ and their corresponding composites excited at 266nm and 550nm wavelengths.

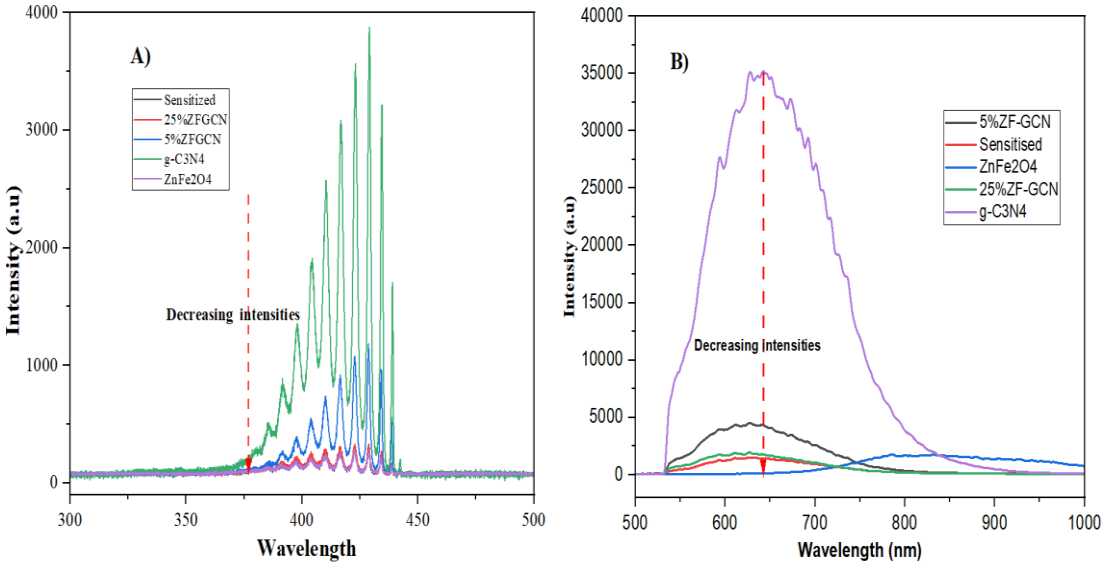

Figure 4.9: Photoluminescence spectra for samples; (A) 266nm and (B) 550nm excitation

It is evident that graphite carbon nitride has the highest PL-spectra intensity which peaks at approximately 435nm and coincides with its band gap energy of 2.85eV. This sharp peak can be attributed to photoexcitation by PL which caused the n->π* electron transition for lone nitrogen pairs in g-C_3N_4 (Oluwole & Olatunji, 2022). Additionally, this phenomenon could be explained by possible radiative recombination of self-trapped charges on the surface of pristine g-C_3N_4 (Gao & Wang, 2020).

Interestingly, when the $ZnFe_2O_4$ content was increased in the composites, the intensity of the emission spectrum reduced significantly. They could be ranked in the following order: g-C_3N_4 > 5%ZF-GCN > 25%ZF-GCN > EY-25%ZF-GCN > $ZnFe_2O_4$. This is evidence that the synthesized composites can successfully inhibit the charge recombination as well as capture the photo-induced charges leading to improved separation as compared to g-C_3N_4. Additionally, the heterojunction created between the two pure semiconductors, resulted in new electron paths used for evacuating electrons and thus reduced the direct recombination of the photoexcited charges (Renukadevi & Jeyakumari, 2020). Besides, there was a notable peak shift of the composite to a higher

wavelength, which revealed the possible band-gap reduction after the creation of the heterostructure.

Finally, the dye-sensitized composite demonstrated lower PL spectra intensity as compared to the 25%ZF-GCN hybrid. This showed the notable improvement in the suppression of charges by dye sensitization and could also explain its slightly higher photocatalytic performance than the latter.

4.2 Optimization of Variables for Degradation of Synthetic Water Containing Trimethoprim

4.2.1 Model Fitting and Statistical Analyses for Trimethoprim

Table 4.2 shows the three-factor CCD matrix table generated by Design Expert software. The experimental values and the corresponding predicted values are shown for degradation and TOC removal as the responses.

Table 4.2: CCD design matrix of operating variables with their actual and predicted responses

Run No	Factor 1: Trimethoprim Dose mg/l (A)	Factor 2: pH (B)	Factor 3: Catalyst Dose g/l (C)	%TMP Degradation, Actual	%TMP Degradation, Predicted	%TOC Removal, Actual	%TOC Removal, Predicted
1	25	10	0.4	60.55	61.02	15.37	15.74
2	17.5	7	0.8	80.86	81.58	39.61	41.60
3	10	4	0.4	42.92	43.39	34.17	34.53
4	17.5	7	0.8	77.93	81.58	48.23	41.60
5	17.5	7	0.23	46.28	45.82	40.19	39.83
6	10	10	1.2	54.71	55.19	32.49	32.86
7	17.5	7	0.8	81.74	81.58	41.28	41.60
8	17.5	11.24	0.8	63.57	63.11	39.54	39.19
9	25	4	1.2	66.50	66.97	29.44	29.81
10	17.5	7	0.8	83.79	81.58	40.83	41.60
11	28.11	7	0.8	68.74	68.28	9.91	9.55
12	17.5	2.75	0.8	62.98	62.52	23.53	23.17
13	17.5	7	0.8	82.62	81.58	37.31	41.60
14	17.5	7	1.36	57.12	56.66	36.01	35.65
15	6.89	7	0.8	93.82	93.35	49.11	48.75

The results show that the actual and predicted responses have negligible deviation, which implies that both quadratic models are strong and can accurately predict the responses. The experimental data was fitted into statistical models developed by regression analyses. The models were used to generate the predicted responses shown in Table 4.2. The statistical models are quadratic and are expressed in terms of the coded factors (where A = TMP dose, B = pH, C = catalyst dose) for each response as shown by Eqn 4.1 & 4.2;

% Trimethoprim degradation (Y_1) = +81.58 - 8.87*A + 0.2072*B + 3.83*C – 0.6025*AB – 1.25*AC – 16.22*BC – 0.3823*A^2 – 9.38*B^2 – 15.17*C^2 ..... **Equation 4.1**

%TOC Removal (Y_2) = +41.60 – 13.86*A + 5.66*B – 1.48*C – 4.58*AB + 9.60*AC – 8.40*BC – 6.22*A^2 – 5.21*B^2 – 1.93*C^2 -----….---------- **Equation 4.2**

For both models, all the negative coefficients (A, AB, BC, B^2) indicate unfavorable effects of the parameter on degradation or TOC removal. However, the positive coefficients (B, C) indicate a positive interaction of the parameter on degradation or TOC removal. Similarly, parameters closer to zero indicate lesser influence on responses than the larger coefficients (Lin & Mehrvar, 2018).

4.2.2 Analysis of Variance for TMP Responses

Tables 4.3 and 4.4 represent the summary of the sum of squares, the standard error, the F-value and p-values obtained by ANOVA from the data in Table 4.2 for each response.

Table 4.3: Summary of ANOVA Results for Trimethoprim Degradation (Y_1)

Response 1: Trimethoprim Degradation						
Source	Sum of squares	df	Mean Square	F-value	P value	Remark
Model	3057.87	9	339.76	77.14	<0.0001	significant
A-Trimethoprim Dose	314.43	1	314.43	71.39	0.0004	significant
B-PH	0.1717	1	0.1717	0.0390	0.8512	not significant
C-Catalyst Dose	58.78	1	58.78	13.35	0.0147	significant
AB	0.7260	1	0.7260	0.1648	0.7015	not significant
AC	3.15	1	3.15	0.7144	0.4365	not significant
BC	526.17	1	526.17	119.46	0.0001	significant
A^2	1.13	1	1.13	0.2560	0.6344	not significant
B^2	679.20	1	679.20	154.21	<0.0001	significant
C^2	1777.45	1	1777.45	403.10	<0.0001	significant
Lack of Fit	2.37	5	2.37	0.4835	0.5251	not significant

Std dev=2.10; Mean= 68.28; CV% = 3.07; R^2=0.99; Adj. R^2= 0.98; Predicted R^2=0.91 Adequate Precision = 29.15;

Table 4.4: Summary of ANOVA Results for Trimethoprim TOC Removal (Y_2)

Response 2: TOC Removal						
Source	Sum of squares	df	Mean Square	F-value	P value	Remark
Model	1634.29	9	181.59	13.30	0.0054	significant
A-Tetracycline Dose	69.17	1	768.32	56.26	0.0007	significant
B-PH	121.26	1	128.21	9.39	0.0280	significant
C-Catalyst Dose	87.45	1	8.74	0.6397	0.4601	not significant
AB	20.44	1	41.88	3.07	0.1403	not significant
AC	890.90	1	184.25	13.49	0.0144	significant
BC	31.54	1	141.08	10.33	0.0236	significant
A^2	56.39	1	298.91	21.89	0.0054	significant
B^2	101.05	1	209.44	15.34	0.0112	significant
C^2	532.02	1	28.76	2.11	0.2064	not significant
Lack of Fit	41.48	5	1.42	0.0851	0.7850	not significant

Std dev=3.70; Mean= 34.47; CV% = 10.72; R^2 = 0.96; Adj. R^2 = 0.89; Predicted R^2 = 0.85 Adequate Precision = 12.99;

Each factor coefficient in both models was tested for significance using the Fisher value (F-value) and the probability value (p-value). In statistical terms, if a model has a large F-value > 1 and p-value < 0.05 indicates that the model is significant. However, when a model has a small F-value, and the p > 0.05 indicates non-significance. Therefore, both models had large F-values at 77.14 and 13.30 for Y_1 and Y_2, respectively. Similarly, the p-values for the models were significantly less than 0.05, which implied

the strong significance of the models. On the other hand, the lack of fit for both models was not significant since $p > 0.05$. This suggested that the proposed models were significant and could well fit the observed data (Lin & Mehrvar, 2018; Yin et al., 2021).

The coefficient of determination (R^2) for models Y_1 and Y_2 is 0.99 and 0.96, respectively. This revealed that the models explained 99% and 96% of the variability in response surface. Model Y_1 shows a high degree of correlation between predicted and observed values since the predicted $R^2 = 0.91$, which differs slightly from the Adj. $R^2 = 0.98$ since the difference is below 0.2. Similarly, for model Y_2, the predicted $R^2 = 0.85$ and Adj. $R^2 = 0.89$ are in reasonable agreement. Hence both models give a good prediction of trimethoprim degradation and TOC removal.

During variance analysis, evaluation of the normality of a dataset is crucial since it gives validity of the assumptions made. The residuals should remain independent as well as have a normal distribution along the line of best fit with a constant variance, which proves the adequacy of the chosen model (Attarikhasraghi et al., 2021). Figure 4.10 (a, b) shows the normal probability plot.

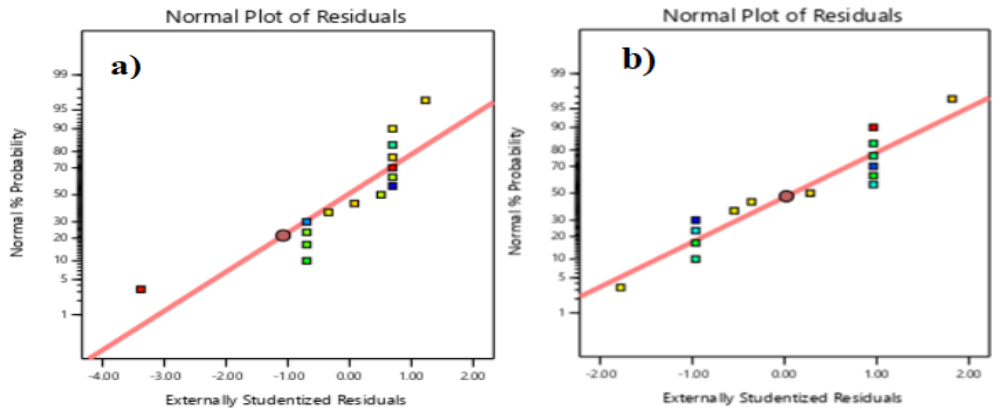

Figure 4.10: Normal probability plot of residuals: (a) %Degradation (b) %TOC removal

It is evident that most datapoints are scattered along the line of best fit with some minor deviations. The linear scatter of residuals implies a homogenous distribution of error,

and the effect of random error due to experimental sequence is decreased (Zare & Zeinabad, 2022). The plot of predicted vs actual values is shown in Figure 4.11 (a, b).

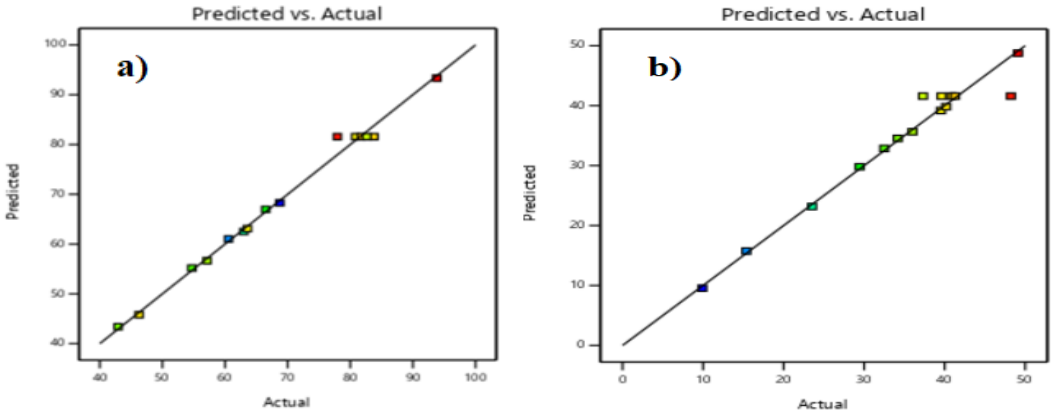

Figure 4.11: Plot of predicted versus actual values (a) %Degradation (b) %TOC removal

The results show a linear relationship exists between experimental and predicted values, with most of the data points laying along the straight line. This confirms the accuracy of the two models and also signifies minimal experimental error.

4.2.3 Effects of Factor Interaction and Response Surface Plots for TMP Degradation

Figure 4.12 (a, b) shows the interaction of TMP dose (A) and pH (B) in influencing degradation.

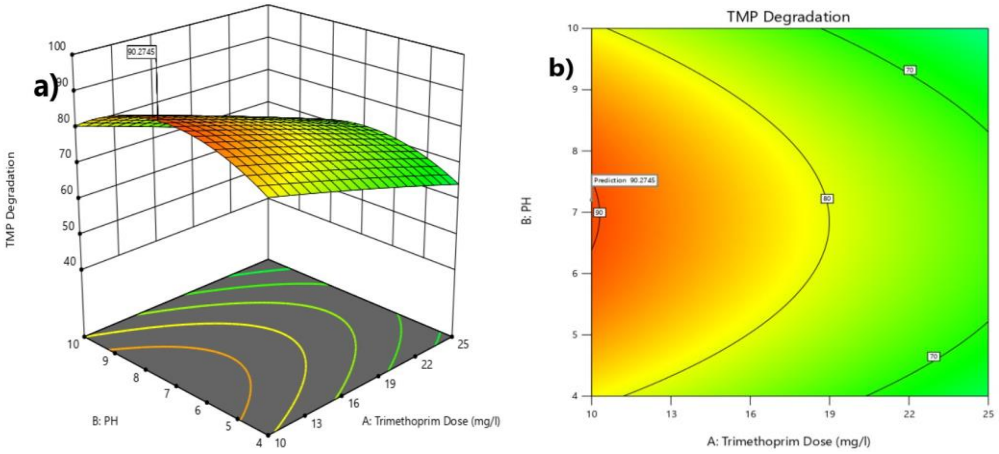

Figure 4.12: (a) Response surface plot for TMP dose and pH, (b) Contour plot for TMP dose and pH

The disc appearance of the contour lines is an indicator of the low significance of parameter AB in affecting degradation (Berkani et al., 2021; Zhang & Wang, 2018). Similarly, it is evident that a narrow pH range (pH 5.5-7.2) at low pollutant dose yields the highest degradation (>90%). However, a further increase or decrease in pH beyond the optimum range is accompanied by a rapid reduction in degradation. The high degradation observed within the narrow pH range can be due to the effects of pH on the surface charge of the catalyst and the ionization of the pollutant. TMP has a pKa value of approximately 7.1 (Osoikhia & Emesiani, 2019); hence when pH < pKa, it exists as cationic molecules. However, when pH > pKa its dominant molecules have neutral charges (Ljubas et al., 2023). On the other hand, $ZnFe_2O_4$/g-C_3N_4 composites have the points of zero charge (pzc) at pH 5.25-5.91, hence when pH > pH_{pzc}, the photocatalyst surface is negatively charged (Dai et al., 2021; Saeed et al., 2021). The highest degradation was observed at pH 6.5. At such conditions, the photocatalyst and trimethoprim molecules possess opposite charges to each other. This results in the increased attraction and adsorption of TMP molecules on the catalyst surface, hence the increased degradation (Ljubas et al., 2023). However, when pH > pKa, both the catalyst surface and the molecules become negatively charged, leading to strong repulsion between the catalyst and pollutant, hence a decrease in degradation as observed at high pH values.

Figure 4.13 (a, b) shows the interaction between pH (B) and catalyst dose (C).

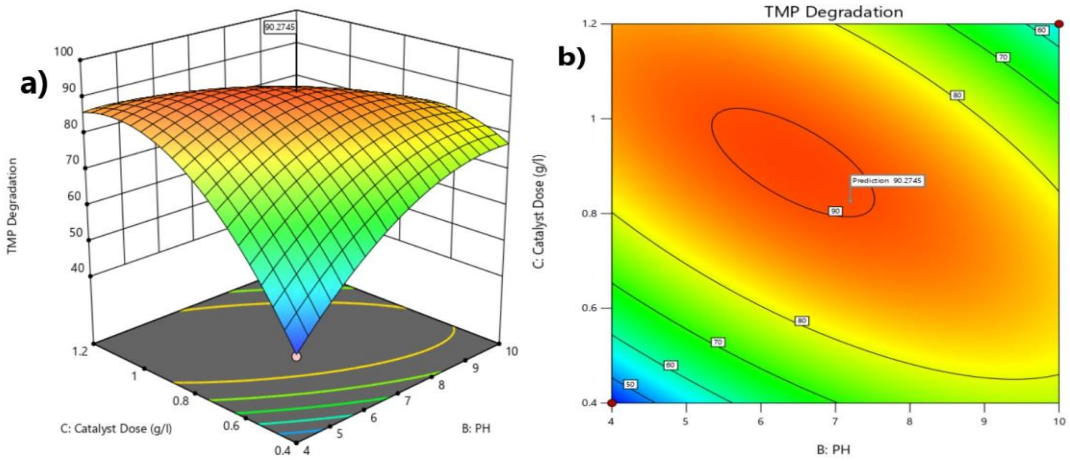

Figure 4.13: (a) Response surface plot for pH and catalyst dose, (b) Contour plot for pH and catalyst dose

The elliptical-shaped contour lines are evidence of significant interaction between factors BC in affecting degradation, confirmed by p-value (BC) < 0.05. From the RSM graph 4.13 (a), it is evident that an increase in the catalyst dosage results to an increase in degradation until the optimum range is exceeded, which declines steadily. Similarly, according to the Contour graph 4.13 (b), both pH and catalyst dose seem to influence degradation, with the highest degradation > 90% realized at pH 5.5-7.5 and a catalyst dosage of between 0.8-1.0g/l. The decreased degradation at high catalyst loading could be attributed to increased solution turbidity, which hinders light penetration to the catalyst's active surfaces (Samy et al., 2020).

Figure 4.14(a, b) shows the relationship between pollutant dose (A) and catalyst dose (C).

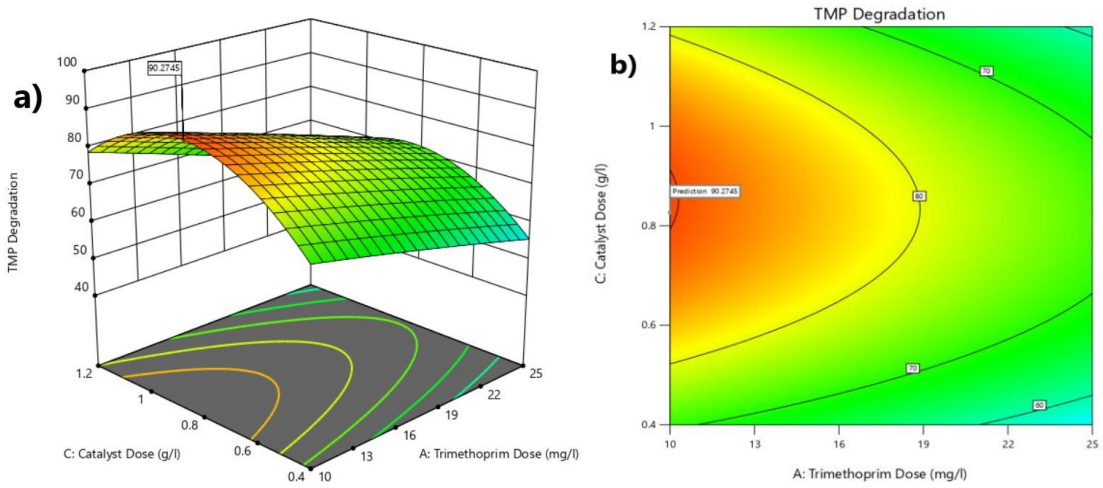

Figure 4.14: (a) Response surface plot for TMP dose and catalyst dose, (b) Contour plot for TMP dose and catalyst dose

The figures show that a decrease in catalyst dosage was accompanied by a decrease in the degradation efficiency. However, an inverse linear relationship existed between TMP dose and the degradation efficiency. Besides, from the contour graph 4.14 (b), it was observed that the highest degradation > 90% was obtained for a catalyst dosage of approximately 0.8-1.0g/l and a pollutant concentration of 10mg/l. The decrease in degradation at low catalyst dose is due to a decrease in number of surface-active sites available for degradation. On the other hand, high pollutant doses could have saturated the catalyst active sites, leading to decreased generation of radicals (Zare & Zeinabad, 2022).

4.2.4 Effects of Factor Interaction and Response Surface Plots for TMP %TOC Removal

Figure 4.15 (a, b) shows the interaction between trimethoprim dose (A) and pH (B) in influencing TOC removal.

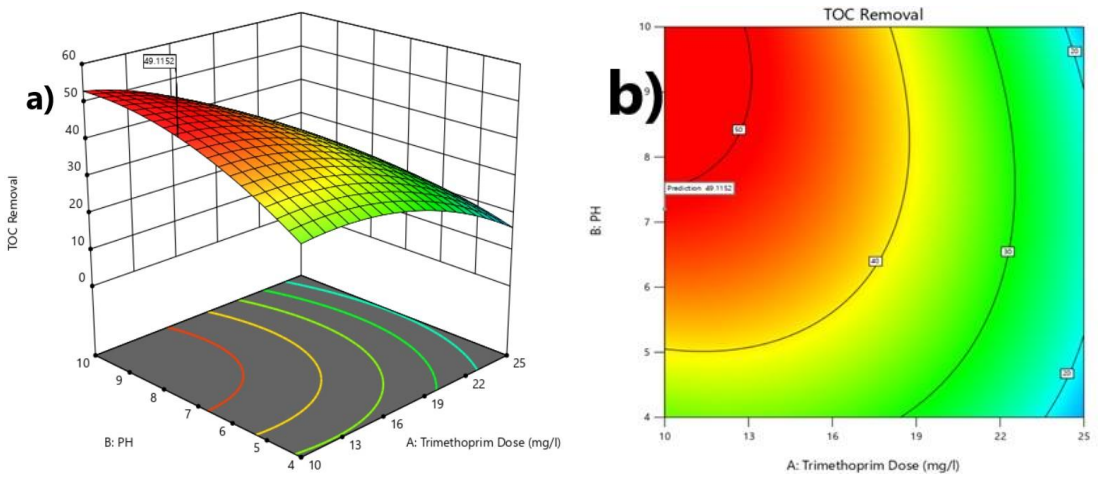

Figure 4.15: (a) Response surface plot for TMP dose and pH, (b) Contour plot for TMP dose and pH

The disc-shaped contour lines are an indicator of low interaction between the factors, which is confirmed by the p-value of AB (0.1403) > 0.05 as shown in Table 4.4 (Hosseini et al., 2022). From the RSM graph, an increase in trimethoprim dose is accompanied by a gradual decrease in TOC removal. On the other hand, as pH increased from 4 to 10, it resulted in an increase in the TOC removal. Besides, the Contour graph 4.15 (b) shows that the highest TOC removal efficiency (> 50%) occurred when the pollutant dose was 10-14mg/l and a pH of 6.5-10. The influence of pH in TOC removal is prominent since it affects the protonation/deprotonation of the organic states as well as the ionization state of the photocatalyst. Therefore, the high TOC removal observed with increasing pH can be possibly explained by two scenarios. At alkaline environment the hydroxyl ion concentration is elevated which promotes the hydroxylation process. Hydroxylation is a major mineralization pathway for trimethoprim, hence more intermediate molecules are mineralized at these conditions (Samy et al., 2020). The second explanation could be due to enhanced oxidization of hydroxyl ions to hydroxyl radicals on the surface of the catalyst which consequently improves the TOC removal (Hosseini et al., 2022).

Figure 4.16 (a, b) shows the interaction of pH (B) and catalyst dose (C) in influencing TOC removal.

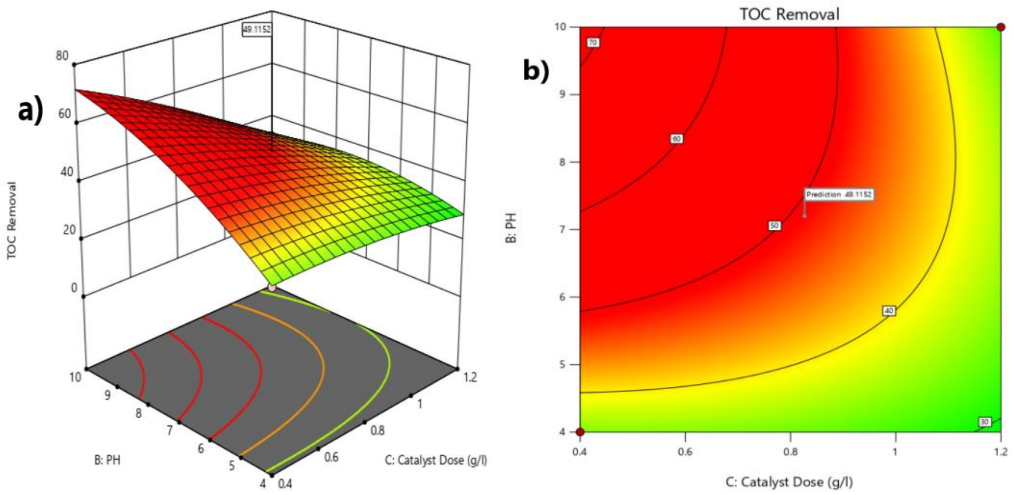

Figure 4.16: (a) Response surface plot for pH and catalyst dose, (b) Contour plot for pH and catalyst dose

The elliptical-like contour lines show significant interaction between the factors, as confirmed by the p-value of BC (0.0236) < 0.05 shown in Table 4.4. The RSM graphs show that an almost linear relationship exists between change of pH and TOC removal. Since an increase in pH from 4 to 10 is accompanied by an increase in TOC removal. On the other hand, it is observed from the contour lines that both pH and catalyst dose have a synergistic influence on TOC removal since the highest TOC removal (> 60%) occurs at pH range 7.5-10 and catalyst dose 0.4-0.6g/l. Low catalyst dose tend to have highest TOC removal due to the antagonistic influence of the organic dye-sensitizer.

Figure 4.17(a, b) shows the interaction between trimethoprim dose (A) and catalyst dose (C) on the influence on TOC removal.

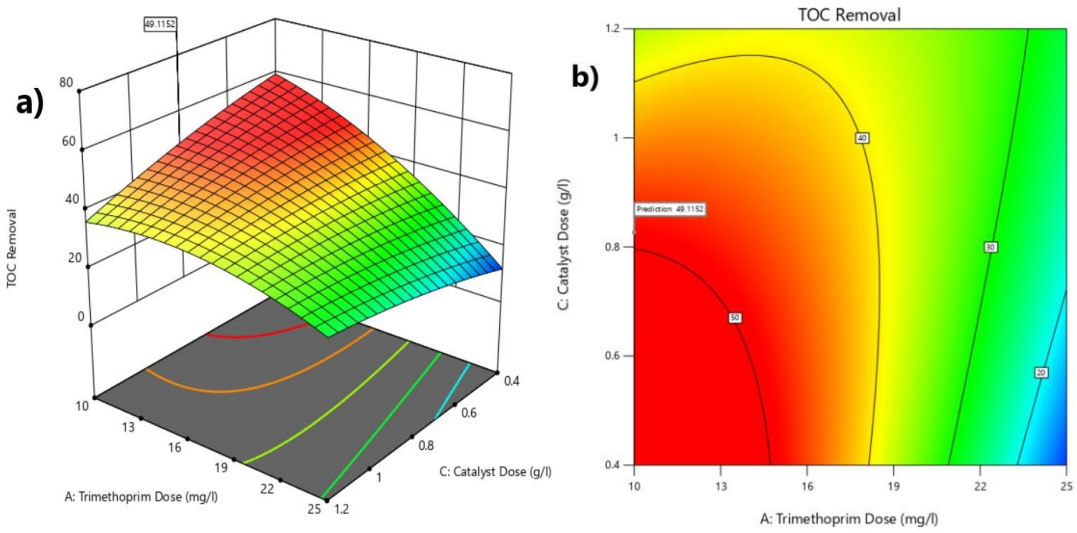

Figure 4.17: (a) Response surface plot for TMP dose and catalyst dose, (b) Contour plot for TMP dose and catalyst dose

The elliptical-like contour lines suggest a significant level of interaction between the factors, which is confirmed by the p-value of AC (0.0144) < 0.05, as shown in Table 4.4. According to the RSM graph, an increase in trimethoprim dose results to a decrease in TOC removal. Similarly, an increase in the catalyst dose is accompanied by a decrease in TOC removal. Nonetheless, it can be observed from the contour graph that the highest TOC removal (>50%) occurs at a catalyst dose in the range of 0.4-0.7g/l and pollutant dose range of 10-13.2mg/l.

4.2.5 Optimization of Trimethoprim Degradation and TOC Removal

The desirability function was used in obtaining the global optimum for the combined responses and the localized optimum for single responses as shown in Figure 4.18.

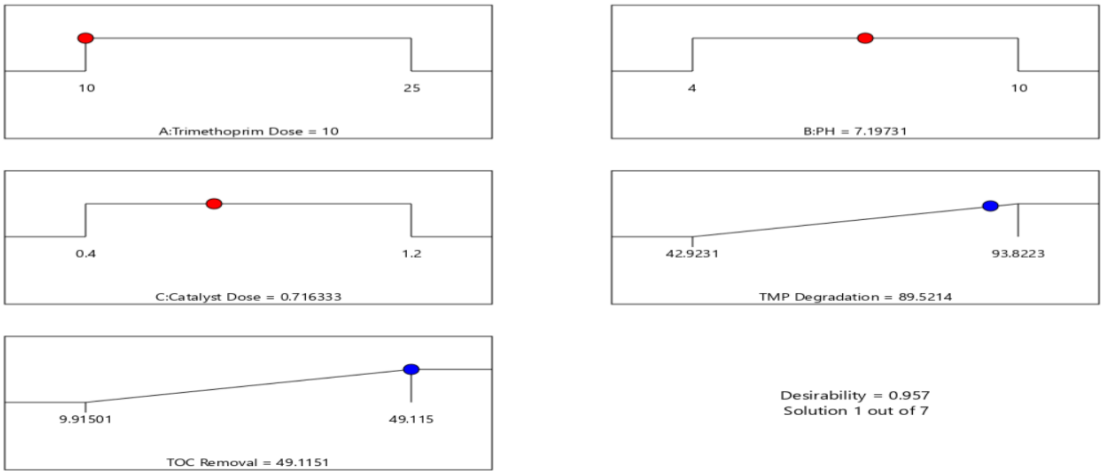

Figure 4.18: Global optimum parameters after optimization of Degradation and TOC Removal

The overall optimum degradation parameters for the two responses were: trimethoprim dose = 10mg/l, pH = 7.2, catalyst dose = 0.716g/l which predicted a yield of 89.52% degradation and 49.11% TOC removal at a desirability of 95.70%.

4.2.6 Effects of Factors on TMP Removal

Single factors studies were performed at various pH ranges (pH 5.5-10), catalyst loading (0.5-2.5g/l) and pollutant dose (10-40mg/l) to help validate the results obtained from RSM. The factor under study was varied, while the other factors were kept constant at their localized optimum.

4.2.6.1 Effect of operating pH

The effect of solution pH affects the surface charge property of the catalyst as well as the ionization state of the pollutant (Trang et al., 2021). The effect of pH was evaluated at pH 5.5-10, at the fixed conditions of; TMP dose = 10mg/l, catalyst dose = 0.7g/l and 90 minutes irradiation time. From Figure 4.19, the removal efficiency by adsorption for the first 15 minutes were 8%, 9.61%, 25.09% and 35.77% for pH 5.5, pH 10, pH 6.43 and pH 7, respectively.

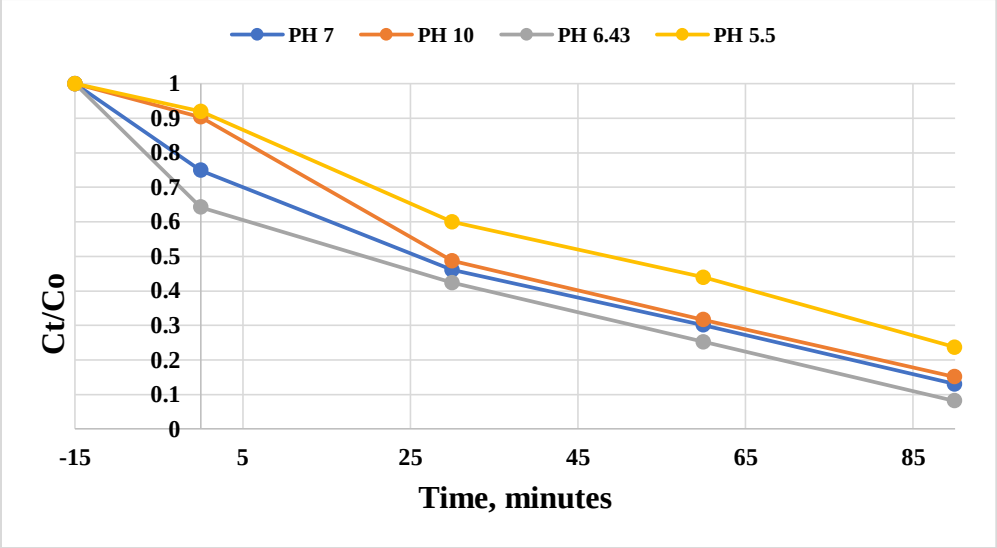

Figure 4.19: Plot of TMP degradation with time at various pH values

The highest degradation was 91.83% observed at pH 6.43, similar to the predicted optimum pH by the RSM optimization. At pH 6.43, the photocatalyst is negatively charged since $pH_{solution} > pH_{pzc}$. However, the TMP molecules are positively charged since the pKa value is 7.1 and when $pH_{solution} <$ pKa, TMP exists as cations (Ljubas et al., 2023). Therefore, the TMP molecules are strongly adsorbed on the catalyst surface resulting in higher degradation. The lowest degradation efficiency of 76.34% was achieved at pH 5.5. In such conditions, both the catalyst and pollutant molecules are positively charged hence repel each other strongly. Therefore, less pollutant molecules are adsorbed on the catalyst surface leading to poor degradation (Deng et al., 2018).

The highest TOC removal efficiency was realized at high pH conditions as shown in Figure 4.20.

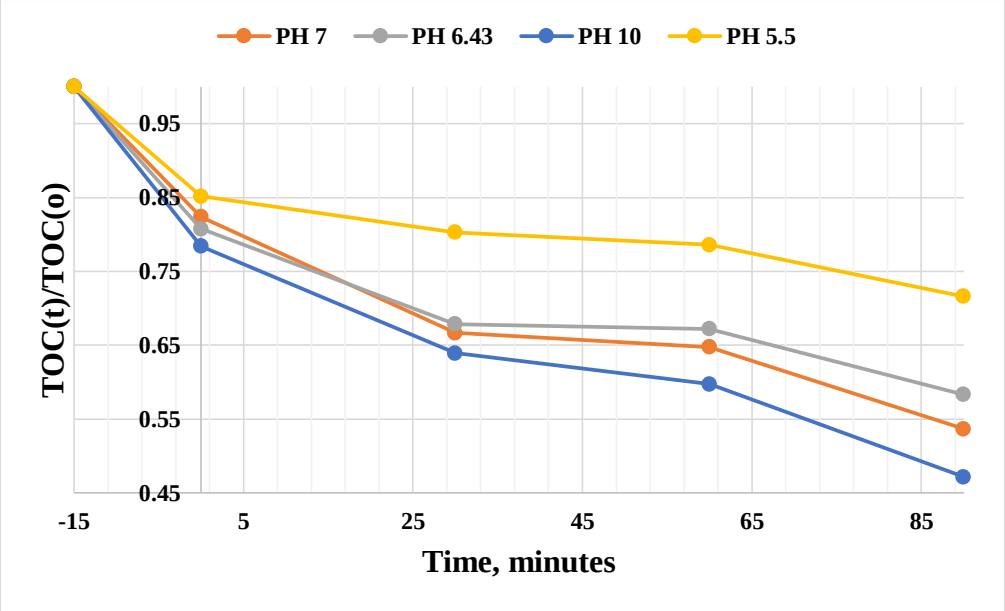

Figure 4.20: Plot of TMP %TOC Removal with time at various pH values

The order of TOC removal for TMP was pH 10 > pH 7 > pH 6.43 > pH 5.5 with removal efficiencies of 52.83%, 46.33%, 41.64%, and 28.39%, respectively. The highest removal observed at pH 10 could be attributed to the slightly alkaline environment, which has excess of hydroxyl ions which were rapidly converted to hydroxyl radicals (Pham et al., 2021). This is necessary for the fast mineralization of both the pollutants and its intermediate groups. This is supported by previous studies that have reported pollutant molecules decomposition in strong alkaline environments (Zhou et al., 2022).

4.2.6.2 Effect of Catalyst Dose

The effect of catalyst concentration in TMP degradation was studied in the range of 0.5-2.5g/l at fixed conditions of 10mg/l pollutant dose, pH 7 and 90minutes irradiation time. From Figure 4.21, the removal efficiencies by adsorption for the first 15minutes carried out in the dark were; 22.92%, 24.33%, 27.565% and 29.52% for 0.5g/l, 0.7g/l, 1.2g/l and 2.5g/l, respectively.

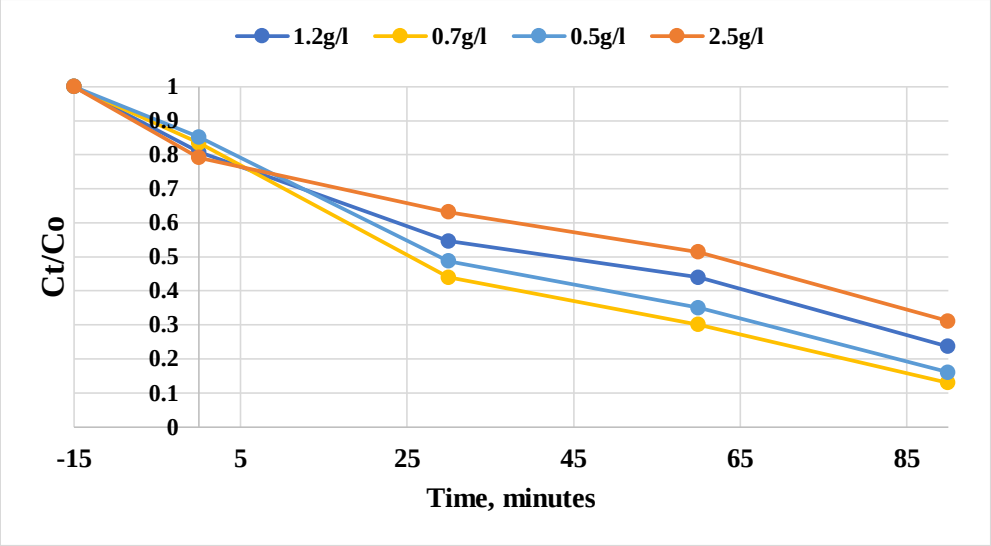

Figure 4.21: Plot of TMP degradation with time at various catalyst doses

The initial increase in TMP removal at high catalyst loading is due to improved pollutant adsorption on a large surface area of catalyst active sites (Le et al., 2019). After 90minutes irradiation, the removal efficiencies were 68.87%, 76.34%, 84% and 87.02% for 2.5g/l, 1.2g/l, 0.5g/l and 0.7g/l respectively. The decreased TMP degradation at high catalyst loading above optimum point is due to increase in the solution turbidity which scatters light photons hence inhibiting radical generation (Minh et al., 2019). Furthermore, at high catalyst loading some studies have reported the increase in particle agglomeration, decreasing the available active sites (Samy et al., 2020).

From Figure 4.22, the TOC removal rates decreased with increasing catalyst dose from 48.64% to 21.88% for 0.5g/l and 2.5g/l catalyst, respectively.

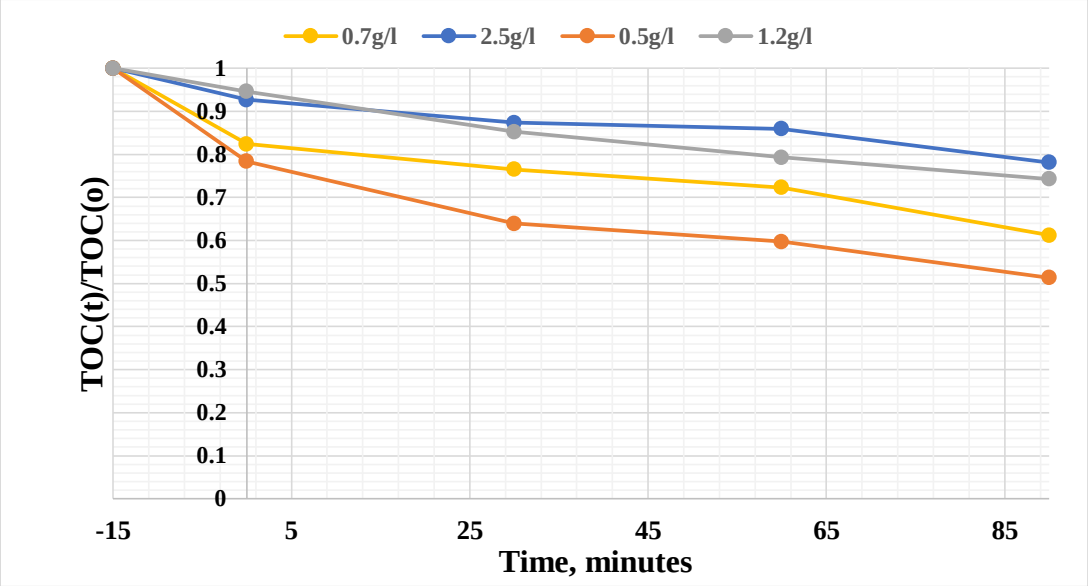

Figure 4.22: Plot of TMP %TOC Removal with time at various catalyst doses

The high TOC removal at high catalyst dosage could be due to the antagonistic effect of the organic dye sensitizer which might slightly have increased the level of organic carbon in the solution.

4.2.6.3 Effect of Initial Pollutant Concentration

The effect of TMP dose (10-40mg/l) was studied at the fixed conditions of pH 7, catalyst dose 0.7g/l and irradiation time of 90minutes. From Figure 4.23, the degradation efficiency decreased with increasing pollutant concentration from 87.02 to 57.88% for 10 and 40mg/l.

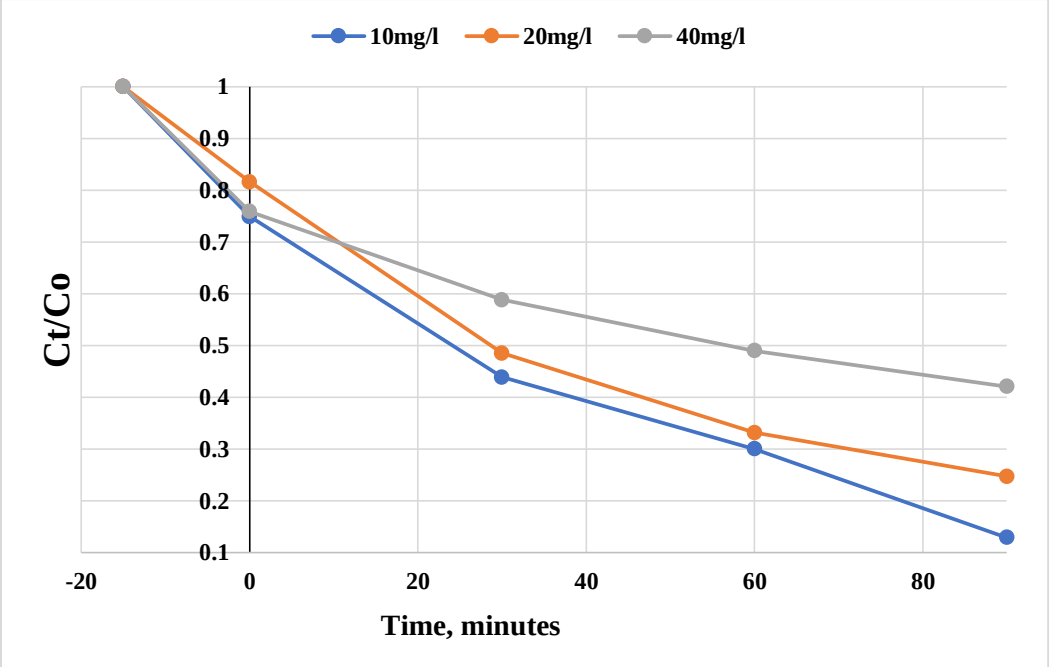

Figure 4.23: Plot of TMP degradation with time at various pollutant dosage

This could be possibly due to low pollutant concentration; most catalyst active sites are unoccupied and thus available for pollutant removal. However, at high pollutant concentration, all the active sites become saturated with the contaminant molecules which inhibits reactive radical species generation. Furthermore, at high pollutant doses intermediate products produced during photocatalysis will also increase competition with the pollutant for active sites hence a remarkable decrease in degradation efficiency (Minh et al., 2019).

The percentage TOC removal for 10mg/l, 20mg/l and 40mg/l TMP doses were 46.33%, 27.99% and 13.90% respectively, as shown in Figure 4.24.

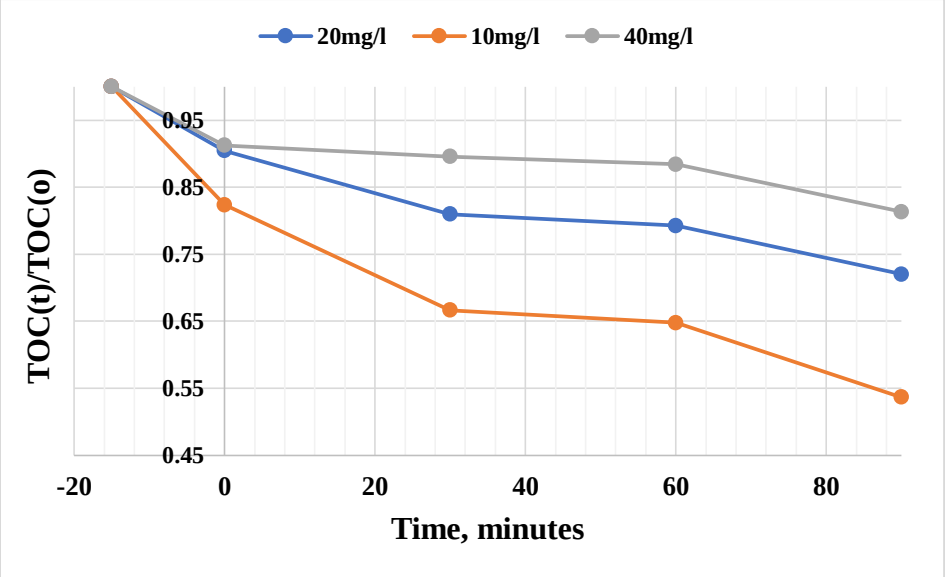

Figure 4.24: Plot of TMP %TOC Removal with time at various catalyst doses

The decrease in % TOC removal with increasing pollutant dose could be attributed to the saturation of active sites with the pollutants.

4.2.7 Possible Degradation Pathways for Trimethoprim

The main mechanisms for the degradation of trimethoprim are; hydroxylation, cleavage and oxidation (Hasija et al., 2022; Samy et al., 2020). Trimethoprim has a mass to charge ratio of 291. During hydroxylation reactions hydroxyl ions react with TMP to form hydroxylated products with a general formula $C_{14}H_{19}N_4O_{3+x}$. The hydroxylated products can be (mono, bi, tetra, penta) depending on the value of x. The hydroxylated products are formed by addition reactions of TMP and hydroxyl ions. Therefore, the hydroxylated intermediates are formed in the order: mono-hydroxylated ($C_{14}H_{19}N_4O_4$; m/z 307), di-hydroxylated ($C_{14}H_{19}N_4O_5$; m/z 323), tetra-hydroxylated ($C_{14}H_{19}N_4O_6$; m/z 339) and penta-hydroxylated ($C_{14}H_{19}N_4O_8$; m/z 371). Demethylation reactions generate intermediate products with a formulae $C_{14-y}H_{19-2y}N_4O_{3+x}$ ($C_{13}H_{17}N_4O_3$; m/z 309, $C_{12}H_{15}N_4O_5$, m/z 279). Finally, cleavage reactions are responsible for breaking the unstable intermediates into smaller products ($C_5H_6N_4O$, m/z 139; $C_5H_6N_4O_2$, m/z 155 and $C_8H_{10}O_4$, m/z 141) (Samy et al., 2020).

A study by Ljubas et al. on the degradation pathway of TMP using immobilized TiO2 and simulated solar light identified five degradation products. The transformational products chromatogram peaks were identified by LC-Ms based on their retention time and m/z values. The peaks were: DP-1 (m/z 307), DP-2 (m/z 305), DP-3 (m/z 277), DP-4 (m/z 155) and DP-5 (m/z 139). These intermediates matched with those identified by Samy and co-workers. Therefore, a possible degradation pathway would have been hydroxylation of TMP to yield (DP-1 = $C_{14}H_{19}N_4O_4$; m/z 307), demethylation reaction to yield (DP-2 and DP-3) and cleavage reactions to yield (DP-4 and DP-5) (Ljubas et al., 2023).

4.3 Optimization of Variables for Degradation of Synthetic Water Containing Tetracycline

4.3.1 Model Fitting and Statistical analysis for Tetracycline

Table 4.5 shows the three-factor CCD matrix table generated by Design expert software. The experimental values and the corresponding predicted values are shown for degradation and TOC removal as the responses.

Table 4.5: CCD matrix of operating variables with their actual and predicted responses

Run No	Factor 1: Tetracycline Dose mg/l (A)	Factor 2: pH (B)	Factor 3: Catalyst Dose g/l (C)	% Tetracycline Degradation, Actual	% Tetracycline Degradation, Predicted	% TOC Removal, Actual	% TOC Removal, Predicted
1	17.5	7	0.8	91.61	92.67	49.59	51.21
2	10	4	0.8	89.56	89.87	57.52	59.47
3	10	4	0.4	72.54	71.94	62.83	63.52
4	17.5	12.05	0.8	64.43	65.62	55.25	53.80
5	10	10	0.4	76.54	75.79	61.36	64.84
6	17.5	7	0.8	93.42	92.67	52.82	51.21
7	25	4	1.2	85.32	85.71	57.11	55.24
8	17.5	7	0.8	94.21	92.67	50.57	51.21
9	17.5	7	0.8	88.11	92.67	51.75	51.21
10	25	10	1.2	74.67	74.92	41.30	42.22
11	17.5	1.95	0.8	72.13	71.44	64.41	63.60
12	17.5	7	0.8	94.14	92.67	52.62	51.21
13	10	10	1.2	92.54	91.42	53.14	52.84
14	17.5	7	1.47	89.68	89.61	44.83	45.20
15	30.11	7	0.8	88.56	87.95	21.07	21.49
16	4.88	7	0.8	96.07	97.18	82.41	79.70
17	25	4	0.4	76.61	77.39	15.19	17.09
18	25	10	0.4	69.56	68.90	12.36	12.01
19	17.5	7	0.13	68.56	69.11	25.34	22.76
20	17.5	7	0.8	94.62	92.67	49.56	51.21

The results showed negligible deviations between the observed and predicted values, which was evidence for a robust quadratic model that can predict responses. Regression analyses generated the quadratic models used in fitting the experimental data. The regression equation is expressed in terms of coded factors (where A = TMP dose, B = pH, C = catalyst dose) for each response as shown by Eqn 4.3 & 4.4;

% Tetracycline degradation (Y_3) = +94.05 -5.17*A - 2.31*B - 5.01*C – 3.08*AB – 3.63*AC -0.8672*BC – 0.0380*A^2 – 8.54*B^2 – 10.60*C^2 ……**Equation 4.3**

%TOC Removal (Y_4) = +51.77 – 3.71*A – 4.91*B – 8.32*C – 1.60*AB + 15.93*AC – 3.00*BC – 1.98*A^2 + 2.65*B^2 – 13.72*C^2 …… **Equation 4.4**

The positive values (AC, B^2) in the regression model represent synergistic effects on the responses, while the negative values (A, B, C, AB, AC, BC) are due to antagonistic effects (Rani & Karthikeyan, 2018).

4.3.2 Analysis of Variance (ANOVA)

Tables 4.6 and 4.7 represent the summary of the sum of squares, the standard error, the F-value and p-values obtained by ANOVA from the data in Table 8 for each response.

Table 4.6: Summary of ANOVA Results for Tetracycline Degradation (Y_3)

Response 1: Tetracycline Degradation						
Source	Sum of squares	df	Mean Square	F-value	P value	Remark
Model	2046.46	9	227.38	59.59	<0.0001	significant
A-Tetracycline Dose	134.16	1	134.16	35.16	0.0001	significant
B-PH	26.80	1	26.80	7.02	0.0243	significant
C-Catalyst Dose	31.75	1	31.75	8.32	0.0163	significant
AB	76.14	1	76.14	19.95	0.0012	significant
AC	46.19	1	46.19	12.10	0.0059	significant
BC	2.64	1	2.64	0.6920	0.4249	not significant
A^2	0.0208	1	0.0208	0.0055	0.9425	not significant
B^2	1049.49	1	1049.49	275.03	<0.0001	significant
C^2	317.51	1	317.51	83.21	<0.0001	significant
Lack of Fit	7.35	5	1.47	0.2384	0.9292	not significant

Std dev=1.95; Mean= 83.64; CV% = 2.34; R^2=0.9817; Adj. R^2= 0.9652; Predicted R^2=0.9514 Adequate Precision = 22.8513; Residuals =38.16

Table 4.7: Summary of ANOVA Results for Tetracycline TOC Removal (Y_4)

Response 1: TOC Removal						
Source	Sum of squares	df	Mean Square	F-value	P value	Remark
Model	5170.42	9	574.49	110.26	<0.0001	significant
A-Tetracycline Dose	69.17	1	69.17	13.28	0.0045	significant
B-PH	121.26	1	121.26	23.27	0.0007	significant
C-Catalyst Dose	87.45	1	87.45	16.78	0.0022	significant
AB	20.44	1	20.44	3.92	0.0758	not significant
AC	890.90	1	890.90	170.99	<0.0001	significant
BC	31.54	1	31.54	6.05	0.0336	significant
A^2	56.39	1	56.39	10.82	0.0082	significant
B^2	101.05	1	101.05	19.40	0.0013	significant
C^2	532.02	1	532.02	102.11	<0.0001	significant
Lack of Fit	41.48	5	8.30	3.91	0.0805	not significant

Std dev=2.28; Mean= 47.55; CV% = 4.8; R^2=0.99; Adj. R^2= 0.9810; Predicted R^2=0.9330 Adequate Precision = 35.7627; Residuals =52.10

Both regression models Y_3 and Y_4 had large F-Value (Y_3=59.59, F-value Y_4=110.26) and small p-values ($Y_3 < 0.0001$, $Y_4 < 0.0001$). This indicated the strong significance of the models. Similarly, the relevance of the factors in the models is summarized in

Tables 4.6 and 4.7. Tetracycline dose and pH were the most significant factors in degradation and TOC removal, respectively. On the contrary, the lack of fit for both models were not significant since p-value > 0.05. This indicated that the proposed models had better predictability of responses (Zhang & Wang, 2018).

The normal probability plot is a graphical method for determining whether the standard deviation of predicted and observed values follow the normal distribution (Berkani et al., 2021). Figure 4.25 (a, b) shows the normal probability plot.

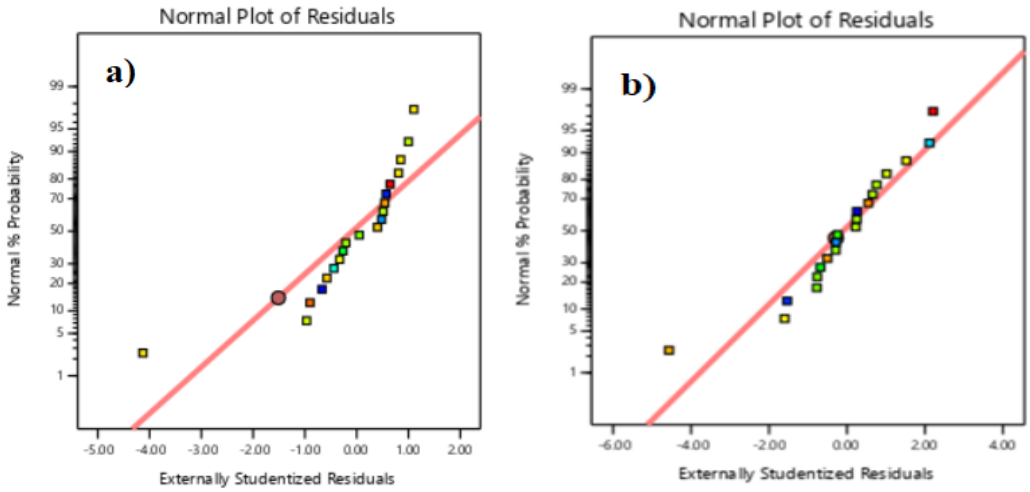

Figure 4.25: Normal probability plot of residuals: (a) %Degradation (b) %TOC removal

It is evident that the sum of errors follows a normal distribution and lie close to the straight line which proves the assumptions used. Besides, the errors appear to be randomly scattered which reinforces the adequacy of the model. This confirmed that both models were sufficient since they had minimal residual errors (Musa & Gaya, 2019).

The R^2 is an important tool for estimating the correlation between observed and predicted values. Figure 4.26 (a, b) shows the plot of predicted versus the experimental values.

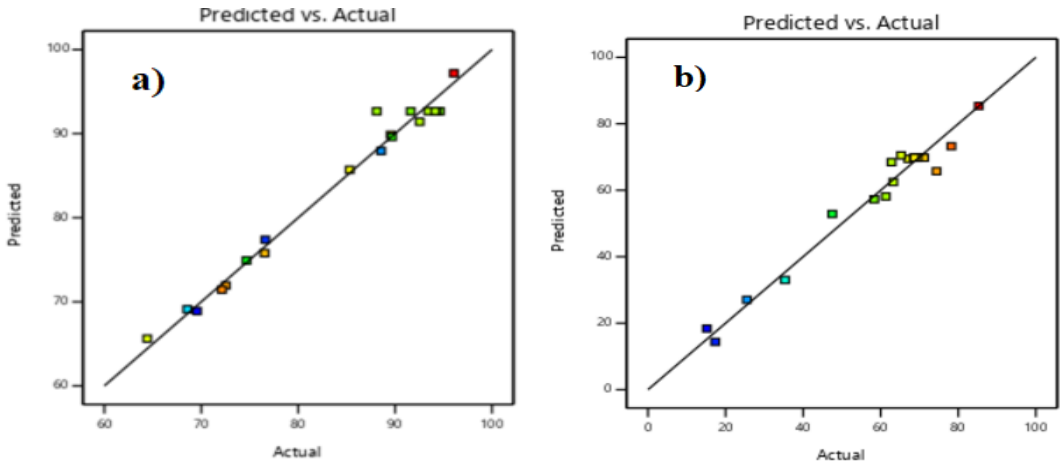

Figure 4.26: Plot of predicted versus actual values, (a) %Degradation (b) %TOC removal

The R^2 for Y_3 and Y_4 was 0.98 and 0.99, respectively. This indicated that 98 and 99% of the variation in the response surface for Y_3 and Y_4 could be explained by the independent variables (Shan et al., 2022). Similarly, the adjusted R^2 is a corrected-goodness of fit with values R_{adj}^2 = 0.97, 0.98, which matches the R^2 values for the models. This shows that the regression equation can accurately predict the experimental datapoints (Berkani et al., 2021). Nonetheless, the predicted R^2 value for Y_3 and Y_4 was R_{pred}^2 = 0.95, 0.93 was still close to the R^2 and adjusted R^2. This revealed the high level of correlation for the generated model in predicting the responses within the data range (Favier et al., 2023).

The adequate precision values for Y_3 and Y_4 are 22.85 and 35.76, respectively. Higher precision values greater than 4 indicate the adequacy of the model in exploring the design space (Garg et al., 2020; Rani & Karthikeyan, 2018). Additionally, the two models were reliable and could be used in predicting degradation and TOC removal for tetracycline. The standard deviation was calculated from the six replicates of the center points for both Y_3 and Y_4 which yielded 1.95 and 2.28, respectively. These values are evidence of good repeatability of the experiments and the variation in responses is due to the change in factors and not in environmental conditions (Mountassir et al., 2022).

4.3.3 Effects of Factor Interaction and Response Surface Plots for Tetracycline Degradation

Figure 4.27(a, b) shows the interaction of tetracycline dose (A) and pH (B) in determining degradation.

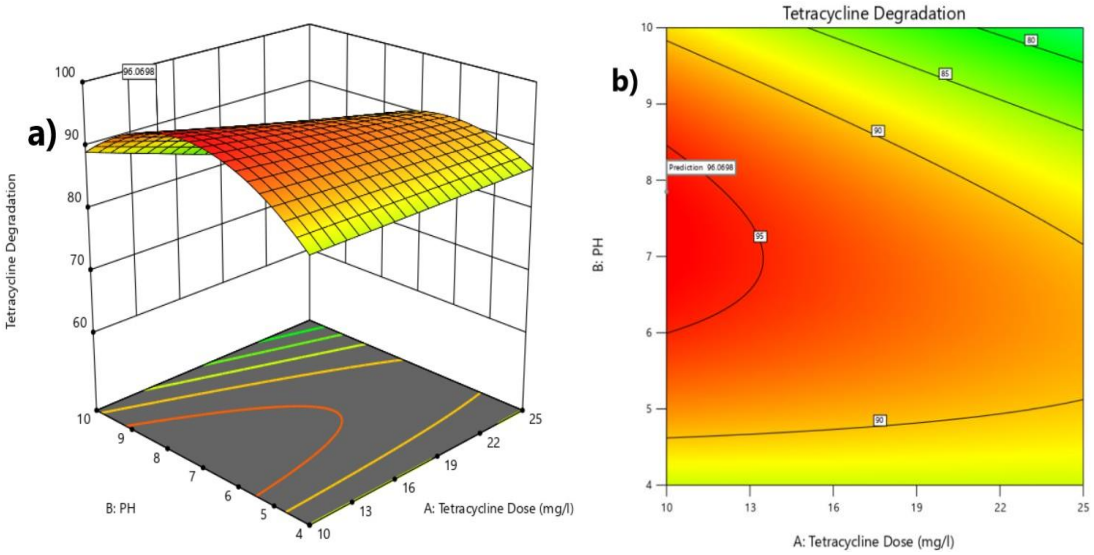

Figure 4.27: (a) Response surface plot for Tetracycline dose and pH, (ab) Contour plot for Tetracycline dose and pH

The elliptical contours are an indicator of the high significance of parameter AB in affecting degradation. The RSM graph 4.27 (a) shows that degradation efficiency increased with a decrease in pollutant concentration from 25 to 10mg/l. The highest degradation (> 95%) occurred at low pollutant dose and wide pH range (4 - 9). The high photocatalytic activity observed at a wide pH range could be due to the amphoteric nature of tetracycline. Tetracycline has three pKa values (pKa_1 =3.3, pKa_2 =7.7, pKa_3=9) (Zhou et al., 2022). Therefore, tetracycline molecule is cationic below pH 3.3, neutral between pH 3.3 -7.7 and anionic above pH 7.7. Consequently, the dissociated tetracycline molecules have a high degradation across a wide pH range. Furthermore, a study by (Adenuga et al., 2021), on the degradation of tetracycline using $AgCl/Bi_24O_{31}Cl_{10}$ at pH 3, 7 and 11 found degradation ranging between 85-87%. These results suggested that tetracycline degradation maybe independent of pH due to its

amphoteric nature, dissociation characteristics and is significantly degraded at wide pH ranges (Adenuga et al., 2021). However, further increase above pH 10 lead to reported decrease in degradation efficiency, since the dissociated tetracycline ions were repelled by the negative charges on catalyst surface.

Figure 4.28(a, b) shows the interaction between pH (B) and catalyst dose (C).

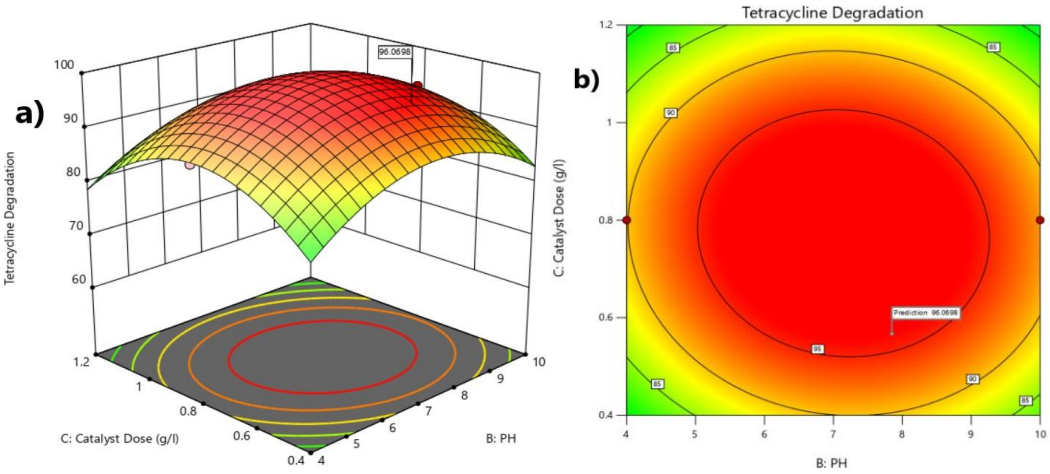

Figure 4.28: (a) Response surface plot for pH and catalyst dose, (bb) Contour plot for pH and catalyst dose

The disc-shaped contour lines indicate low levels of interaction between the factors, confirmed by p-value of (BC) > 0.4249. From the RSM graph 4.28 (a), an increase in catalyst dose from 0.4-0.8g/l resulted to an increase in tetracycline degradation but when the optimum was exceeded degradation declined. The enhanced degradation could be attributed to increased surface area of active sites at large catalyst doses which consequently increased radicals concentration (Adenuga et al., 2021; Hanif et al., 2021). However, further increase in catalyst dosage or pH beyond the optimum values may have disturbed the catalyst-pH balance leading to a decrease in degradation efficiency. Besides, excessive interactions between excited and un-excited catalyst molecules at high catalyst loading decreased degradation (Ur et al., 2021).

Figure 4.29(a, b) shows the interaction between pollutant dose (A) and catalyst dose (C).

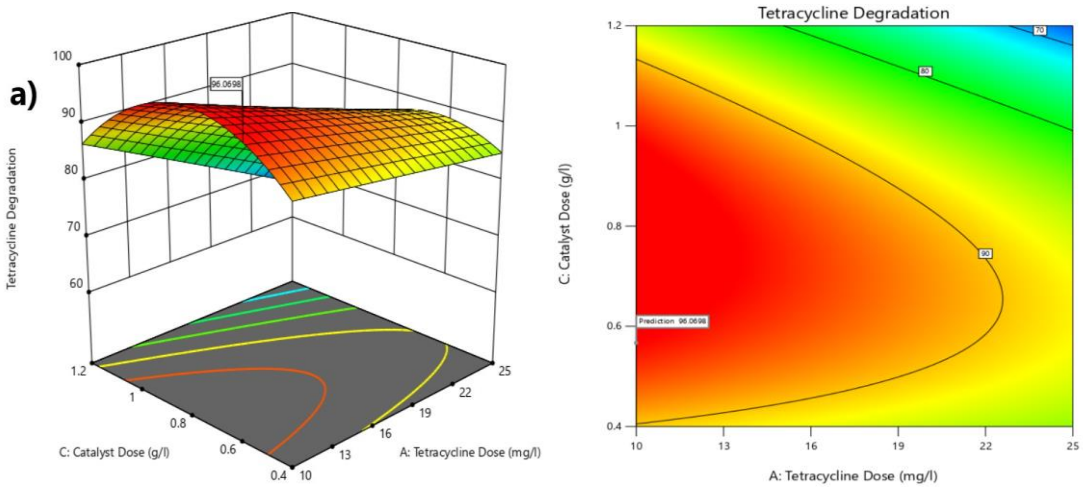

Figure 4.29: (a) Response surface plot for Tetracycline dose and catalyst dose, (b) Contour plot for Tetracycline dose and catalyst dose

The contour graph shows that the highest tetracycline degradation (> 95%) was obtained when the catalyst dose was 0.5-1.0g/l and a pollutant dose of 10mg/l. Similarly, the RSM graph shows that when the catalyst dose was decreased below the optimum was accompanied by a decrease in degradation. This was possibly due to a reduction in surface-active sites in the solution at lower catalyst loading (Song et al., 2016). On the other hand, when the pollutant dose was increased above the optimum the degradation efficiency decreased. This could be attributed to excessive competition for reaction sites by the pollutant which inhibited reactive species generation (Doosti et al., 2022).

4.3.4 Effects of Factor Interaction and Response Surface Plots for Tetracycline and %TOC Removal

Figure 4.30(a, b) shows the response surface plots for pollutant dose (A) and pH (B) in TOC removal.

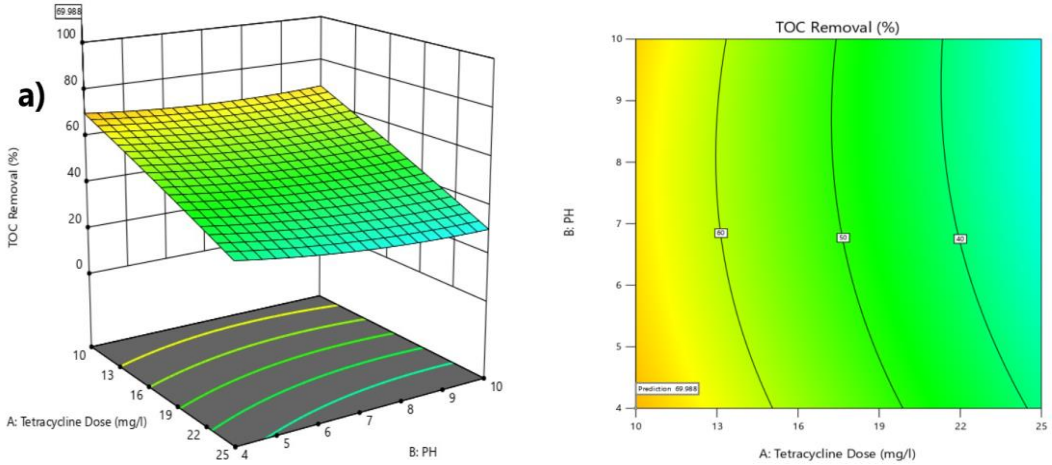

Figure 4.30: (a) Response surface plot for Tetracycline dose and pH, (b) Contour plot for Tetracycline dose and pH

The disc shaped contours indicate minimal interaction between the factors confirmed by the high p-value (AB) > 0.05. The RSM graph 4.30 (a) showed that an inverse linear relationship existed between %TOC removal and tetracycline dose. This could be attributed to the high pollutant concentration lead to saturation of catalyst surface with the contaminant. On the other hand, extreme pH values (4 and 10) achieved the highest TOC removal. This could be explained by at alkaline pH, there was excess of hydroxyl ions which reacted with catalyst surface to form hydroxyl radicals (Borthakur & Saikia, 2019). Besides, highly alkaline environments have been reported to hydrolyze the unstable aromatic rings of pollutant molecules in mineralization reactions (Attarikhasraghi et al., 2021).

The interaction between pH and catalyst dose is shown in Figure 4.31(a, b).

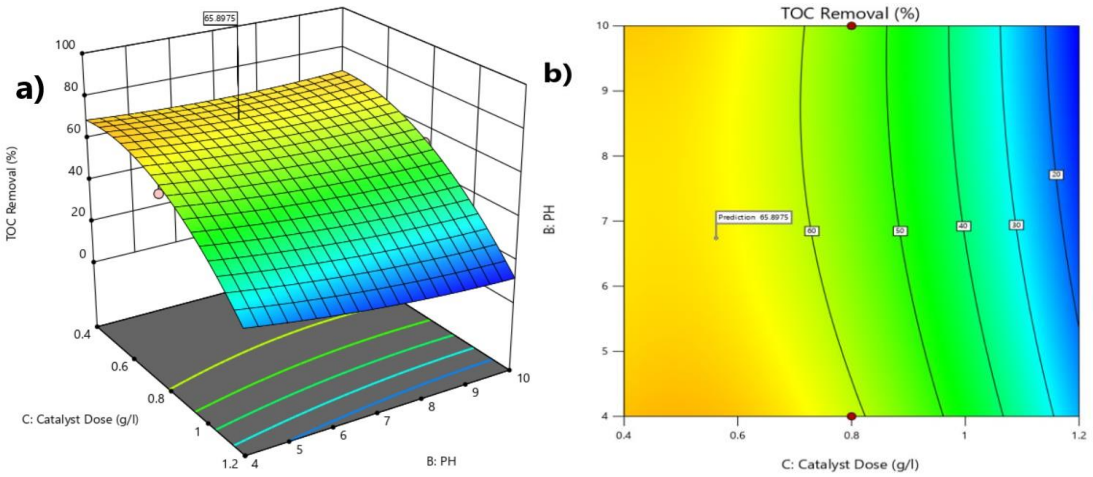

Figure 4.31: (a) Response surface plot for pH and catalyst dose, (b) Contour plot for pH and catalyst dose

The contour lines are slightly elliptical which shows significant interaction between the variables. According to the RSM graph 4.31 (a), the highest TOC removal was observed at the lowest catalyst dosage. Besides, as the catalyst dose increased, the TOC removal decreased. This phenomenon could be attributed to the influence of Eosin Y dye present in the sensitized photocatalyst, which increased the total organic carbon in the mixture. Figure 4.32(a, b) shows the response surface plots for catalyst dose and pollutant concentration.

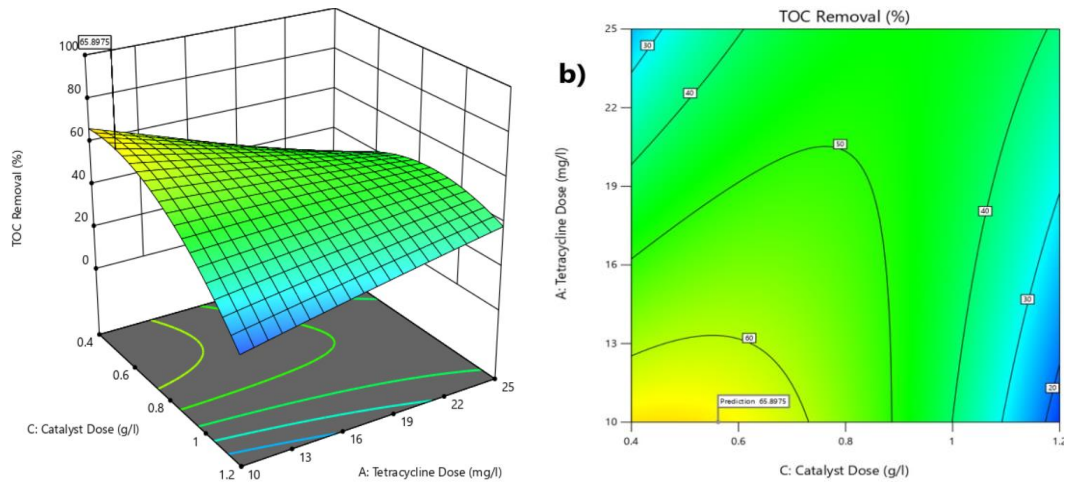

Figure 4.32: (a) Response surface plot for Tetracycline dose and catalyst dose, (b) Contour plot for Tetracycline dose and catalyst dose

The prominent elliptical contours are evidence of high degree of interaction between the two variables, confirmed by the low p-value of AC. The contour graph 4.32 (b) shows that the highest TOC Removal (> 60%) occurred at a catalyst dose of 0.4-0.7g/l and a pollutant dose of 10-12mg/l. Further increase in both catalyst and pollutant dose led to a decrease in TOC removal. This showed the synergies between the two variables in influencing %TOC removal. Moreover, at high catalyst dosage the solution turbidity increased which obscured solar light in the reaction medium.

4.3.5 Optimization of Tetracycline Degradation and TOC Removal

The desirability function was used in obtaining the global optimum for the combined responses and the localized optimum for single responses as shown in Figure 4.33.

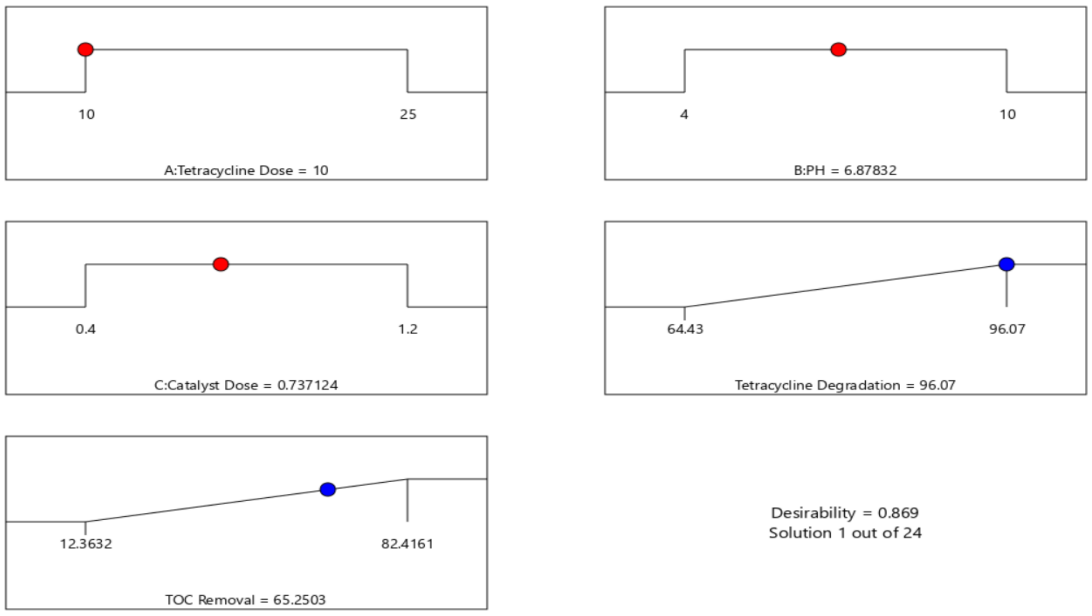

Figure 4.33: Global optimum parameters after optimization of Degradation and TOC Removal

The overall optimum degradation parameters for the two responses were: tetracycline dose=10mg/l, pH=6.88, catalyst dose=0.737g/l and a predicted yield of 96.07% degradation and 65.203% TOC removal at a desirability of 86.90%.

4.3.6 Single Factor Studies for Tetracycline

4.3.6.1 Effect of operating pH

The effect of solution pH is one of the most critical parameters that affect photocatalytic processes. The effect of pH on tetracycline degradation was studied in the pH range (pH 4-12) at the fixed conditions of 10mg/l pollutant dose, 0.7g/l catalyst dose, and 90 minutes irradiation time. The results are shown in Figure 4.34(a, b).

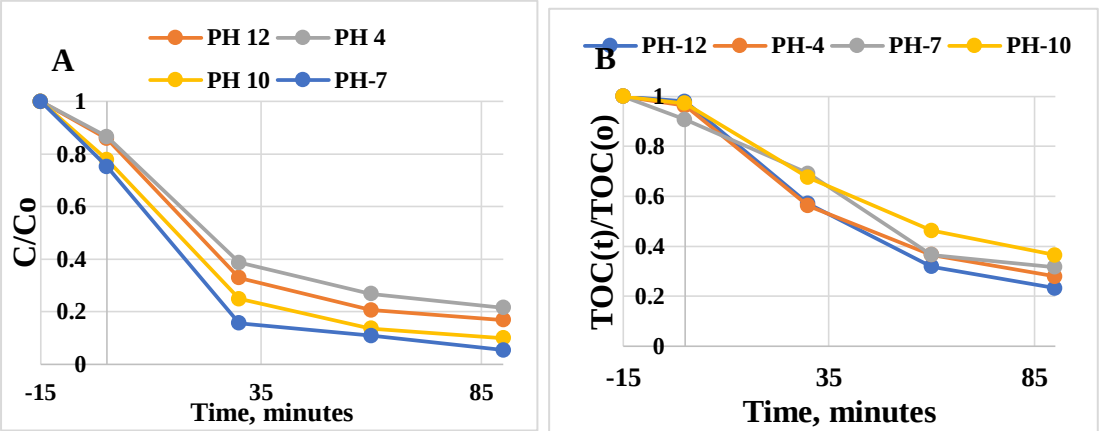

Figure 4.34: Plot of TTC concentration with time at various pH values; (A) TTC degradation, (B) TOC Removal

They indicate that in the first 15 minutes carried out in the dark, the removal efficiencies by adsorption were as follows: 15.48%, 16.26%, 20.17%, and 20.02% for pH 4, pH 12, pH 7 and pH 10, respectively. The results show that at extreme pH values, there is decreased adsorption of tetracycline molecules on the catalyst surface due to increased coulombic repulsion between catalyst and molecules. The overall degradation efficiency after 90 minutes of irradiation time was 78.48%, 94.62%, 90.02% and 83.12% for initial pH of 4, 7, 10 and 12, respectively. The high degradation efficiency observed at pH 7 could be explained by the influence of the point of zero charge on the surface charge of the catalyst as well as the pKa value of the pollutant. The photocatalyst has a pH_{pzc} =5.91 (Dai et al., 2021), while tetracycline is amphoteric and has three pKa values with pKa_1=3.3, pKa_2=7.7 and pKa_3=9.0. The amphoteric nature

of tetracycline means that it exists in four ionic forms at different pH values as follows: (TC_3^+ when pH < pKa_1, TC_2^+ when pKa_1 < pH < pKa_2, TC^- when pKa_2 < pH < pKa_3 and, TC^{2-} when pH < pKa_3) (Ciğeroğlu et al., 2023). At pH 7, the photocatalyst surface was negatively charged since the solution pH 7 > pH_{pzc}. However, tetracycline molecules exist as TC_2^+, which is positively charged since pKa_1 < pH 7 < pKa_2. This implied that more tetracycline molecules were adsorbed on the catalyst surface, resulting in increased photocatalytic performance. However, low degradation was observed at pH 4, where both catalyst and TC_3^+ are positively charged. This could have resulted in increased repulsion, which decreased the adsorption of pollutants. A similar study by Trang et al. degraded tetracycline at various initial pH of 5, 7, 9 and 11 using g-C_3N_4/Ga-N-ZnO composite. The highest degradation was 94.3%, at neutral pH, which was attributed to the catalyst and the pollutant molecules having opposite charges (Trang et al., 2021).

The order of TOC removal was pH 12 > pH 4 > pH 7 > pH 10, with removal efficiencies of 76.75%, 72.02%, 68.29%, and 63.55%, respectively. The high TOC removal observed at pH 12 could be explained based on LC-Ms studies. Previous studies of LC-Ms reported that N-demethylation, hydroxylation and cleavage processes are the main mechanism for intermediate formation in tetracycline degradation (Deng et al., 2018; Felis et al., 2022; Samy et al., 2020; Yang et al., 2023). Hydroxylation reactions are the more dominant processes favored by alkaline pH due to the abundance of hydroxyl ions and radicals, which directly react with the pollutant to form hydroxylated products. The hydroxylated products are further degraded by •OH radicals to smaller molecular groups (Samy et al., 2020a).

4.3.6.2 Effect of catalyst dose

The effect of catalyst concentration in tetracycline degradation was studied in the range of 0.5-2.5g/l at fixed conditions of 10mg/l pollutant dose, pH 7 and 90minutes irradiation time. The graph of how tetracycline concentration and TOC removal varied with time is shown in Figure 4.35 (a, b).

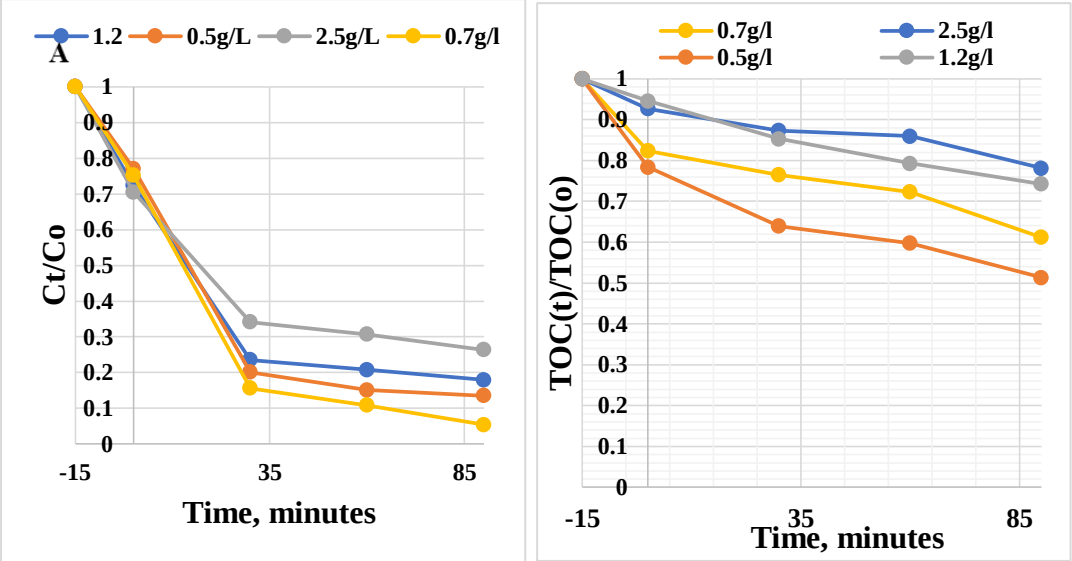

Figure 4.35: Plot of TTC concentration with time at various catalyst dosages: (A) TTC degradation, (B) TOC Removal

The results show that for the first 15minutes, which was carried out in the dark, the removal efficiencies were 22.92%, 24.33%, 27.565% and 29.52% for 0.5g/l, 0.7g/l, 1.2g/l and 2.5g/l, respectively. Similarly, the TOC removal efficiencies were 70.43%, 68.29%, 61.39% and 13.34% for 0.5g/L, 0.7g/l, 1.2g/l and 2.5g/l catalyst, respectively. It was evident that by increasing the catalyst dose during the dark experiment, there is an increase in the adsorption of pollutant molecules on the catalyst surface due to increased number of active sites and larger surface area (Le et al., 2019). After 90minutes irradiation, it was observed that when the catalyst dosage was increased from 0.5-0.7g/l, the degradation efficiency increased from 86.43% to 94.22%. However, further increases in catalyst dose to 1.2g/l and 2.5g/l lead to a drastic decrease in degradation efficiency to 82.03% and 73.64% respectively. The initial increase in

photocatalytic degradation of tetracycline with catalyst dose is due to an increase in surface active sites necessary for the generation of oxidative/reductive radicals (Musa & Gaya, 2019; Trang et al., 2021). On the other hand, the observed reduction in degradation efficiency at higher catalyst loading is due to increased turbidity of the catalyst, which scatters light photons, hindering them from reaching active sites thus inhibiting radical generation (Minh et al., 2019). Furthermore, at high catalyst loading, some studies have reported an increase in particle agglomeration, decreasing the available active sites (Samy et al., 2020). The poor TOC removal observed at high catalyst loading reinforces the impact of increased turbidity, which causes light scattering, and consequently low generation of radicals.

4.3.6.3 Effect of initial pollutant concentration

The effect of different tetracycline concentrations (10-40mg/l) was studied at the fixed conditions of pH 7, catalyst dose 0.7g/l and irradiation time of 90minutes. The graph of how initial tetracycline concentration and TOC removal varied with time is shown in Figure 4.36 (a, b).

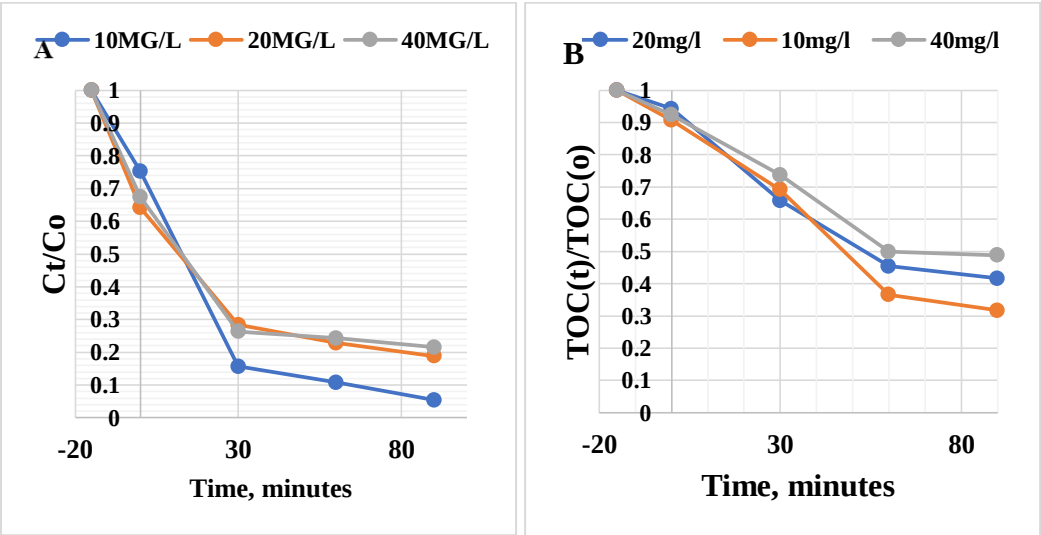

Figure 4.36: Plot of pollutant concentration with time at various pollutant dosages: (A) TTC degradation, (B) TOC removal

The results show that degradation efficiency was inversely related to the pollutant concentration since degradation decreased from 94.62 to 78.47%, for 10–40mg/l concentrations, respectively. Similarly, the TOC removal decreased with increasing pollutant concentration from 68.29 – 51.18% for 10-40mg/l, respectively. This could be due to at low pollutant concentration; most of the active sites are unoccupied and thus available for the removal of pollutants. However, at higher pollutant concentration, there is increased light attenuation in the solution medium, which increases solution turbidity (Pham et al., 2021). The interference of ions causes light scattering, hence, fewer light photons will penetrate the reaction medium to access the active site of the photocatalyst (Deng et al., 2018).

The decrease in TOC removal with increasing catalyst dose may be attributed to the saturation of active sites with the pollutant, which hinders the formation of radicals. Furthermore, more intermediates products are produced at higher pollutant doses, which increases the competition for active sites with the parent molecule, hence a decrease in TOC removal.

4.3.7 Possible Degradation Pathways for Trimethoprim

According to most researchers, N-demethylation, hydroxylation and cleavage processes are the primary mechanisms for intermediate formation in tetracycline (Deng et al., 2018; Felis et al., 2022; Samy et al., 2020; Yang et al., 2023). Tetracycline has a condensed formulae of ($C_{22}H_{24}N_2O_8$) and a mass-to-charge ratio (m/z) of 445 (Wu et al., 2023). OH• radicals break down the parent molecule into simpler intermediates such as; $C_{22}H_{26}O_9$, $C_{22}H_{23}NO_9$, $C_{12}H_{12}O_4$ and carboxylic acid (Adenuga et al., 2021). A study by (Deng et al., 2018) on the reaction intermediates of tetracycline produced from P-g-C_3N_4/$BiVO_4$ photocatalysis. The study found that after 30minutes of irradiation, intermediates with a m/z of 495, 490, 477, 461, 459, 431, 427 and 417 appeared. He

attributed the intermediates to N-demethylation and hydroxylation reactions. The OH radicals attacked the TTC molecules to produce hydroxylated product. Besides, demethylation reactions, that break low energy N-C bonds were responsible in generating lower intermediates with less m/z (Deng et al., 2018).

4.3.8 Comparison of TMP and Tetracycline Degradation

For all reactions carried out at uniform conditions, tetracycline achieved higher degradation and %TOC removal efficiencies than trimethoprim, as shown in Figure 4.37(a, b).

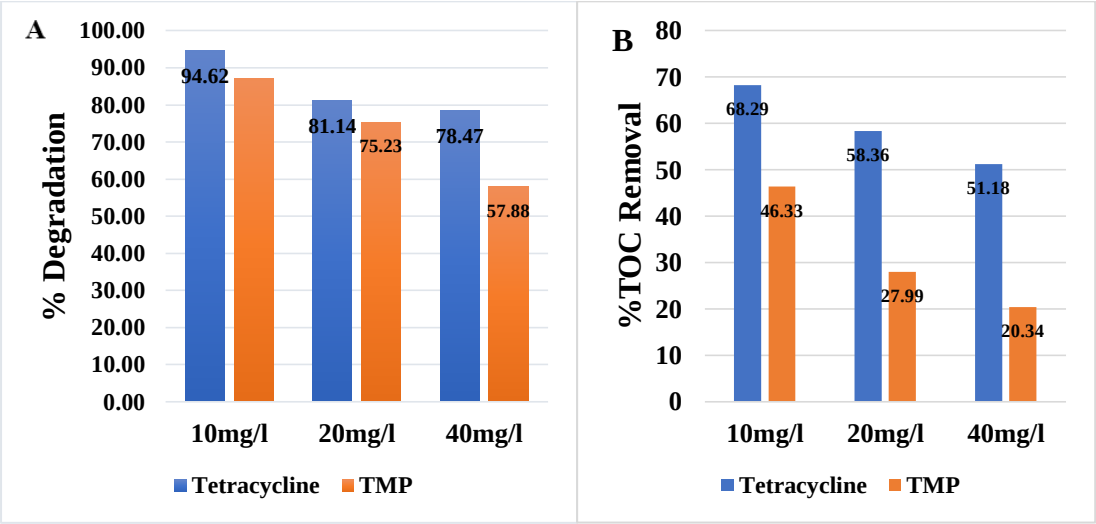

Figure 4.37: Comparison of Photocatalytic Performance of Tetracycline and Trimethoprim: (A): Photodegradation, (B): %TOC Removal

This phenomenon could be attributed to the fact that tetracycline is a light-yellow highly soluble powder with an absorption wavelength of between 300-400nm as opposed to colorless low water-soluble trimethoprim. Therefore, the colored tetracycline molecules could be sensitized by solar light, enhancing their photocatalytic degradation (Adenuga et al., 2021). Similar mechanisms have also been observed during the photodegradation of methyl orange dye, where sunlight activates both catalyst and pollutant, leading to generation of oxidative species hence improving the degradation (Diaz-angulo et al., 2019).

4.3.9 Effects of Dopant Loading and Controls

All the prepared composites (0, 5, 15, 25% ZF-GCN) were tested for their degradation and mineralization efficiency at the optimal condition of 10mg/l tetracycline, pH 7, 0.7g/L catalyst and 90minutes irradiation time. Figure 4.38 shows the photocatalytic performance of the photocatalysts under solar irradiation.

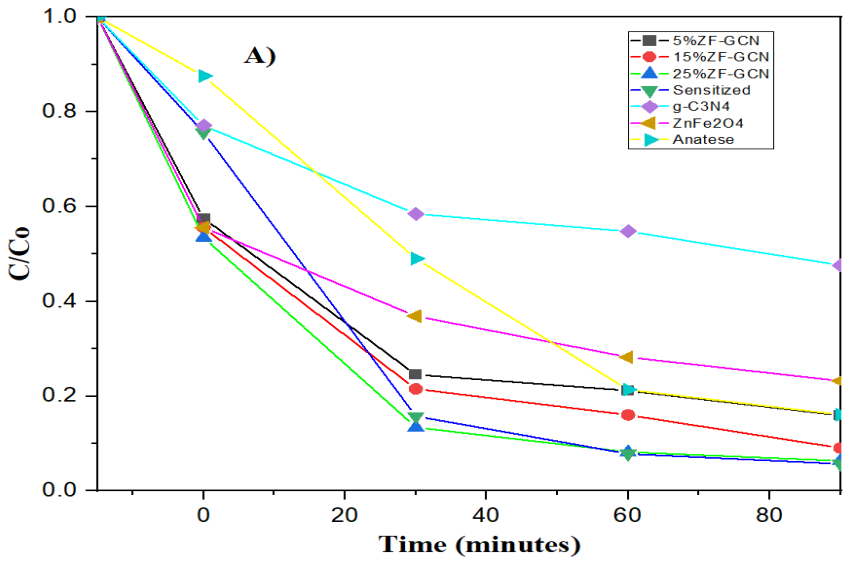

Figure 4.38: Photodegradation of tetracycline using various photocatalysts

For the first 15minutes carried out under dark conditions, the 5, 15 and 25%ZF-GCN composite had a remarkable adsorption efficiency compared to g-C_3N_4 and the sensitized composite. This could be possibly attributed to the improved surface area and affinity for tetracycline molecules in the composites (N. Liu et al., 2022). Figure 4.38 shows that the degradation efficiency of tetracycline follows the order; EY-25%ZF-GCN > 25%ZF-GCN > 15%ZF-GCN > 5%ZF-GCN > Anatase > ZF > GCN. The sensitized photocatalyst achieved the best photocatalytic performance at 94.62%. This could be explained by the improved charge separation and better light photon harvesting (Chen et al., 2021). Similarly, all the composites performed significantly higher than all the pure photocatalysts. Besides, an increase in $ZnFe_2O_4$ composition was accompanied by increased photocatalytic activity. This could be attributed to the

synergistic interaction between the two semiconductors, which resulted in prolonged charge separation, higher specific surface area and enhanced light absorption (Basaleh, 2021). However, Chen et al. reported that when the proportion of $ZnFe_2O_4$ was increased above 67% in the composite, there was a significant reduction in photocatalytic activity due to poor dispersion and large crystallite size, which hinder charge mobility (Chen et al., 2016).

Eventually, the dye-sensitized composite had the best overall photocatalytic performance as shown by its kinetic rates in Figure 4.39.

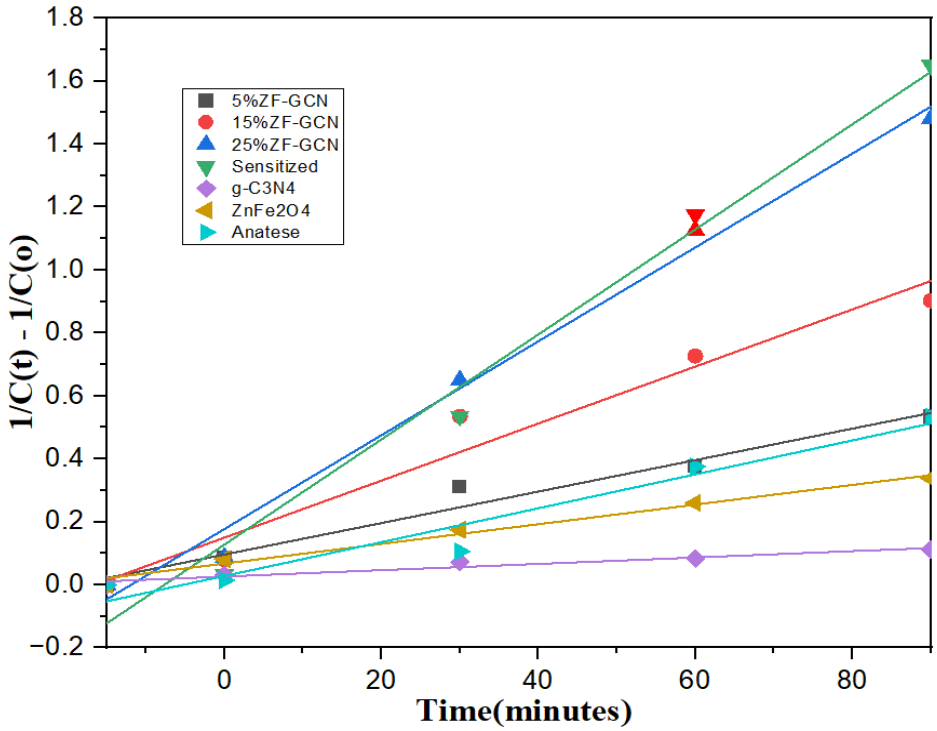

Figure 4.39: Tetracycline removal kinetics of as-synthesized photocatalysts

It outperformed the 25%ZF-GCN 1.118 times, 15%ZF-GCN 1.82 times, 5%ZF-GCN 3.31 times, Anatase-Titania 5.04 times, $ZnFe_2O_4$ 5.34 times and 16 times better than g-C_3N_4 based on the calculated kinetic rates as shown in Table 4.8.

Table 4.8: Kinetic constant comparison of composites

Photocatalyst	**k_{app} ($x10^{-3}$)**	**Comparison with sensitized**
Sensitized	16.68	1
25%ZF-GCN	14.91	1.118
15%ZF-GCN	9.16	1.82
Anatase (TiO_2)	5.38	3.10
5%ZF-GCN	5.04	3.31
g-C_3N_4	1.01	16.52
$ZnFe_2O_4$	3.12	5.34

The second-order kinetics could fit the degradation data adequately for all the photocatalysts since the coefficient of determination, R^2 ranged between 0.94-0.99, see Table I.2 in the Appendix. Therefore, this remarkable improvement in photocatalytic activity is evidence of the potential of dye sensitization as a photocatalyst modification strategy. A similar study by Musa et al. on caffeine degradation using Eosin Y dye-sensitized Ag-TiO_2 and plain Ag-TiO_2 found a higher removal of 95% against 52% in 290 minutes, respectively (Musa & Gaya, 2019). Furthermore, a study by Li et al. on the degradation of 2,4-DCP using 15wt% Eosin Y/$BiPO_4$ composite obtained apparent reaction rates 10.5 fold higher than plain $BiPO_4$ (Li et al., 2019). According to these studies, it can be observed that Eosin Y sensitization of a photocatalyst improves its photocatalytic performance.

A decrease in maximum absorbance intensity for tetracycline as measured by UV/Vis is not evidence for its complete mineralization to CO_2 and H_2O (Jo et al., 2020). Therefore, TOC removal was measured for all the composites and pure photocatalysts to determine the extent of mineralization. The TOC removal results showed similar trends to the degradation results obtained by UV/Vis as shown in Figure 4.40(a, b).

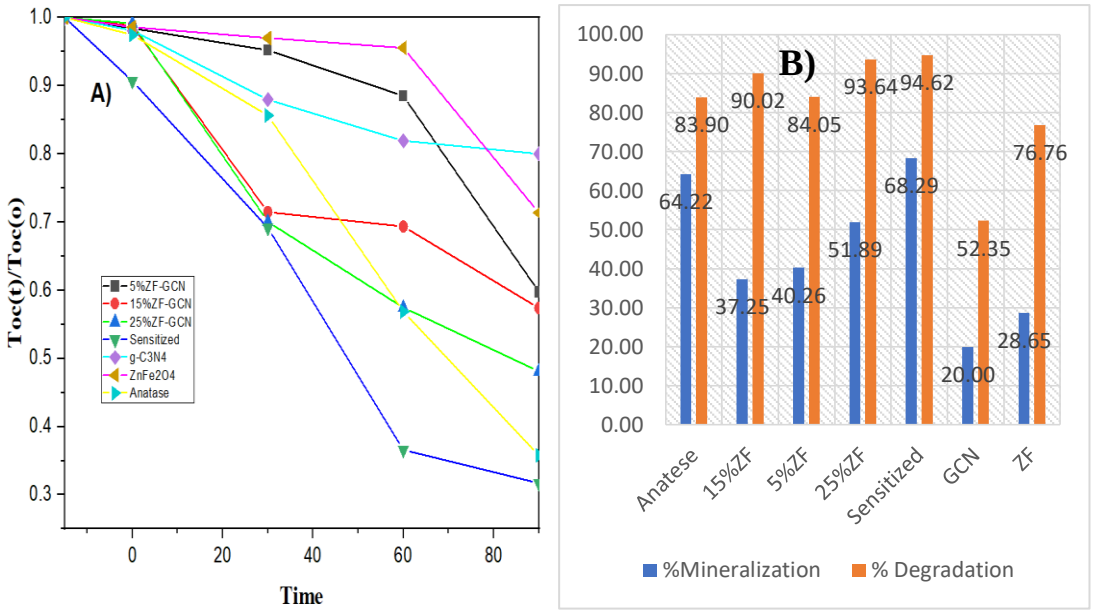

Figure 4.40: (A) TOC Removal of tetracycline, (B) Comparison plot for Degradation and TOC Removal

The TOC removal followed the order; EY-25%ZF-GCN > Anatase > 25%ZF-GCN > 15%ZF-GCN > 5%ZF-GCN > ZF > GCN. The dye-sensitized photocatalyst had the highest removal efficiency of 68.29%, followed closely by anatase (TiO_2) at 64.22%, which proves the comparability of the as-synthesized photocatalyst with that of commercial ones. Interestingly, all the other composites achieved a higher mineralization efficiency than for the pure photocatalysts. The higher performance of composites compared to pure photocatalysts is evidence of the enhanced photocatalytic activity as a result of constructing the type-II heterojunction. Furthermore, dye sensitization of the catalyst improves both the degradation and mineralization of pollutant molecules which can be attributed to the increased generation of oxidative radicals during electron transfer from the excited dye molecule to the conduction band of the photocatalyst (Diaz-angulo et al., 2019). Nonetheless, none of the photocatalysts achieved 100% mineralization of tetracycline, but by increasing the reaction time for photocatalytic systems, it is possible to mineralize all the transformational products (Adenuga et al., 2021).

4.4 Degradation study of Real wastewater and Effects of Competing ions

4.4.1 Characterization of Real Wastewater Sample

The collected wastewater was analyzed for its physicochemical properties. Table 4.9 shows a summary of the characterization results.

Table 4.9: Characterization of the wastewater used in this study

Parameter	Actual	Maximum limits for discharge	Standard Body
pH	9.62	pH 6.5 – 8.5	NEMA
Conductivity	1890μS^{-1}/cm	2500 μS^{-1}/cm	EPA
Turbidity	175 FTU	5 FTU	KEBS
Temperature	25.5^{o}C	+/-3 ambient Temp	NEMA
TOC	25.63mg/L	30mg/l	NEMA
UV 254	0.174	-	-
Total Nitrogen	3.30mg/l	10mg/l	USEPA
Tetracycline*	20mg/l	-	-

The pH value of the water sample exceeded the maximum permissible discharge levels as per NEMA standards. High pH values in a WSP can be attributed to microbial activities such as ammonification, which release excess NH_3^+ ions (Mosley, 2018). The UV-254 is a precursor for identifying aromatic rings/unsaturated compounds in water (Shakhawat, 2022). Thus, the presence of aromatic groups in the wastewater was confirmed, which could be attributed to natural organic matter (NOM). The TOC test indicates the organic pollution level in the wastewater (Lee et al., 2020). The TOC test showed some significant level of organic contamination, which could be attributed to recalcitrant pollutants. The conductivity values were slightly lower than the recommended limits. Conductivity is directly related to the total dissolved solids by a factor of 0.55~0.9 (Marandi et al., 2013). Thus, conductivity is a precursor of the molar charges of common ions such as Cl-, HCO_3^- and SO_4^{2-}. High conductivity is attributed

to high chloride concentration, while low conductivity is due to SO_4^{2-}. Nonetheless, the tetracycline concentration in wastewater was spiked with a pure standard.

4.4.2 Degradation study of Real wastewater

4.4.2.1 Effect of Pollutant Concentration

Figure 4.41 shows the photocatalytic performance of 10, 20, 40mg/l of tetracycline doses spiked in real wastewater.

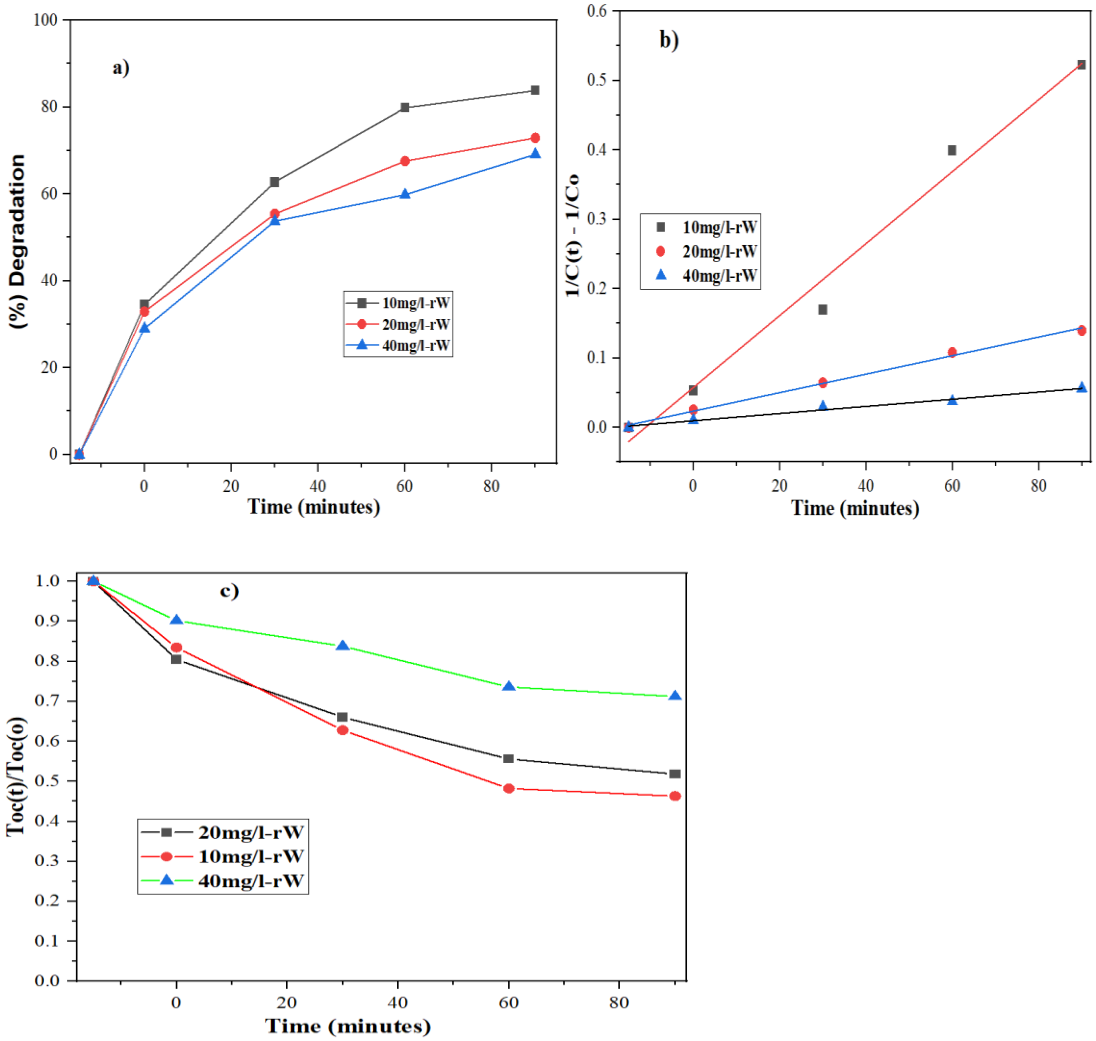

Figure 4.41: (A) Photocatalytic performance of composite at various tetracycline doses, (B) Pseudo second-order degradation kinetics for various tetracycline doses, (C) TOC removal efficiency at different tetracycline doses

These results indicate that the degradation efficiency decreases with increasing pollutant concentration from 83.84-69.13% for 10- 40mg/l, respectively. Similarly, the

degradation constant (k_{app}) shown in Figure 4.41b decreases with increasing pollutant concentration as follows: 0.00519, 0.00133 and 0.000517 for 10, 20, 40mg/l, respectively. The pseudo-second-order model used in fitting the data showed a high degree of correlation, since the R^2 ranges between 0.98-0.99; see Table I.3 in the Appendix. This confirmed the validity of the linear models. The TOC removal shown, in Figure 4.41c, agreed with the other two parameters in that the removal efficiency decreased from 53.70% to 28.79% with an increase in substrate load from 10 to 40mg/l.

The decrease in degradation at high pollutant doses was probably due to the saturation of the catalyst surface by tetracycline molecules, which blocked the active sites from light illumination, hence decreasing the generation of oxidative radicals (Tanwar & Mandal, 2019). Furthermore, competition for active sites between the pollutant molecules and reaction intermediates could slow kinetics and decrease TOC removal at large tetracycline doses (Su et al., 2021).

4.4.2.2 Comparison of degradation rates for RW and SW

Comparison studies for real wastewater matrix (RW) and synthetic water (SW) are shown in Figure 4.42.

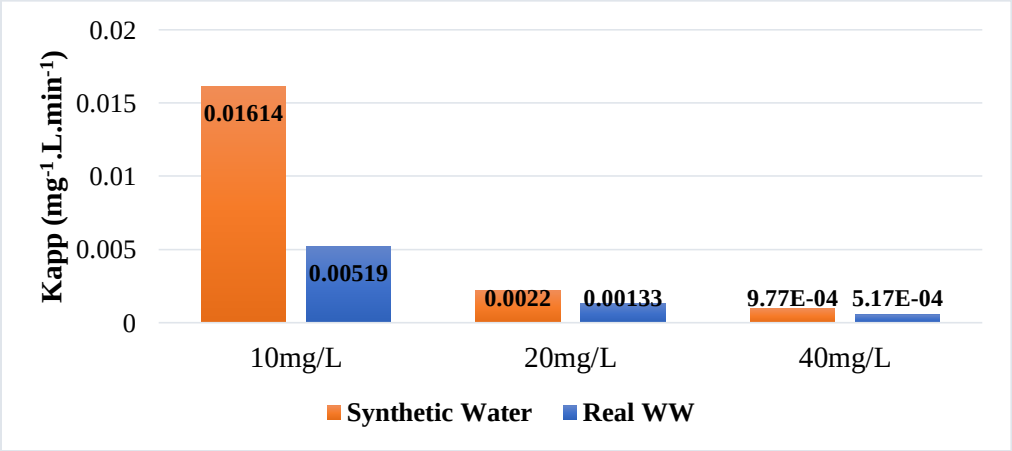

Figure 4.42: Comparison of kinetic constant for tetracycline degradation in real wastewater and synthetic wastewater

The results from all experiments show that synthetic wastewater had a higher degradation constant (k_{app}) than real wastewater. At 10mg/l, the kinetics of SW was 3.1 times faster than RW, at 20mg/l, the SW kinetics was 1.65 times faster than RW and at 40mg/l, the SW kinetics was 1.89 times faster than RW. The decreased degradation rates observed in RW were likely due to negative interference by both organic and inorganic species present in wastewater. The organic species originate from the high initial TOC of real wastewater, which contains both natural organic matter (NOM) and other undegraded recalcitrant pollutants. Therefore, these pollutants inhibit tetracycline degradation as follows: (i) strongly compete with tetracycline molecules for the catalyst active surface and reactive radicals in the reaction solution, (ii) NOM molecules may cause light attenuation in the reaction solution by acting as a light filter for both UV and visible light hence reducing the number of light photons reaching the catalyst surface, (iii) inorganic species present in wastewater matrix may scavenge the e^-/h^+ or react with oxidative radicals generating low activity radicals hence reducing photocatalytic performance (Kutuzova et al., 2021; G. Silva et al., 2021).

Therefore, the synergistic interaction of inorganic and organic molecules contributes to the diminished degradation kinetics observed in real wastewater. This agrees with the literature since studies have found the value of k_{app} to decrease by one order of magnitude when degrading complex water matrices, containing high TOC and turbidity (Pretali et al., 2022).

4.4.2.3 Control experiment

Figure 4.43(a, b) shows the degradation efficiency and kinetics of 0.7g/l photocatalyst (5, 15, 25%ZF-GCN, EY-25%ZF-GCN, TiO_2, GCN and ZF) in real wastewater spiked with 10mg/l of tetracycline.

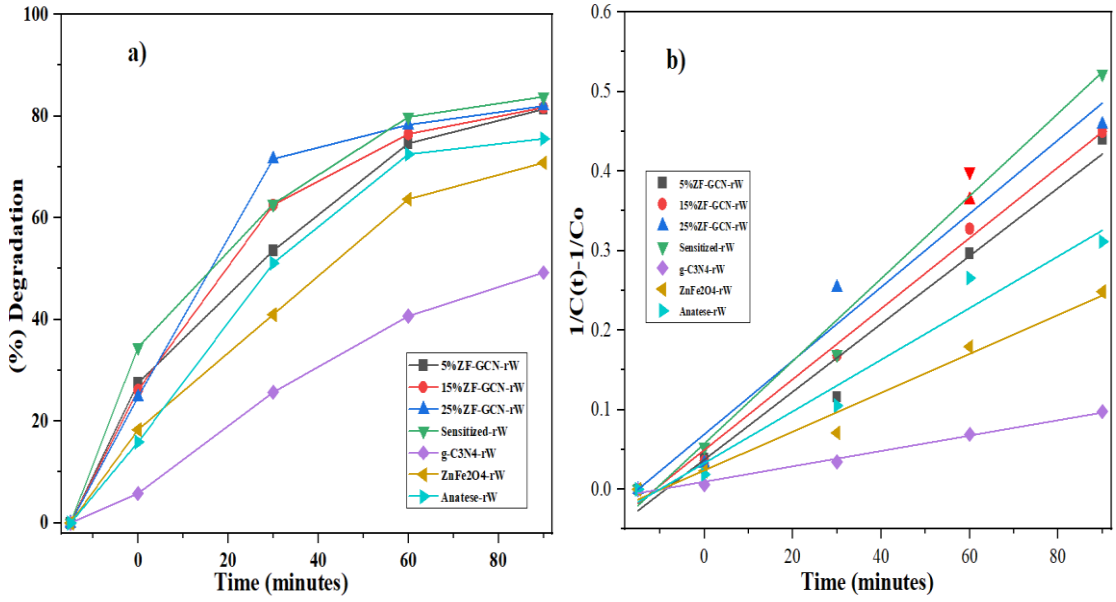

Figure 4.43: (A) Photodegradation of tetracycline in real wastewater using photocatalysts (B) Tetracycline removal kinetics of photocatalysts in real wastewater

The dye-sensitized photocatalyst (EY-25%ZF-GCN) had the highest degradation efficiency at 83.84% in 90minutes, compared to other photocatalysts. Therefore, the degradation efficiency increases with increasing ferrite dopant as follows: GCN (49.26%) < ZF (70.85%) < TiO_2 (75.58%) < 5%ZF-GCN (81.39%) < 15%ZF-GCN (81.70%) < 25%ZF-GCN (82.01%) < EY-25%ZF-GCN (83.84%). Similarly, the kinetic constant ($k_{app}x10^{-3}$) followed the same trend since the dye-sensitized composite had the highest rate constant. Therefore, it outperformed the 25%ZF-GCN 1.11 times, 15%ZF-GCN 1.17 times, 5%ZF-GCN 1.22 times, Anatase-Titania 1.57 times, $ZnFe_2O_4$ 2.12 times and 5.38 times better than g-C_3N_4 based on the calculated kinetic rates as shown in Table I.4 in Appendix.

The high degradation rate of the EY-25%ZF-GCN could be accredited to the sensitization effect of Eosin Y dye. Besides, the heterojunction formed at 25% ferrite concentration aids in enhanced separation of photogenerated charges; hence the charge

can proceed to the catalyst surface for redox reactions (Diaz-angulo et al., 2019; Kumar et al., 2020).

4.4.3 Effects of Anions on Photodegradation of tetracycline

4.4.3.1 Effect of Chloride ions

Figure 4.44(a, b) shows tetracycline's photocatalytic degradation and kinetic plots at various Cl- concentrations.

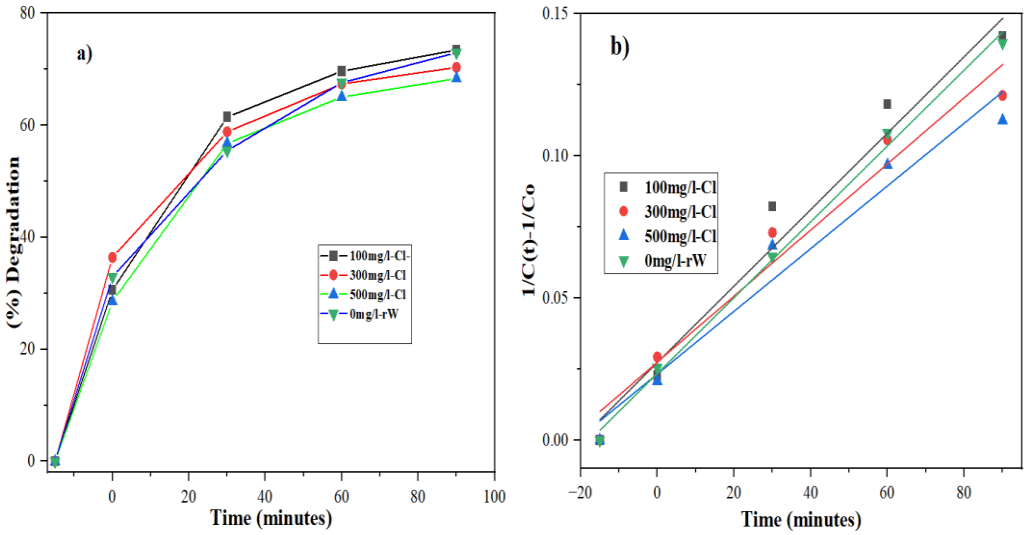

Figure 4.44: The effect of Cl- on (a) Tetracycline degradation, (b) Apparent kinetic constant (Tetracycline dose=20mg/l, pH 9.62, catalyst dose =0.7g/l)

The degradation performance was as follows: 68.32%, 70.32%, 72.94% and 73.37% for 500, 300, 0 and 100mg/l Cl-, respectively. Likewise, the pseudo-second-order model was used to monitor tetracycline degradation in the presence of Cl-. The apparent kinetic constant decreased with increasing chloride concentration as follows: $1.1*10^{-3}$, $1.16*10^{-3}$, $1.33*10^{-3}$ and $1.34*10^{-3}$ for 500, 300, 0 and 100mg/l Cl^-, respectively. The second-order kinetics could fit the degradation data adequately for all the chloride concentrations since the coefficient of determination R^2 ranged between 0.94-0.99, see Table I.5 in Appendix. It is evident that chloride's effects in degradation are dual in nature since high Cl- concentrations tend to inhibit the photocatalytic degradation while low Cl- concentration tend to promote degradation.

It can also be seen from Figure 4.45 that a decreasing linear relationship (y = -5E-07x+0.0014, R^2 = 0.9221) exists between Cl- concentration and K_{app}.

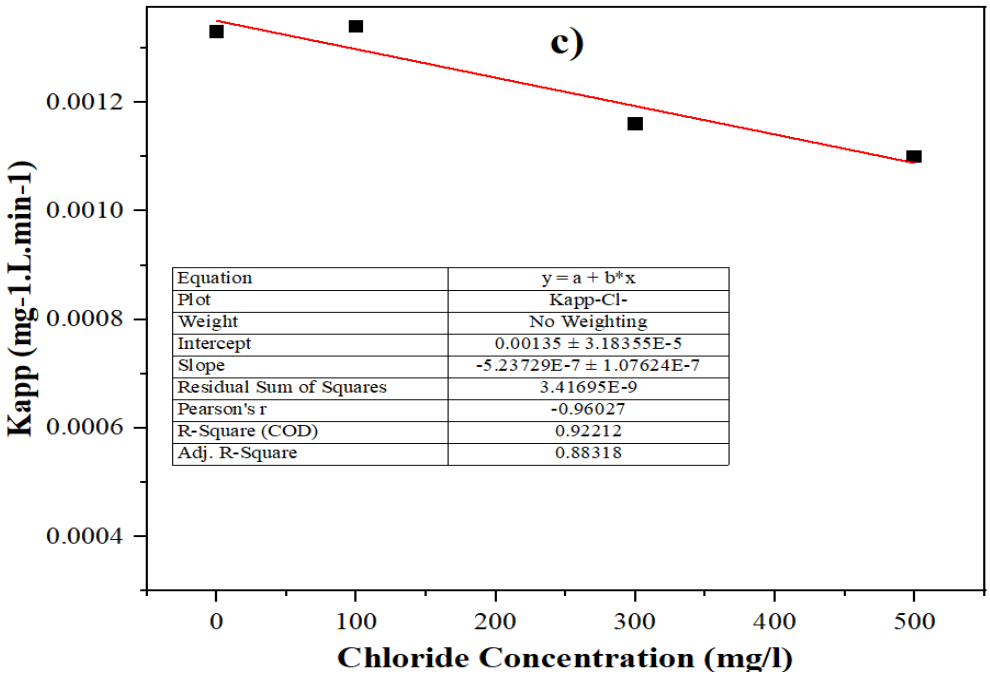

Figure 4.45: Linear fit of kinetic constant with Cl- concentration

The gently inclined slope indicates the low inhibition effect of various chloride doses on tetracycline degradation. The inhibition effects on K_{app} for the different Cl- concentration were; -17.29% > -12.78% > 0.75% for 500, 300 and 100mg/l Cl- concentrations, respectively. These findings agree with literature since two separate studies by Dong et al. and Chakkunny et al. both reported that at low chloride concentrations, there was increased kinetic degradation constant, while high doses inhibited degradation (Chakkunny et al., 2021; Dong et al., 2021).

The observed high photocatalytic activity at low chloride concentration is due to the rapid scavenging of holes and electrons by chloride and dichloride radicals. This reduces the charge recombination and enhances degradation (Chakkunny et al., 2021). The reaction mechanism involves chloride ions reacting with h^+ and •OH, yielding chlorine radicals (Cl•) as shown in Eqn 4.5-4.9. The Cl• may also attack the pollutant

molecules leading, to degradation, hence the slight increase in removal kinetics. However, further increase in Cl- concentration beyond optimum concentration leads to increased scavenging of reactive radicals (•OH, h^+) to yield Cl• that may react with tetracycline molecules to form stable chlorinated derivatives which are resistant to degradation by Cl• (Gao et al., 2019). Additionally, at high chloride concentration there is increased competitive adsorption between Cl- anions and tetracycline molecules for the catalyst's active surface as well as for oxidative species, which may hinder the generation of •OH radicals, hence decreasing pollutant degradation (Azzaz et al., 2021; Chakkunny et al., 2021; Su et al., 2021).

$$Cl^- + h^+ \rightarrow Cl^\bullet \quad \text{Equation 4.5}$$

$$Cl^\bullet + Cl^- \rightarrow Cl_2^-\bullet \quad \text{Equation 4.6}$$

$$\bullet OH + Cl^- \rightarrow Cl^\bullet + OH^- \quad \text{Equation 4.7}$$

$$\bullet OH + Cl^- \rightarrow HOCl^{\bullet -} \quad \text{Equation 4.8}$$

$$HOCl^{\bullet -} + H^+ \rightarrow Cl^\bullet + H_2O \quad \text{Equation 4.9}$$

4.4.3.2 Effect of Nitrate ions

Figure 4.46 (a, b) shows the photocatalytic degradation and kinetic plots of tetracycline at various NO_3^- concentrations.

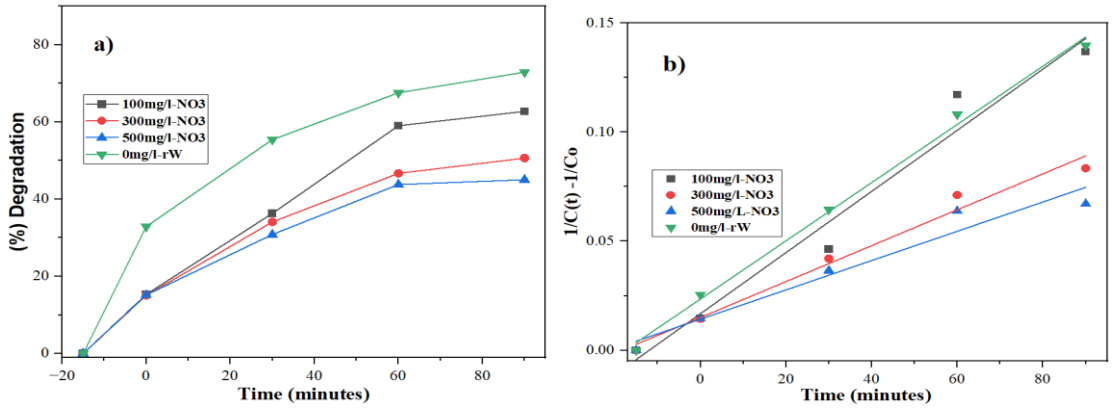

Figure 4.46: The effect of NO_3^- on; (a) Tetracycline degradation, (b) Apparent kinetic constant (Tetracycline dose=20mg/l, pH 9.62, catalyst dose =0.7g/l)

The degradation performance was as follows: 45.04%, 50.64%, 62.74% and 72.94% for 500, 300, 100 and 0mg/l NO_3^-, respectively. On the other hand, the second-order kinetics could fit the degradation data adequately for all the nitrate concentrations since the coefficient of determination, R^2 ranged between 0.95-0.99, see Table I.6 in Appendix. Therefore, the apparent kinetic constant was $0.675*10^{-3}$, $0.823*10^{-3}$, $1.33*10^{-3}$ and $1.4*10^{-3}$ for 500, 300, 0 and 100mg/l NO_3^-, respectively. Moreover, the results show that effects of nitrates in degradation is decreasing linear since an increase in the NO_3^- concentration is accompanied by a decrease in degradation efficiency. However, a similar trend is observed for the degradation kinetics but at the lowest NO_3^- concentrations tends to promote the degradation constant. These results agreed with the literature since a previous study by Gao et al. found NO_3^- to decrease the degradation of carbamazepine (Gao et al., 2019).

The results also show in Figure 4.47 that a decreasing linear relationship ($y = -2E-06x + 0.0014$, $R^2 = 0.8897$) exists between NO_3^- concentration and K_{app}.

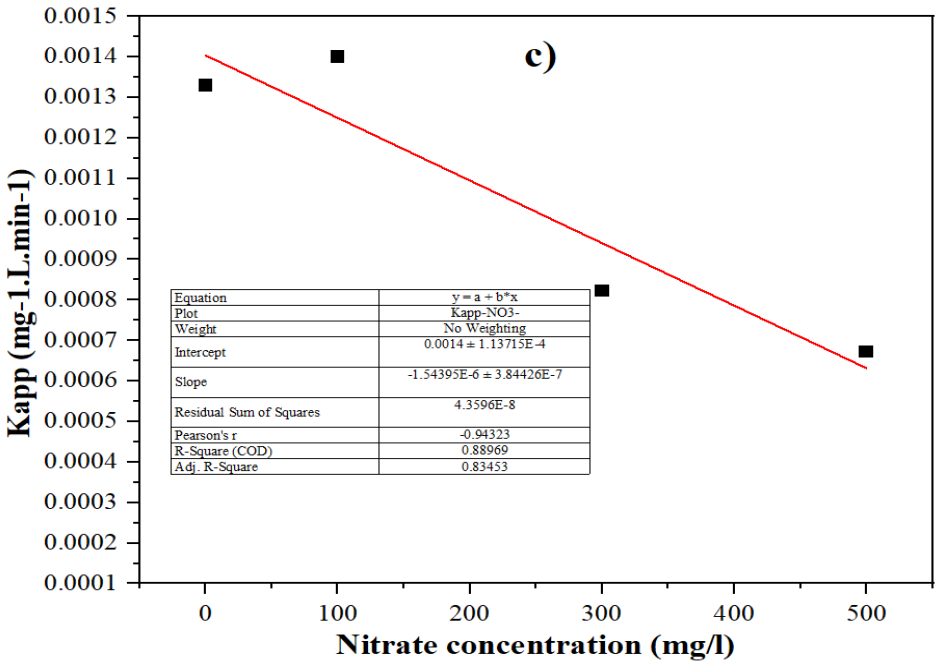

Figure 4.47: Linear fit of kinetic constant with NO_3^- concentration

The steep gradient indicates the high inhibition effect of NO_3^- on tetracycline degradation. Therefore, the inhibition effects of NO_3^- on degradation constant are as follows: -49.55% > -38.12% > 5.26% for 500, 300 and 100mg/l NO_3^- concentrations, respectively. These results were consistent with those obtained in a similar study by Liu et al. who found NO_3^- to inhibit the degradation of norfloxacin by -38% (Liu et al., 2020). The NO_3^- ions could have scavenged h^+, which retarded the generation of $^{\bullet}OH$, hence inhibiting the degradation process (Xie et al., 2019). Additionally, the more potent $^{\bullet}OH$ radicals may react with NO_3^-, generating the lower potential $NO_3^{\bullet-}$ that decrease the degradation rate as shown in Equation 4.10 – 4.11 (Gao et al., 2019).

$$NO_3^- + h^+ \rightarrow NO_3^{\bullet-} \quad \text{Equation 4.10}$$

$$NO_3^- + {}^{\bullet}OH \rightarrow NO_3^{\bullet-} + OH^- \quad \text{Equation 4.11}$$

4.4.3.3 Effect of Sulphate ions

Figure 4.48(a, b) shows the photocatalytic degradation and kinetic plots of tetracycline at various SO_4^{2-} concentrations.

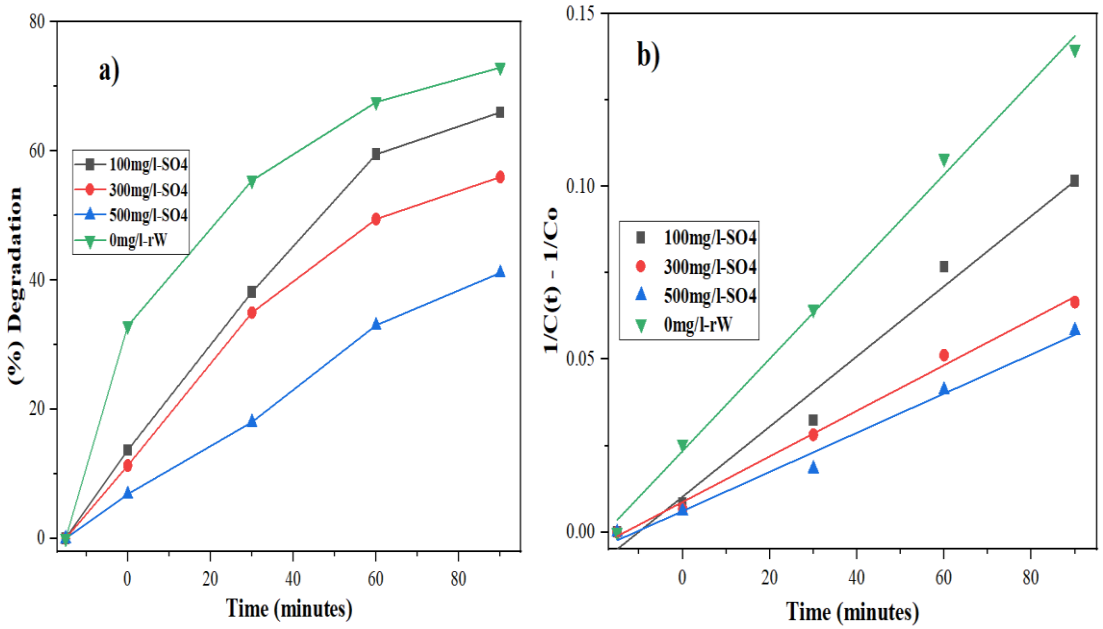

Figure 4.48: The effect of SO_4^{2-} on; (a) Tetracycline degradation, (b) Apparent kinetic constant

The degradation performance was as follows: 41.13%, 55.97%, 65.99% and 72.94% for 500,300,100 and 0mg/l SO_4^{2-}, respectively. On the other hand, the second-order kinetics could fit the degradation data adequately for all the SO_4^{2-} concentrations since the coefficient of determination, R^2 ranged between 0.97-0.99, see Table I.7 in the Appendix. Therefore, the apparent kinetic constant was $0.567*10^{-3}$, $0.66*10^{-3}$, $1.02*10^{-3}$ and $1.33*10^{-3}$ for 500, 300, 100 and 0mg/l SO_4^{2-}, respectively. From these results, it is shown that the effects of sulphates in degradation is negatively linear since an increase in the SO_4^{2-} concentration is accompanied by a decrease in degradation efficiency. Similarly, the kinetic constant follows a similar trend of a decreasing K_{app} with an increase in salt concentration.

Figure 4.49 shows the relationship between SO_4^{2-} concentration and degradation constant.

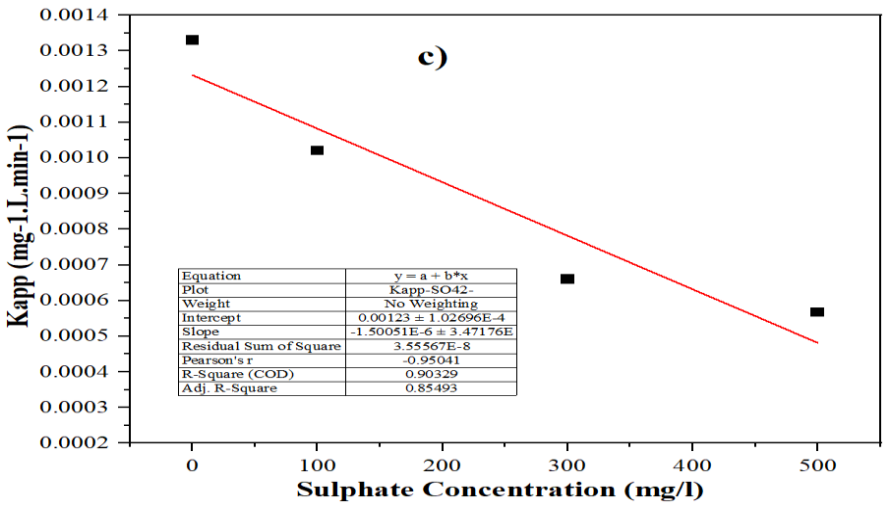

Figure 4.49: Linear fit of kinetic constant with SO_4^{2-} concentration

A linear relationship (y = -2E-06x+0.0012, R^2 = 0.9033) exists between the two variables. The steep slope observed indicates the high inhibition effect of SO_4^{2-} concentration on tetracycline degradation. Therefore, the inhibition effects on K_{app} for various SO_4^{2-} are as follows: -57.36% > -50.38% > -23.306% for 500, 300 and 100mg/l

sulfate ion concentrations, respectively. Similarly, a previous study by Tanwar and co-workers on the degradation of azo dye using polyaniline-sensitized $Ni_{0.5}Zn_{0.5}Fe_2O_4$/BiOCl, found sulphate ions to exhibit the highest inhibition effect among the anions tested. The observed inhibition order of anions was as follows: SO_4^{2-} > PO_4^{3-} > Cl^- > NO_3^- (Tanwar & Mandal, 2019). The results indicate that sulfate ions are strong inhibitors since they scavenge the reactive species from the solution, forming less reactive $SO_4^{\bullet-}$ radical that consequently quench electrons to form the unreactive SO_4^{2-} as shown by Equation 4.12 - 4.14 (Alfred et al., 2022; Yang et al., 2023). Besides, a preferential adsorption displacement mechanism may exist where the more electronegative SO_4^{2-} ions are selectively adsorbed on the catalyst's active surface, displacing the hydroxyl anions hence inhibiting hydroxyl radical formation (Gusain et al., 2020).

$$SO_4^{2-} + \bullet OH \rightarrow SO_4^{\bullet-} + OH^- \quad \text{Equation 4.12}$$

$$SO_4^{2-} + h^+ \rightarrow SO_4^{\bullet-} + OH^- \quad \text{Equation 4.13}$$

$$SO_4^{\bullet-} + e^- \rightarrow SO_4^{2-} \quad \text{Equation 4.14}$$

4.4.2.4 Mineralization Study

To verify the mineralization of tetracycline in the presence of salt (NaCl, $NaNO_3$, Na_2SO_4), TOC measurements were carried out for salt concentration of 100mg/l in real wastewater. Figure 4.50 shows the effect of different anions on TOC removal.

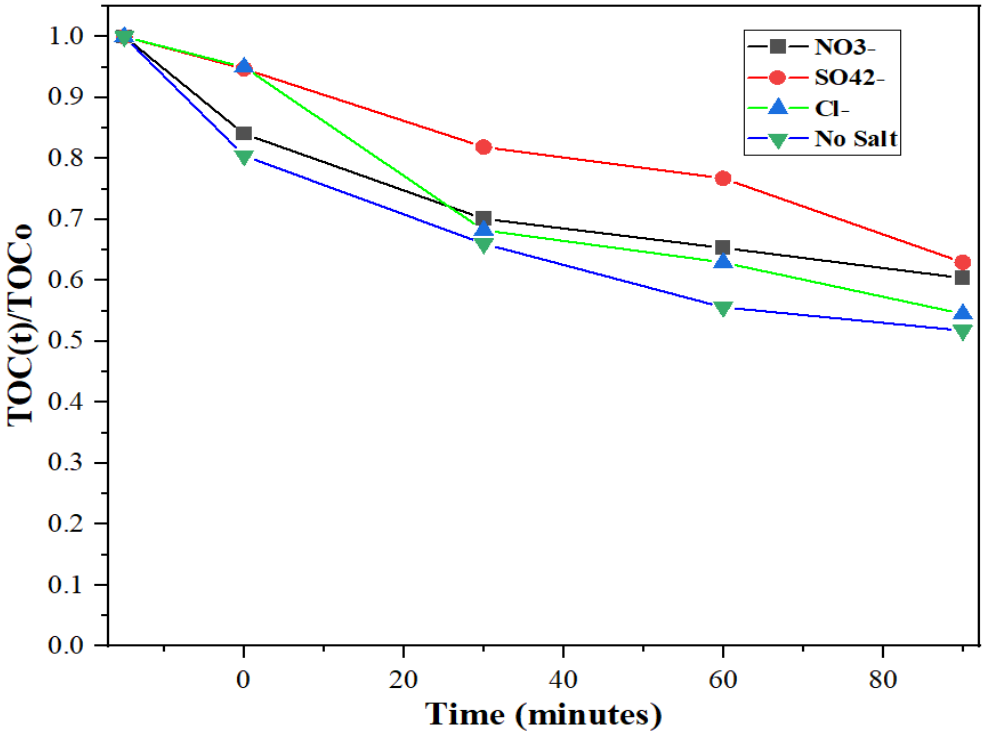

Figure 4.50: Effect of anions on TOC removal of tetracycline (salt dose $NaNO_3$, NaCl, Na_2SO_4=100mg/l, tetracycline dose=20mg/l, catalyst dose=0.7g/l)

The TOC removal follows the order: 48.20%, 45.47%, 39.56% and 37.02% for no salt, Cl-, NO_3^- and SO_4^{2-}, respectively. Despite the contrary during degradation, the no-salt matrix had a higher TOC removal than the Cl^- matrix. This can be possibly attributed to the formation of stable chloride intermediates by Cl• radicals, which inhibit the TOC removal. Furthermore, the participation of the less electronegative Cl• radicals in degradation may reduce mineralization since they are incapable of breaking aromatic rings. Likewise, sulphate ions had the lowest mineralization due to their scavenging effect of h^+, e- and •OH radicals to produce low activity $SO_4•^-$ radicals. Therefore, it can be inferred that competing ions have an influence on both degradation and mineralization. The sulphate anions have the highest inhibition effect for both degradation and TOC removal.

CHAPTER 5

CONCLUSIONS AND RECOMMENDATIONS

5.1 Conclusions

The main aim of the study was to evaluate the degradation of trimethoprim and tetracycline using a dye sensitized composite. The study synthesized four composites of ZF-GCN at 0, 5,15 and 25wt% loading of zinc ferrite followed by dye sensitization. The as-synthesized composites were characterized for structural analyses using XRD and FTIR, morphology and chemical composition using SEM-EDX, and optical-electronic properties using UV-vis and PL-spectra. Central composite design was used in optimizing degradation and TOC removal for both antibiotics. Finally, the effect of competing ions was studied at various salt concentrations (100, 300, 500 mg/l) in real wastewater. Several conclusions were drawn from the study as follows;

1. The as-synthesized composites exhibited both the structural and crystalline phases of g-C_3N_4 and $ZnFe_2O_4$. Furthermore, the composites displayed a reduction in bandgap and suppressed charge recombination. This was evidence of the successful creation of heterojunction. Dye sensitization had no significant effect on optical absorption but improved charge suppression. This may have led to its improved photocatalytic activity.
2. Single factor experiments conducted at the suggested optimum helped validate the RSM values. The actual degradation and %TOC removal for TMP were 87.02% and 46.33%, respectively, while the predicted values were 89.52% and 49.12%, respectively. Similarly, the actual tetracycline degradation and %TOC removal was 94.62% and 68.26%, while the predicted values were 96.02% and 65.25%, respectively. These deviations of the predicted from actual values could be

attributed to changes in environmental conditions. These findings indicate that RSM can be used to model the removal of antibiotics from contaminated wastewater.

3. The initial pH strongly influenced %TOC removal, with the highest removal observed at alkaline pH. Hydroxylation reactions that break the unstable aromatic rings and initiate mineralization reactions could have been responsible. On the other hand, degradation tends to be favored by mild conditions.
4. Real wastewater had lower degradation kinetics for all instances compared to synthetic water. For 10, 20, and 40mg/l pollutant concentrations, the degradation kinetics for SW were 3.1, 1.65 and 1.89 times faster than those for RW. The low degradation rates in real wastewater could be attributed to the presence of competing ions, NOM, high turbidity and undegraded metabolites.
5. Low doses of Cl- and NO3- had a promoting effect on Kapp since at 100mg/l salt concentration, the promotion effect was 0.75% and 5.26%, respectively. At high doses, all the anions inhibited degradation. Consequently, the order of increasing inhibition for the anions was as follows: Cl- < NO3- < SO42-. The high inhibition of SO42- ions could be attributed to a preferential adsorption displacement mechanism. The more electronegative SO42- ions were selectively adsorbed, displacing the OH- anions, hence inhibiting radical formation.

5.2 Recommendations

5.2.1 Recommendation from this study

This research has explored heterogenous photocatalysis as a potential treatment method for remediating antibiotics from water. The following recommendations could be considered:

a. The solar PTR/photocatalyst system explored in this research exhibited a high photocatalytic performance in both synthetic and real wastewater matrices.

Therefore, this system could be used as a tertiary polishing step for municipal wastewater. This would help curb the incessant problem of pharmaceutical residues in treated wastewater.

b. A high concentration of anions was found to severely inhibit the photocatalytic activity of composites in the PTR system. Therefore, the removal of anions before photocatalytic treatment is recommended as a pretreatment step.

5.2.2 Recommendation for future studies

a. The synthesized photocatalysts were not recovered at the end of treatment. Future research should focus on the installation of recovery systems on the PTR reactor.

b. Regression models used in this study were only specific to a particular pollutant. Considering the varied nature of pollutants that exist in real wastewater matrices. Future research should focus on developing mechanistic models suitable for optimizing the degradation of an array of emerging contaminants.

c. Extraneous factors such as environmental-induced conditions like light intensity and temperature may affect the performance of the PTR system. Future research should investigate their effects on the reaction kinetics.

REFERENCES

Abdulrazaq, Y., Abdulsalam, A., Larayetan Rotimi, A., Aliyu Abdulbasit, A., Clifford, O., Abdulazeez Abdulsalam, O., Nayo Racheal, O., Akor Joy, A., Omale Victor, F., Mbese Johannes, Z., Bilal, M., & Umar M, S. (2021). Classification, Potential Routes and Risk of Emerging Pollutants/Contaminant. *Emerging Contaminants*, *December*. https://doi.org/10.5772/intechopen.94447

Abid, M. F., Abdulla, O. N., & Kadhim, A. F. (2019). Journal of King Saud University – Engineering Sciences Study on removal of phenol from synthetic wastewater using solar photo catalytic reactor. *Journal of King Saud University - Engineering Sciences*, *31*(2), 131–139. https://doi.org/10.1016/j.jksues.2017.03.002

Adamek, E., Masternak, E., Sapińska, D., & Baran, W. (2022). Degradation of the Selected Antibiotic in an Aqueous Solution by the Fenton Process: Kinetics, Products and Ecotoxicity. *International Journal of Molecular Sciences*, *23*(24). https://doi.org/10.3390/ijms232415676

Adenuga, D., Skosana, S., Tichapondwa, S., & Chirwa, E. (2021). Synthesis of a plasmonic AgCl and oxygen-rich Bi24O31Cl10composite heterogeneous catalyst for enhanced degradation of tetracycline and 2,4-dichlorophenoxy acetic acid. *RSC Advances*, *11*(58), 36760–36768. https://doi.org/10.1039/d1ra06855e

Adil, S., Maryam, B., Kim, E. J., & Dulova, N. (2020). Individual and simultaneous degradation of sulfamethoxazole and trimethoprim by ozone, ozone/hydrogen peroxide and ozone/persulfate processes: A comparative study. *Environmental Research*, *189*(March), 109889. https://doi.org/10.1016/j.envres.2020.109889

Aghalari, Z., Dahms, H., Sillanpää, M., Sosa-hernandez, J. E., & Parra-saldívar, R. (2020). *Effectiveness of wastewater treatment systems in removing microbial agents : a systematic review*. 1–11.

Ahmed, S., Saleem, F., Khan, A., Mujawar, N., Khalid, M., Hua, Y., Ali, S., Rao, R., & Chan, E. (2021). Journal of Environmental Chemical Engineering Emerging pollutants and their removal using visible-light responsive photocatalysis – A comprehensive review. *Journal of Environmental Chemical Engineering*, *9*(6), 106643. https://doi.org/10.1016/j.jece.2021.106643

Ajala, O. A., & Akinnawo, O. (2023). *Adsorptive removal of antibiotic pollutants from wastewater using biomass/biochar-based adsorbents*. 4678–4712. https://doi.org/10.1039/d2ra06436g

Akbari, M. Z., Xu, Y., Lu, Z., & Peng, L. (2021). Review of antibiotics treatment by advance oxidation processes. *Environmental Advances*, *5*, 100111. https://doi.org/10.1016/j.envadv.2021.100111

Aksu Demirezen, D., Yıldız, Y. Ş., & Demirezen Yılmaz, D. (2019). Amoxicillin degradation using green synthesized iron oxide nanoparticles: Kinetics and mechanism analysis. *Environmental Nanotechnology, Monitoring and Management*, *11*(September 2018). https://doi.org/10.1016/j.enmm.2019.100219

Alalm, M. G., Tawfik, A., & Ookawara, S. (2015). Degradation of four pharmaceuticals by solar photo-Fenton process: Kinetics and costs estimation. *Journal of Environmental Chemical Engineering*, *3*(1), 46–51. https://doi.org/10.1016/j.jece.2014.12.009

Alfred, M. O., Olorunnisola, C. G., Oyetunde, T. T., Dare, P., Vilela, R. R. C., de Camargo, A., Oladoja, N. A., Omorogie, M. O., Olukanni, O. D., Motheo, A. de J., & Unuabonah, E. I. (2022). Sunlight-driven photocatalytic mineralization of antibiotic chemical and selected enteric bacteria in water via zinc tungstate-imprinted kaolinite. *Green Chemistry Letters and Reviews*, *15*(3), 705–723. https://doi.org/10.1080/17518253.2022.2124889

Alnajrani, M. N., & Alsager, O. A. (2020). Removal of Antibiotics from Water by Polymer of Intrinsic Microporosity : Isotherms , Kinetics , Thermodynamics , and Adsorption Mechanism. *Scientific Reports*, 1–14. https://doi.org/10.1038/s41598-020-57616-4

Ameta, R., Solanki, M. S., Benjamin, S., & Ameta, S. C. (2018). *6.1 introduction*. https://doi.org/10.1016/B978-0-12-810499-6.00006-1

Arman, N. Z., Salmiati, S., Aris, A., Salim, M. R., Nazifa, T. H., Muhamad, M. S., & Marpongahtun, M. (2021). *A Review on Emerging Pollutants in the Water Environment : Existences , Health Effects and Treatment Processes*. 1–31.

Attarikhasraghi, N., Zare, K., Mehrizad, A., Modirshahla, N., & Behnajady, M. A. (2021). Achieving the Enhanced Photocatalytic Degradation of Ceftriaxone Sodium Using CdS - g - C 3 N 4 Nanocomposite under Visible Light Irradiation : RSM Modeling and Optimization. *Journal of Inorganic and Organometallic Polymers and Materials*, *0123456789*. https://doi.org/10.1007/s10904-021-01967-6

Azzaz, A. A., Jellali, S., Ben, N., Hamed, H., El, A., Azzaz, A. A., Jellali, S., Ben, N., Hamed, H., Jery, A. El, & Khezami, L. (2021). *Photocatalytic Treatment of Wastewater Containing Simultaneous Organic and Inorganic Pollution : Competition and Operating Parameters Effects To cite this version : HAL Id : hal-03331070 Photocatalytic Treatment of Wastewater Containing Simultaneous Organ*. 0–17.

Balakrishnan, A., Chinthala, M., Kumar, R., & Vo, D. N. (2023). Removal of tetracycline from wastewater using g-C 3 N 4 based photocatalysts : A review. *Environmental Research*, *216*(P3), 114660. https://doi.org/10.1016/j.envres.2022.114660

Basaleh, A. S. (2021). *Construction of mesoporous ZnFe 2 O 4 -g-C 3 N 4 nanocomposites for enhanced photocatalytic degradation of acridine orange dye under visible light illumination adopting soft- and hard- template-assisted routines*. https://doi.org/10.1016/j.jmrt.2021.01.110

Berkani, M., Kadmi, Y., Bouchareb, M. K., Bouhelassa, M., Bouzaza, A., Berkani, M., Kadmi, Y., Bouchareb, M. K., Bouhelassa, M., Berkani, M., Kadmi, Y., & Kheireddine, M. (2021). Combination of a Box-Behnken design technique with response surface methodology for optimization of the photocatalytic mineralization of CI Basic Red 46 dye from aqueous solution To cite this version : HAL Id : hal-03100263 Combinat ı on of a Box-Behnken . *Arabian Journal of Chemistry*, *13*(11), 8338–8346. https://doi.org/10.1016/j.arabjc.2020.05.013

Borthakur, S., & Saikia, L. (2019). *Journal of Environmental Chemical Engineering ZnFe 2 O 4 @ g-C 3 N 4 nanocomposites : An e ffi cient catalyst for Fenton-like photodegradation of environmentally pollutant Rhodamine B*. *7*(March). https://doi.org/10.1016/j.jece.2019.103035

Budi, S., Yulianto, E., Maharani, N., Gunawan, G., Farida, N., Hobley, J., Usman, A., & Nur, M. (2022). *Heliyon Degradation of cipro fl oxacin in aqueous solution using ozone microbubbles : spectroscopic , kinetics , and antibacterial analysis*. *8*(May). https://doi.org/10.1016/j.heliyon.2022.e10137

Carvalho, P. N., Araújo, J. L., Mucha, A. P., Basto, M. C. P., & Almeida, C. M. R. (2013). Potential of constructed wetlands microcosms for the removal of veterinary pharmaceuticals from livestock wastewater. *Bioresource Technology*, *134*, 412–416. https://doi.org/10.1016/j.biortech.2013.02.027

Chakkunny, A. H., Thomas, B., & Alexander, L. K. (2021). Influence of pH and salinity on the photocatalytic dye degradation and heavy metal ion reduction with cobalt ferrite photocatalysts. *IOP Conference Series: Materials Science and Engineering*, *1187*(1), 012018. https://doi.org/10.1088/1757-899x/1187/1/012018

Chen, L., Ma, W., Dai, J., Zhao, J., Li, C., & Yan, Y. (2016). *Journal of Photochemistry and Photobiology A : Chemistry heterostructures enhanced visible-light photocatalysis for spiramycin degradation*. *328*, 24–32.

Chen, Y., Liu, Y., & Ma, Z. (2021). *g-C 3 N 4 Sensitized by an Indoline Dye for Photocatalytic*. 1–15.

Chowdhury, S. R., Alhelal, F., Alahmadi, M., & Alqahtani, N. (2021). *An Overview on Major Design Constraints , Impact and Challenges for a Conventional Wastewater Treatment Design*. *9*(1), 7–16.

Ciğeroğlu, Z., Kazan-Kaya, E. S., El Messaoudi, N., Fernine, Y., Américo-Pinheiro, J. H. P., & Jada, A. (2023). Remediation of tetracycline from aqueous solution through adsorption on g-C3N4-ZnO-BaTiO3 nanocomposite: Optimization, modeling, and theoretical calculation. *Journal of Molecular Liquids*, *369*. https://doi.org/10.1016/j.molliq.2022.120866

Coha, M., Farinelli, G., Tiraferri, A., Minella, M., & Vione, D. (2021). Advanced oxidation processes in the removal of organic substances from produced water: Potential, configurations, and research needs. *Chemical Engineering Journal*, *414*(September 2020), 128668. https://doi.org/10.1016/j.cej.2021.128668

da Silva, S. W., Welter, J. B., Albornoz, L. L., Heberle, A. N. A., Ferreira, J. Z., & Bernardes, A. M. (2021). Advanced Electrochemical Oxidation Processes in the Treatment of Pharmaceutical Containing Water and Wastewater: a Review. *Current Pollution Reports*, *7*(2), 146–159. https://doi.org/10.1007/s40726-021-00176-6

Dai, Z., Zhen, Y., Sun, Y., Li, L., & Ding, D. (2021). ZnFe2O4/g-C3N4 S-scheme photocatalyst with enhanced adsorption and photocatalytic activity for uranium(VI) removal. *Chemical Engineering Journal*, *415*(November 2020). https://doi.org/10.1016/j.cej.2021.129002

Damania, R., Desbureaux, S., Rodella, A.-S., Russ, J., & Zaveri, E. (2019). Quality Unknown. In *Quality Unknown: The Invisible Water Crisis*. https://openknowledge.worldbank.org/handle/10986/32245

Darkwah, W. K., & Ao, Y. (2018). *Mini Review on the Structure and Properties (Photocatalysis), and Preparation Techniques of Graphitic Carbon Nitride Nano-Based Particle , and Its Applications*. *3*.

Deng, Y., Tang, L., Zeng, G., Wang, J., Zhou, Y., Wang, J., Tang, J., Wang, L., & Feng, C. (2018). Journal of Colloid and Interface Science Facile fabrication of mediator-free Z-scheme photocatalyst of phosphorous-doped ultrathin graphitic carbon nitride nanosheets and bismuth vanadate composites with enhanced tetracycline degradation under visible lig. *Journal of Colloid And Interface Science*, *509*, 219–234. https://doi.org/10.1016/j.jcis.2017.09.016

Desye, B., Belete, B., Amare Alemseged, E., Angaw, Y., & Asfaw Gebrezgi, Z. (2022). Evaluation of Waste Stabilization Pond Efficiency and Its Effluent Water Quality: A Case Study of Kito Furdisa Campus, Jimma University, Southwest Ethiopia. *Scientific World Journal*, *2022*. https://doi.org/10.1155/2022/2800034

Diaz-angulo, J., Arce-sarria, A., Mueses, M., Hernandez-ramirez, A., & Machuca-martinez, F. (2019). Materials Science in Semiconductor Processing Analysis of two dye-sensitized methods for improving the sunlight absorption of TiO 2 using CPC photoreactor at pilot scale. *Materials Science in Semiconductor Processing*, *103*(April), 104640. https://doi.org/10.1016/j.mssp.2019.104640

Dong, W., Yang, C., Zhang, L., Su, Q., Zou, X., Xu, W., Gao, X., Xie, K., & Wang, W. (2021). Highly efficient UV/H2O2 technology for the removal of nifedipine antibiotics: Kinetics, coexisting anions and degradation pathways. *PLoS ONE*, *16*(10 October 2021), 1–20. https://doi.org/10.1371/journal.pone.0258483

Doosti, M., Jahanshahi, R., Laleh, S., Sobhani, S., & Sansano, J. M. (2022). Solar light induced photocatalytic degradation of tetracycline in the presence of ZnO/NiFe2O4/Co3O4 as a new and highly efficient magnetically separable photocatalyst. *Frontiers in Chemistry*, *10*(October), 1–17. https://doi.org/10.3389/fchem.2022.1013349

Duc, H. Van, Thi, N., Thu, A., Thi, D., Cam, N., Luyen, N. D., Le, N., Linh, M., Thi, N., Nhung, A., Nhiem, D. N., & Khieu, D. Q. (2023). *Synthesis , characterization , and photocatalytic activity of multicomponent CdMoO 4 / g-C 3 N 4 / GO composite*. *28*(6), 0–3.

Eniola, J. O., Kumar, R., Barakat, M. A., & Rashid, J. (2022). A review on conventional and advanced hybrid technologies for pharmaceutical wastewater treatment. *Journal of Cleaner Production*, *356*(March), 131826. https://doi.org/10.1016/j.jclepro.2022.131826

Eugene-Osoikhia, T. T., & Emesiani, M. C. (2019). Potentiometric Determination of pKa of Some Selected Antibiotics in Mixed Solvent Media. *ChemSearch Journal*, *10*(2), 1–9.

Fast, S. A., Gude, V. G., Truax, D. D., Martin, J., & Magbanua, B. S. (2017). A Critical Evaluation of Advanced Oxidation Processes for Emerging Contaminants Removal. *Environmental Processes*, *4*(1), 283–302. https://doi.org/10.1007/s40710-017-0207-1

Favier, L., Hlihor, R. M., Harja, M., Vial, C., Rakshitha, R., Rajesh, C., Gurupadayya, B., Haridas, S., Devi, K., Xuan, N., Linh, D., Thi, N., Le, H., Cuong, M., Thuy, N., Thi, N., & Ha, T. (2023). Facile Fabrication of α-Fe 2 O 3 / g-C 3 N 4 Z Scheme Heterojunction for Novel Degradation of Residual Tetracycline. *Environmental Science and Pollution Research*, *328*(0123456789), 139–148. https://doi.org/10.1007/s11356-023-27774-9

Felis, E., Buta-hubeny, M., Zieli, W., Hubeny, J., Harnisz, M., Bajkacz, S., & Korzeniewska, E. (2022). *Science of the Total Environment Solar-light driven photodegradation of antimicrobials , their transformation by-products and antibiotic resistance determinants in treated wastewater*. *836*(March). https://doi.org/10.1016/j.scitotenv.2022.155447

Feng, L. (2014). *non-steroidal anti-inflammatory pharmaceuticals from To cite this version : HAL Id : tel-00952080 Processes For The Removal Of Residual Non-Steroidal Anti- Inflammatory Pharmaceuticals From*.

Gálvez, J. B., & Rodríguez, S. M. (n.d.). *SA NE M SC PL O E – C EO AP LS M SC PL O E –. II*.

Gao, B., & Wang, J. (2020). *Enhanced photocatalytic removal of amoxicillin with Ag / TiO 2 / mesoporous g-C 3 N 4 under visible light : property and mechanistic studies*. 7025–7039.

Gao, X., Guo, Q., Tang, G., Peng, W., Luo, Y., & He, D. (2019). *Uncorrected Proof Uncorrected Proof*. 1–9. https://doi.org/10.2166/wrd.2019.001

Garg, A., Kaur, G., Sangal, V. K., Bajpai, P. K., & Upadhyay, S. (2020). *Optimization methodology based on neural networks and box-behnken design applied to photocatalysis of acid red*. *25*(5), 753–762.

Gautam, P., Popat, A., & Lokhandwala, S. (2022). Advances & Trends in Advance Oxidation Processes and Their Applications. *Environmental Science and Engineering*, 45–69. https://doi.org/10.1007/978-3-030-83811-9_3

González, B., Trujillano, R., Vicente, M. A., Rives, V., Korili, S. A., & Gil, A. (2019). Applied Clay Science Photocatalytic degradation of trimethoprim on doped Ti-pillared montmorillonite. *Applied Clay Science*, *167*(September 2018), 43–49. https://doi.org/10.1016/j.clay.2018.10.006

Gorito, A. M., Ribeiro, A. R., Almeida, C. M. R., & Silva, A. M. T. (2017). A review on the application of constructed wetlands for the removal of priority substances and contaminants of emerging concern listed in recently launched EU legislation. *Environmental Pollution*, *227*, 428–443. https://doi.org/10.1016/j.envpol.2017.04.060

Gruchlik, Y., Linge, K., & Joll, C. (2018). Removal of organic micropollutants in waste stabilisation ponds : A review. *Journal of Environmental Management*, *206*, 202–214. https://doi.org/10.1016/j.jenvman.2017.10.020

Guide, A. A. (2005). Celebrating Water for Life 2005-2015 THE INTERNATIONAL DECADE. *Sustainable Development*.

Gusain, R., Kumar, N., & Ray, S. S. (2020). Factors Influencing the Photocatalytic Activity of Photocatalysts in Wastewater Treatment. *Photocatalysts in Advanced Oxidation Processes for Wastewater Treatment*, 229–270. https://doi.org/10.1002/9781119631422.ch8

Haddaoui, I. (2021). *A review on occurrence of emerging pollutants in waters of the MENA region Middle East and North Africa*.

Hanif, R. S. M. A., Javed, A. M. H. M. A., Nadeem, M. Z. N., & Shaheen, G. M. A. (2021). *Sunlight - driven photocatalytic degradation of rhodamine B dye by Ag / FeWO 4 / g - C 3 N 4 composites*. 927–938.

Hartmann, M., Kullmann, S., & Keller, H. (2010). Wastewater treatment with heterogeneous Fenton-type catalysts based on porous materials. *Journal of Materials Chemistry*, *20*(41), 9002–9017. https://doi.org/10.1039/c0jm00577k

Hasija, V., Singh, P., Thakur, S., Stando, K., Nguyen, V. H., Le, Q. Van, Alshehri, S. M., Ahamad, T., Wu, K. C. W., & Raizada, P. (2022). Oxygen doping facilitated N-vacancies in g-C3N4 regulates electronic band gap structure for trimethoprim and Cr (VI) mitigation: Simulation studies and photocatalytic degradation pathways. *Applied Materials Today*, *29*(July), 101676. https://doi.org/10.1016/j.apmt.2022.101676

Hayat, A., Al-sehemi, A. G., El-nasser, K. S., Taha, T. A., Al-ghamdi, A. A., Ali, J., Syed, S., & Amin, M. A. (2021). ScienceDirect Graphitic carbon nitride (g e C 3 N 4) e based semiconductor as a beneficial candidate in photocatalysis diversity. *International Journal of Hydrogen Energy*, *47*(8), 5142–5191. https://doi.org/10.1016/j.ijhydene.2021.11.133

Hazra, M., Joshi, H., Williams, J. B., & Watts, J. E. M. (2022). Chemosphere Antibiotics and antibiotic resistant bacteria / genes in urban wastewater : A comparison of their fate in conventional treatment systems and constructed wetlands. *Chemosphere*, *303*(P2), 135148. https://doi.org/10.1016/j.chemosphere.2022.135148

Hosseini, O., Zare-shahabadi, V., Ghaedi, M., & Azqhandi, M. H. A. (2022). Journal of Environmental Chemical Engineering Experimental design , RSM and ANN modeling of tetracycline photocatalytic degradation using LDH @ CN. *Journal of Environmental Chemical Engineering*, *10*(5), 108345. https://doi.org/10.1016/j.jece.2022.108345

Huang, Q., Zhao, Q., Yang, C., & Jiang, T. (2020). Facile synthesis of mesoporous graphitic carbon nitride / SnO 2 nanocomposite photocatalysts for the enhanced photodegradation of Rhodamine B. *Reaction Kinetics, Mechanisms and Catalysis*, *129*(1), 535–550. https://doi.org/10.1007/s11144-019-01712-8

Huong, T., Hieu, M., Thu, T., Chu, H., Myung, Y., Hoon, S., Mapari, M. G., & Taeyoung, K. (2023). Enhanced photodegradation of tetracycline in wastewater and conversion of CO 2 by solar light assisted ZnO / g-C 3 N 4. *Environmental Research*, *217*(November 2022), 114825. https://doi.org/10.1016/j.envres.2022.114825

Ikehata, K., & Li, Y. (2018). Ozone-Based Processes. *Advanced Oxidation Processes for Wastewater Treatment: Emerging Green Chemical Technology*, 115–134. https://doi.org/10.1016/B978-0-12-810499-6.00005-X

Ismael, M. (2020). A review on graphitic carbon nitride (g-C 3 N 4) based nanocomposites : Synthesis , categories , and their application in photocatalysis. *Journal of Alloys and Compounds*, *846*, 156446. https://doi.org/10.1016/j.jallcom.2020.156446

Jangam, K., Patil, K., Balgude, S., Patange, S., & More, P. (2021). Journal of Physics and Chemistry of Solids Synthesis and characterization of magnetically separable Zn 1-x Co x FeMnO 4 nanoferrites as highly efficient photocatalyst for degradation of dye under solar light irradiation. *Journal of Physics and Chemistry of Solids*, *148*(July 2020), 109700. https://doi.org/10.1016/j.jpcs.2020.109700

Jia, M., Liu, Q., Xiong, W., Yang, Z., & Zhang, C. (2022). *Applied Catalysis B : Environmental Ti 3 + self-doped TiO 2 nanotubes photoelectrode decorated with Ar-Fe 2 O 3 derived from MIL-100 (Fe): Enhanced photo-electrocatalytic performance for antibiotic degradation*. *310*(March).

Jindal, H., Kumar, D., Sillanpaa, M., & Nemiwal, M. (2021). Current progress in polymeric graphitic carbon nitride-based photocatalysts for dye degradation. *Inorganic Chemistry Communications*, *131*(July), 108786. https://doi.org/10.1016/j.inoche.2021.108786

Jo, W., Moru, S., & Tonda, S. (2020). Applied Surface Science Magnetically responsive SnFe 2 O 4 / g-C 3 N 4 hybrid photocatalysts with remarkable visible-light-induced performance for degradation of environmentally hazardous substances and sustainable hydrogen production. *Applied Surface Science*, *506*(December 2019), 144939. https://doi.org/10.1016/j.apsusc.2019.144939

K'oreje, K. O., Kandie, F. J., Vergeynst, L., Abira, M. A., Van Langenhove, H., Okoth, M., & Demeestere, K. (2018). Occurrence, fate and removal of pharmaceuticals, personal care products and pesticides in wastewater stabilization ponds and receiving rivers in the Nzoia Basin, Kenya. *Science of the Total Environment*, *637–638*, 336–348. https://doi.org/10.1016/j.scitotenv.2018.04.331

K'oreje, K. O., Okoth, M., Van Langenhove, H., & Demeestere, K. (2020). Occurrence and treatment of contaminants of emerging concern in the African aquatic environment: Literature review and a look ahead. *Journal of Environmental Management*, *254*(October 2019), 109752. https://doi.org/10.1016/j.jenvman.2019.109752

K, K. O., Vergeynst, L., Ombaka, D., Wispelaere, P. De, & Okoth, M. (2016). Chemosphere Occurrence patterns of pharmaceutical residues in wastewater , surface water and groundwater of Nairobi and Kisumu city , Kenya. *Chemosphere*, *149*, 238–244. https://doi.org/10.1016/j.chemosphere.2016.01.095

kageche, K. D., & kipkirui, E. (2020). Contemporary and emerging pollutants in Nairobi river, Kenya. *International Journal of Scientific and Research Publications (IJSRP)*, *10*(2), p98106. https://doi.org/10.29322/ijsrp.10.02.2020.p98106

Kairigo, P., Ngumba, E., Sundberg, L., Gachanja, A., & Tuhkanen, T. (2020). Science of the Total Environment Occurrence of antibiotics and risk of antibiotic resistance evolution in selected Kenyan wastewaters , surface waters and sediments. *Science of the Total Environment*, *720*, 137580. https://doi.org/10.1016/j.scitotenv.2020.137580

Kamaz, M., Wickramasinghe, S. R., Eswaranandam, S., Zhang, W., Jones, S. M., Watts, M. J., & Qian, X. (2019). Investigation into micropollutant removal from wastewaters by a membrane bioreactor. *International Journal of Environmental Research and Public Health*, *16*(8). https://doi.org/10.3390/ijerph16081363

Kamba, P. F., Kaggwa, B., Munanura, E. I., Okurut, T., & Kitutu, F. E. (2017). Why regulatory indifference towards pharmaceutical pollution of the environment could be a missed opportunity in public health protection. A holistic view. *Pan African Medical Journal*, *27*, 2–5. https://doi.org/10.11604/pamj.2017.27.77.10973

Karpińska, J., & Kotowska, U. (2021). New aspects of occurrence and removal of emerging pollutants. *Water (Switzerland)*, *13*(17). https://doi.org/10.3390/w13172418

Kefeni, K. K., & Mamba, B. B. (2020). Photocatalytic application of spinel ferrite nanoparticles and nanocomposites in wastewater treatment: Review. *Sustainable Materials and Technologies*, *23*, e00140. https://doi.org/10.1016/j.susmat.2019.e00140

Khalil, S., & Shaheen, M. (2011). *Design and manufacturing of parabolic trough solar collector system for a developing country Pakistan*. *December 2015*.

Khan, J. A., Sayed, M., Khan, S., & Shah, N. S. (2020). Advanced oxidation processes for the treatment of contaminants of emerging concern. In *Contaminants of Emerging Concern in Water and Wastewater*. Elsevier Inc. https://doi.org/10.1016/B978-0-12-813561-7.00009-2

Khastoo, H., Hassani, A. H., Mafigholami, R., & Mahmoudkhani, R. (2021). *Comparing the performance of the conventional and fixed - bed membrane bioreactors for treating municipal wastewater*. 997–1004.

Khoshnamvand, N., Mostafapour, F. K., Mohammadi, A., & Faraji, M. (2018). Response surface methodology (RSM) modeling to improve removal of ciprofloxacin from aqueous solutions in photocatalytic process using copper oxide nanoparticles (CuO / UV). *AMB Express*, 0–8. https://doi.org/10.1186/s13568-018-0579-2

Kidd, K. A., & Zoeller, R. T. (2012). *Endocrine Disrupting Chemicals*.

Kudłak, B., Szczepańska, N., Owczarek, K., Mazerska, Z., & Namieśnik, J. (2015). Endocrine Disrupting Compounds – Problems and Challenges. *Emerging Pollutants in the Environment - Current and Further Implications*. https://doi.org/10.5772/60410

Kumar, K., Patnaik, S., Mansingh, S., Behera, A., & Mohanty, A. (2020). *Journal of Colloid and Interface Science Enhanced photocatalytic activities of polypyrrole sensitized zinc ferrite / graphitic carbon nitride n-n heterojunction towards ciprofloxacin degradation , hydrogen evolution and antibacterial studies*. *561*, 551–567. https://doi.org/10.1016/j.jcis.2019.11.030

Kumar, R., & Kumar, P. (2020). *Wastewater Stabilisation Ponds : Removal of Emerging Contaminants*. 344–359.

Kutuzova, A., Dontsova, T., & Kwapinski, W. (2021). Application of tio2-based photocatalysts to antibiotics degradation: Cases of sulfamethoxazole, trimethoprim and ciprofloxacin. *Catalysts*, *11*(6). https://doi.org/10.3390/catal11060728

Le, N., Tri, M., Kim, J., Long, B., Tahtamouni, T. M. Al, Thi, P., Lee, C., Minh, N., & Quang, D. (2019). Journal of Industrial and Engineering Chemistry Ag-doped graphitic carbon nitride photocatalyst with remarkably enhanced photocatalytic activity towards antibiotic in hospital wastewater under solar light. *Journal of Industrial and Engineering Chemistry*, *80*, 597–605. https://doi.org/10.1016/j.jiec.2019.08.037

Lee, H. S., Hur, J., & Shin, H. S. (2020). Enhancing the total organic carbon measurement efficiency for water samples containing suspended solids using alkaline and ultrasonic pretreatment methods. *Journal of Environmental Sciences (China)*, *90*, 20–28. https://doi.org/10.1016/j.jes.2019.11.010

Li, B., Zhang, Y., Duanmu, F., Shen, Y., Shen, Z., & Zhong, S. (2019). *Photochemical & Photobiological Sciences*. 1408–1418. https://doi.org/10.1039/c8pp00387d

Li, M., Chen, M., Ling, S., Lee, J., & Lin, S. (2022a). Facile fabrication of a 2D / 2D CoFe - LDH / g - C 3 N 4 nanocomposite with enhanced photocatalytic tetracycline degradation. *Environmental Science and Pollution Research*, *0123456789*. https://doi.org/10.1007/s11356-022-22554-3

Li, M., Chen, M., Ling, S., Lee, J., & Lin, S. (2022b). *Facile fabrication of a 2D / 2D CoFe - LDH / g - C 3 N 4 nanocomposite with enhanced photocatalytic tetracycline degradation*. *0123456789*.

Lin, Y. P., & Mehrvar, M. (2018). Photocatalytic treatment of an actual confectionery wastewater using Ag/TiO2/Fe2O3: Optimization of photocatalytic reactions using surface response methodology. *Catalysts*, *8*(10), 1–17. https://doi.org/10.3390/catal8100409

Lisa Guppy; kelsey Anderson; Mehta; P.; Nagabhatla; N. and, & M., Q. (2017). *Global Water Crisis : the Facts*. 1–3. http://inweh.unu.edu

Liu, N., Qi, R., Sun, X., & Kawazoe, N. (2022). *Synthesis and characterization of 3D-zeolite – modi fi ed TiO 2 -based photocatalyst with synergistic effect for elimination of organic pollutant in wastewater treatment*. *October*, 1–12. https://doi.org/10.3389/fenvs.2022.1009045

Liu, P., Wu, Z., Fang, Z., & Cravotto, G. (2023). Sonolytic degradation kinetics and mechanisms of antibiotics in water and cow milk. *Ultrasonics Sonochemistry*, *99*(July), 106518. https://doi.org/10.1016/j.ultsonch.2023.106518

Liu, W., He, T., Wang, Y., Ning, G., Xu, Z., Chen, X., Hu, X., Wu, Y., & Zhao, Y. (2020). Synergistic adsorption-photocatalytic degradation effect and norfloxacin mechanism of ZnO/ZnS@BC under UV-light irradiation. *Scientific Reports*, *10*(1), 1–12. https://doi.org/10.1038/s41598-020-68517-x

Liu, Y., Hu, C., & Lo, S. (2021). Comparison of the degradation of multiple amine-containing pharmaceuticals during electroindirect oxidation and electrochlorination processes in continuous system. *Water Research*, *203*(July), 117517. https://doi.org/10.1016/j.watres.2021.117517

Ljubas, D., Jureti, H., & Babi, S. (2023). *applied sciences Photocatalytic Degradation of Pharmaceutical Trimethoprim in Aqueous Solution over Nanostructured TiO 2 Film Irradiated with Simulated Solar Radiation*.

Lovegrove, K., & Pye, J. (2012). Fundamental principles of concentrating solar power (CSP) systems. *Concentrating Solar Power Technology*, 16–67. https://doi.org/10.1533/9780857096173.1.16

Lv, M., Zhang, D., Niu, X., Ma, J., Lin, Z., & Fu, M. (2022). Insights into the fate of antibiotics in constructed wetland systems: Removal performance and mechanisms. *Journal of Environmental Management*, *321*(April), 116028. https://doi.org/10.1016/j.jenvman.2022.116028

Ma, D., Yi, H., Lai, C., Liu, X., Huo, X., An, Z., Li, L., Fu, Y., Li, B., Zhang, M., Qin, L., Liu, S., & Yang, L. (2021). Critical review of advanced oxidation processes in organic wastewater treatment. *Chemosphere*, *275*, 130104. https://doi.org/10.1016/j.chemosphere.2021.130104

Mahhumane, N., Cele, L. M., Muzenda, C., Nkwachukwu, O. V., Koiki, B. A., & Arotiba, O. A. (2022). Enhanced Visible Light-Driven Photoelectrocatalytic Degradation of Paracetamol at a Ternary z-Scheme Heterojunction of Bi2WO6 with Carbon Nanoparticles and TiO2 Nanotube Arrays Electrode. *Nanomaterials*, *12*(14). https://doi.org/10.3390/nano12142467

Marandi, A., Polikarpus, M., & Jõeleht, A. (2013). A new approach for describing the relationship between electrical conductivity and major anion concentration in natural waters. *Applied Geochemistry*, *38*, 103–109. https://doi.org/10.1016/j.apgeochem.2013.09.003

Mareai, B. M., Fayed, M., Ahmed, S., & Ibrahim, W. (2020). Performance comparison of phenol removal in pharmaceutical wastewater by activated sludge and extended aeration augmented with activated carbon. *Alexandria Engineering Journal*, *59*(6), 5187–5196. https://doi.org/10.1016/j.aej.2020.09.048

Marizcal-barba, A., Sanchez-burgos, J. A., Zamora-gasga, V., & Larios, A. P. (2022). *Study of the Response Surface in the Photocatalytic Degradation of Acetaminophen Using TiO 2*. 225–236.

Martínez-orgániz, Á., Elías, J., Bravo, B., Llompart, M., Dagnac, T., & Lamas, J. P. (2021). *Emerging pollutants and antibiotics removed by conventional activated sludge followed by ultraviolet radiation in a municipal wastewater treatment plant in Mexico*. *56*(3), 167–179. https://doi.org/10.2166/wqrj.2021.013

Mecha, A. C., Onyango, M. S., Ochieng, A., Jamil, T. S., Fourie, C. J. S., Momba, M. N. B., Mecha, A. C., Onyango, M. S., Ochieng, A., & Jamil, T. S. (2016). *UV and solar light photocatalytic removal of organic contaminants in municipal wastewater*. *6395*(July). https://doi.org/10.1080/01496395.2016.1178290

Mekonnen, T. B. (2022). *Synthesis and characterization of CdS / CeO 2 Nanocomposite with improved visible-light photocatalytic degradation of methyl orange dye*. 65–74. https://doi.org/10.29328/journal.jpsp.1001077

Minh, N., Quang, D., Long, B., Le, N., Tri, M., & Thao, P. (2019). Journal of Water Process Engineering Noble metal -doped graphitic carbon nitride photocatalyst for enhancement photocatalytic decomposition of antibiotic pollutant in wastewater under visible light. *Journal of Water Process Engineering*, *32*(August), 100954. https://doi.org/10.1016/j.jwpe.2019.100954

Mishra, N., Reddy, R., Kuila, A., Rani, A., Nawaz, A., & Pichiah, S. (2017). A Review on Advanced Oxidation Processes for Effective Water Treatment. *Current World Environment*, *12*(3), 469–489. https://doi.org/10.12944/cwe.12.3.02

Moratalla, Á., Lacasa, E., Cañizares, P., Rodrigo, M. A., & Sáez, C. (2022). Electro-Fenton-Based Technologies for Selectively Degrading Antibiotics in Aqueous Media. *Catalysts*, *12*(6). https://doi.org/10.3390/catal12060602

Mosley, L. (2018). *Causes of high pH in South East wetlands Reid R , Mosley L Goyder Institute for Water Research Technical Report Series No . 15 / 25*. *November*. https://doi.org/10.13140/RG.2.2.10739.78885

Mountassir, E., Mouchtari, E., Claeys-bruno, M., Rafqah, S., Anane, H., Lebarillier, S., Piram, A., Briche, S., Wong-wah-chung, P., Mountassir, E., Mouchtari, E., Claeys-bruno, M., & Rafqah, S. (2022). Optimisation of a photocatalytic water treatment using response surface methodology and quality by design Approach. *International Journal of Environmental Analytical Chemistry*, *00*(00), 1–17. https://doi.org/10.1080/03067319.2021.2012171

Mpatani, F. M., Aryee, A. A., Kani, A. N., Han, R., Li, Z., Dovi, E., & Qu, L. (2021). A review of treatment techniques applied for selective removal of emerging pollutant-trimethoprim from aqueous systems. *Journal of Cleaner Production*, *308*(February), 127359. https://doi.org/10.1016/j.jclepro.2021.127359

Mulwa, F., Li, Z., & Fangninou, F. F. (2021). *Water Scarcity in Kenya : Current Status , Challenges and Future Solutions*. *8*, 1–15. https://doi.org/10.4236/oalib.1107096

Muriuki, C., Kairigo, P., Home, P., Ngumba, E., Raude, J., Gachanja, A., & Tuhkanen, T. (2020). Science of the Total Environment Mass loading , distribution , and removal of antibiotics and antiretroviral drugs in selected wastewater treatment plants in Kenya. *Science of the Total Environment*, *743*, 140655. https://doi.org/10.1016/j.scitotenv.2020.140655

Musa, M., & Gaya, U. I. (2019). *Synthesis of Eosin Y-Sensitized Ag-TiO2 Nano-Hybrid for Optimized Photocatalytic Degradation of Aqueous Caffeine*. *April*. https://doi.org/10.4067/s0717-97072019000104275

Ngigi, A. N., Magu, M. M., & Muendo, B. M. (2020). *Occurrence of antibiotics residues in hospital wastewater , wastewater treatment plant , and in surface water in Nairobi County , Kenya*.

Ngumba, E., Gachanja, A., & Tuhkanen, T. (2016). *Science of the Total Environment Occurrence of selected antibiotics and antiretroviral drugs in Nairobi River Basin , Kenya*. *539*, 206–213. https://doi.org/10.1016/j.scitotenv.2015.08.139

Olatunde, O. C., Kuvarega, A. T., & Onwudiwe, D. C. (2020). Photo enhanced degradation of contaminants of emerging concern in waste water. *Emerging Contaminants*, *6*, 283–302. https://doi.org/10.1016/j.emcon.2020.07.006

Oluwole, A. O., & Olatunji, O. S. (2022). Enhanced photocatalytic degradation of naproxen in aqueous matrices using reduced graphene oxide (rGO) decorated binary BSO / g-C 3 N 4 heterojunction nanocomposites. *Chemical Engineering Journal Advances*, *12*(October), 100417. https://doi.org/10.1016/j.ceja.2022.100417

Otieno, K., Okoth, M., Langenhove, H. Van, & Demeestere, K. (2020). Occurrence and treatment of contaminants of emerging concern in the African aquatic environment : Literature review and a look ahead. *Journal of Environmental Management*, *254*(October 2019), 109752. https://doi.org/10.1016/j.jenvman.2019.109752

Palanivel, B., Jayaraman, V., Ayyappan, C., & Alagiri, M. (2019). *Journal of Water Process Engineering Magnetic binary metal oxide intercalated g-C 3 N 4 : Energy band tuned p-n heterojunction towards Z-scheme photo-Fenton phenol reduction and mixed dye degradation*. *32*(April). https://doi.org/10.1016/j.jwpe.2019.100968

Palanivel, B., & Mani, A. (2020). *Conversion of a Type-II to a Z - Scheme Heterojunction by Intercalation of a 0D Electron Mediator between the Integrative NiFe 2 O 4 / g - C 3 N 4 Composite Nanoparticles : Boosting the Radical Production for Photo-Fenton Degradation*.

Patel, N., Khan, Z. A., Shahane, S., Rai, D., Chauhan, D., Kant, C., & Chaudhary, V. K. (2020). Emerging pollutants in aquatic environment: Source, effect, and challenges in biomonitoring and bioremediation- A review. *Pollution*, *6*(1), 99–113. https://doi.org/10.22059/POLL.2019.285116.646

Patel, S. B., Tripathi, A., & Vyas, A. P. (2021). Environmental Nanotechnology , Monitoring & Management Recent development in the structural modification of graphitic carbon nitride for sustainable photocatalysis : Advances , challenges and opportunities. *Environmental Nanotechnology, Monitoring & Management*, *16*(October), 100589. https://doi.org/10.1016/j.enmm.2021.100589

Peng, H., Xiong, W., Yang, Z., Tong, J., Jia, M., Xiang, Y., Sun, S., & Xu, Z. (2023). Fe3O4-supported N-doped carbon channels in wood carbon form etching and carbonization: Boosting performance for persulfate activating. *Chemical Engineering Journal*, *457*(January), 1–11. https://doi.org/10.1016/j.cej.2023.141317

Pham, T., Jung, S. H., & Kim, T. (2021). Enhanced photodegradation of toxic volatile organic pollutants using Ni-doped graphitic carbon nitride under natural solar light. *Solar Energy*, *224*(March), 18–26. https://doi.org/10.1016/j.solener.2021.05.087

Pretali, L., Fasani, E., & Sturini, M. (2022). Current advances on the photocatalytic degradation of fluoroquinolones: photoreaction mechanism and environmental application. *Photochemical and Photobiological Sciences*, *21*(5), 899–912. https://doi.org/10.1007/s43630-022-00217-z

Priority, H., & Plan, C. (2022). *Kenya_Gws_High_Priority_Country_Plan_2023_1*. 1–9.

PubChem. (1390). *No T □□ □ □□ □□ □□□ □□ .* https://gco.iarc.fr/today/data/factsheets/populations/404-kenya-fact-sheets.pdf

Qu, G. (2019). *A Critical Review of Conventional and Emergency Domestic Sewage Treatment Technology A Critical Review of Conventional and Emergency Domestic Sewage Treatment Technology*. https://doi.org/10.1088/1755-1315/237/2/022037

Rani, C. N., & Karthikeyan, S. (2018). *Photocatalytic degradation of aqueous phenanthrene in a slurry photocatalytic reactor : optimization and modelling*. *115*(9), 1732–1740.

Reid, K. (2020). Global Water Crisis: Facts. *World Vision*. https://www.worldvision.org/clean-water-news-stories/global-water-crisis-facts

Rekhate, C. V., & Srivastava, J. K. (2020). Recent advances in ozone-based advanced oxidation processes for treatment of wastewater- A review. *Chemical Engineering Journal Advances*, *3*, 100031. https://doi.org/10.1016/j.ceja.2020.100031

Renukadevi, S., & Jeyakumari, A. P. (2020). Rational design of ZnFe 2 O 4 / g-C 3 N 4 heterostructures composites for high efficient visible-light photocatalysis for degradation of aqueous organic pollutants. *Inorganic Chemistry Communications*, *118*(April), 108047. https://doi.org/10.1016/j.inoche.2020.108047

Rodr, H., Gamez-jara, A., Cruz-noriega, M. D. La, & Rojas-flores, S. (2022). *Literature Review : Evaluation of Drug Removal Techniques in Municipal and Hospital Wastewater*.

Rong, X., Liu, S., Xie, M., Liu, Z., Wu, Z., Zhou, X., Qiu, X., & Wei, J. (2020). *N 2 photo fi xation by Z-scheme single-layer g-C 3 N 4 / ZnFe 2 O 4 for cleaner ammonia production*. *127*(November 2019). https://doi.org/10.1016/j.materresbull.2020.110853

Rono, N., Kibet, J. K., Martincigh, B. S., Nyamori, V. O., Rono, N., Kibet, J. K., Martincigh, B. S., & Nyamori, V. O. (2020). *A review of the current status of graphitic carbon nitride*. *8436*. https://doi.org/10.1080/10408436.2019.1709414

Rout, P. R., Zhang, T. C., Bhunia, P., & Surampalli, R. Y. (2021). Science of the Total Environment Treatment technologies for emerging contaminants in wastewater treatment plants : A review. *Science of the Total Environment*, *753*, 141990. https://doi.org/10.1016/j.scitotenv.2020.141990

Roy, S., Garg, A., Garg, S., & Tran, T. A. (2022). Advanced Industrial Wastewater Treatment and Reclamation of Water. In S. Roy, A. Garg, S. Garg, & T. A. Tran (Eds.), *Environmental Science and Engineering* (Issue January, pp. 197–209). Springer International Publishing. https://doi.org/10.1007/978-3-030-83811-9

Saeed, H., Nadeem, N., & Zahid, M. (2021). Mixed metal ferrite (Mn 0 . 6 Zn 0 . 4 Fe 2 O 4) intercalated g-C 3 N 4 nanocomposite : ef fi cient sunlight driven photocatalyst for methylene blue degradation. *Nanotechnology*, *32*(50), 505714. https://doi.org/10.1088/1361-6528/ac2847

Samy, M., Ibrahim, M. G., Gar Alalm, M., Fujii, M., Ookawara, S., & Ohno, T. (2020a). Photocatalytic degradation of trimethoprim using S-TiO2 and Ru/WO3/ZrO2 immobilized on reusable fixed plates. *Journal of Water Process Engineering*, *33*(October 2019), 3–10. https://doi.org/10.1016/j.jwpe.2019.101023

Samy, M., Ibrahim, M. G., Gar Alalm, M., Fujii, M., Ookawara, S., & Ohno, T. (2020b). Photocatalytic degradation of trimethoprim using S-TiO2 and Ru/WO3/ZrO2 immobilized on reusable fixed plates. *Journal of Water Process Engineering*, *33*(September 2019), 3–10. https://doi.org/10.1016/j.jwpe.2019.101023

Sengupta, A., Jebur, M., Kamaz, M., & Wickramasinghe, S. R. (2022). Removal of Emerging Contaminants from Wastewater Streams Using Membrane Bioreactors: A Review. *Membranes*, *12*(1), 1–25. https://doi.org/10.3390/membranes12010060

Sgroi, M., Pelissari, C., Roccaro, P., Sezerino, P. H., García, J., Vagliasindi, F. G. A., & Ávila, C. (2018). Removal of organic carbon, nitrogen, emerging contaminants and fluorescing organic matter in different constructed wetland configurations. *Chemical Engineering Journal*, *332*(September 2017), 619–627. https://doi.org/10.1016/j.cej.2017.09.122

Shakhawat, M. K. (2022). *Natural Organic Matter (NOM) Precursors Characterization in Source Water by Surrogate Measurements and Disinfection Byproducts (DBPs) Analysis*. 60.

Shan, J., Wu, X., Li, C., Hu, J., Zhang, Z., Liu, H., & Xia, P. (2022). *Photocatalytic degradation of tetracycline hydrochloride by a - Fe 3 O 4 / g - C 3 N 4 / rGO magnetic nanocomposite mechanism : modeling and optimization*.

Shukla, R., & Ahammad, S. Z. (2023). Science of the Total Environment Performance assessment of a modi fi ed trickling fi lter and conventional activated sludge process along with tertiary treatment in removing emerging pollutants from urban sewage. *Science of the Total Environment*, *858*(September 2022), 159833. https://doi.org/10.1016/j.scitotenv.2022.159833

Silva, G., Silva, M. T., Barros, M. A., Sampaio, M. J., Ribeiro, A. R., & Faria, J. L. (2021). *Journal of Environmental Chemical Engineering Interactions of pharmaceutical compounds in water matrices under visible-driven photocatalysis*. *9*(September 2020). https://doi.org/10.1016/j.jece.2020.104747

Song, C., Li, X., Wang, L., & Shi, W. (2016). Fabrication , Characterization and Response Surface Method (RSM) Optimization for Tetracycline. *Nature Publishing Group*, *November*, 1–12. https://doi.org/10.1038/srep37466

Sonu, Sharma, S., Dutta, V., Raizada, P., Hosseini-Bandegharaei, A., Thakur, V., Nguyen, V. H., Vanle, Q., & Singh, P. (2021). An overview of heterojunctioned ZnFe2O4photocatalyst for enhanced oxidative water purification. *Journal of Environmental Chemical Engineering*, *9*(5), 105812. https://doi.org/10.1016/j.jece.2021.105812

Souza, D. M., Reichert, J. F., & Ramos, V. (2022). Toxic / Hazardous Substances and Environmental Engineering Ozonation and UV photolysis for removing anticancer drug residues from hospital wastewater. *Journal of Environmental Science and Health, Part A*, *57*(8), 635–644. https://doi.org/10.1080/10934529.2022.2099195

Su, F., Li, P., Huang, J., Gu, M., Liu, Z., & Xu, Y. (2021). Photocatalytic degradation of organic dye and tetracycline by ternary Ag2O/AgBr–CeO2 photocatalyst under visible-light irradiation. *Scientific Reports*, *11*(1), 1–13. https://doi.org/10.1038/s41598-020-76997-0

Sun, W., Meng, S., Zhang, S., Zheng, X., Ye, X., Fu, X., & Chen, S. (2018). Insight into the Transfer Mechanisms of Photogenerated Carriers for Heterojunction Photocatalysts with the Analogous Positions of Valence Band and Conduction Band: A Case Study of ZnO/TiO2. *Journal of Physical Chemistry C*, *122*(27), 15409–15420. https://doi.org/10.1021/acs.jpcc.8b03753

Suresh, R., Rajendran, S., Kumar, P. S., Vo, D. N., & Cornejo-ponce, L. (2021). Chemosphere Recent advancements of spinel ferrite based binary nanocomposite photocatalysts in wastewater treatment. *Chemosphere*, *274*, 129734. https://doi.org/10.1016/j.chemosphere.2021.129734

Tanwar, R., & Mandal, U. K. (2019). RSC Advances Photocatalytic activity of role and degradation kinetics interpretation †. *RSC Advances*, *9*, 8977–8993. https://doi.org/10.1039/C9RA00548J

Teodosiu, C., Gilca, A., Barjoveanu, G., & Fiore, S. (2018). Emerging pollutants removal through advanced drinking water treatment : A review on processes and environmental performances assessment. *Journal of Cleaner Production*, *197*, 1210–1221. https://doi.org/10.1016/j.jclepro.2018.06.247

Thomas, N., Dionysiou, D. D., & Pillai, S. C. (2021). Heterogeneous Fenton catalysts : A review of recent advances. *Journal of Hazardous Materials*, *404*(PB), 124082. https://doi.org/10.1016/j.jhazmat.2020.124082

Tiejun, Q. (2022). *Pharmaceuticals and drinking water*. https://www.mwra.com/04water/html/pharmaceuticals.htm

Trang, N. H., Thi, T., Ha, V., Viet, N. M., & Phuong, N. M. (2021). *Synthesis , Characterization , and Photocatalytic Activity of*. *2021*, 1–10.

Tripathi, S., & Hussain, T. (2021). Water and Wastewater Treatment through Ozone-based technologies. *Development in Wastewater Treatment Research and Processes: Removal of Emerging Contaminants from Wastewater through Bio-Nanotechnology*, 139–172. https://doi.org/10.1016/B978-0-323-85583-9.00015-6

unicef. (2020). *Water, Sanitation and Hygiene*. https://www.unicef.org/kenya/water-sanitation-and-hygiene#:~:text=59%25 of people in Kenya,villages as open defecation free.

Ur, M., Yaqub, U., Hussain, T., & Nadeem, N. (2021). *Solar driven photocatalytic degradation potential of novel graphitic carbon nitride based nano zero-valent iron doped bismuth ferrite ternary composite*. *120*(July).

USAID Global Waters. (2020). *Water for the World Country Plan: D. R. Congo*. *August 2020*, 1–6. https://www.globalwaters.org/sites/default/files/wfw_drc_country-plan.pdf

Vidyasagar, D., Ghugal, S. G., Kulkarni, A., Shende, A. G., Umare, S. S., & Sasikala, R. (2018). *driven photocatalysis †*. 6322–6331. https://doi.org/10.1039/c8nj00444g

Vliet, M. T. H. Van, Jones, E. R., Flörke, M., Franssen, W. H. P., & Hanasaki, N. (2021). *Global water scarcity including surface water quality and expansions of clean water technologies OPEN ACCESS Global water scarcity including surface water quality and expansions of clean water technologies*.

Waleng, N. J., & Nomngongo, P. N. (2022). Occurrence of pharmaceuticals in the environmental waters: African and Asian perspectives. *Environmental Chemistry and Ecotoxicology*, *4*(November 2021), 50–66. https://doi.org/10.1016/j.enceco.2021.11.002

Wang, L., Wang, K., He, T., Zhao, Y., Song, H., & Wang, H. (2020). Graphitic carbon nitride-based photocatalytic materials: Preparation strategy and application. *ACS Sustainable Chemistry and Engineering*, *8*(43), 16048–16085. https://doi.org/10.1021/acssuschemeng.0c05246

Wu, C. J., Valerie Maggay, I., Chiang, C. H., Chen, W., Chang, Y., Hu, C., & Venault, A. (2023). Removal of tetracycline by a photocatalytic membrane reactor with MIL-53(Fe)/PVDF mixed-matrix membrane. *Chemical Engineering Journal*, *451*(P4), 138990. https://doi.org/10.1016/j.cej.2022.138990

Xie, X., Li, S., Zhang, H., Wang, Z., & Huang, H. (2019). Promoting charge separation of biochar-based Zn-TiO 2 /pBC in the presence of ZnO for efficient sulfamethoxazole photodegradation under visible light irradiation. *Science of the Total Environment*, *659*, 529–539. https://doi.org/10.1016/j.scitotenv.2018.12.401

Xu, S., Zhu, H., Cao, W., Wen, Z., Wang, J., François-xavier, C. P., & Wintgens, T. (2018). *Applied Catalysis B : Environmental simultaneous enhancement of Fenton-like catalytic activity and selective H 2 O 2 conversion to hydroxyl radicals*. *234*(April), 223–233. https://doi.org/10.1016/j.apcatb.2018.04.029

Yan, Q., Xu, Y., Yu, Y., Zhu, Z. W., & Feng, G. (2018). Effects of pharmaceuticals on microbial communities and activity of soil enzymes in mesocosm-scale constructed wetlands. *Chemosphere*, *212*, 245–253. https://doi.org/10.1016/j.chemosphere.2018.08.059

Yang, B., Dai, J., Zhao, Y., Wang, Z., Wu, J., Ji, C., Zhang, Y., & Pu, X. (2023). Synergy effect between tetracycline and Cr(VI) on combined pollution systems driving biochar-templated Fe3O4@SiO2/TiO2/g-C3N4 composites for enhanced removal of pollutants. *Biochar*, *5*(1), 1–20. https://doi.org/10.1007/s42773-022-00197-4

Yin, H., Cao, Y., Fan, T., Li, P., & Liu, X. (2021). Construction of AgBr / β -Ag 2 WO 4 / g-C 3 N 4 ternary composites with dual Z-scheme band alignment for efficient organic pollutants removal. *Separation and Purification Technology*, *272*(October 2020), 118251. https://doi.org/10.1016/j.seppur.2020.118251

Yn, Tan; Chen, Sau Soon; Bakar, Izham; Abdullah, Z. F. (2013). Solar Photocatalytic Decontamination And Disinfection Of Water. *Journal of Industrial Technology*. https://doi.org/DOI:10.21908/jit.2013.8

You, H. (2016). Synthesis, Characterization and Visible Photocatalytic Performance of Iron (III) Tetracarboxyphthalocyanine-Sensitized TiO2 Photocatalyst. *Journal of Physical Chemistry & Biophysics*, *6*(1), 2–6. https://doi.org/10.4172/2161-0398.1000199

Zare, M. H., & Zeinabad, A. M. (2022). Photocatalytic activity of - for the degradation of naproxen : characterization and optimization using response surface methodology. *Scientific Reports*. https://doi.org/10.1038/s41598-022-14676-y

Zhang, D., & Wang, F. (2018). *Investigation on enhanced photocatalytic degradation of bisphenol A with bismuth oxyiodide catalyst using response surface methodology †*. 5967–5975. https://doi.org/10.1039/c7ra13460f

Zhang, S., Ren, H., Fu, K., Cheng, W., Wu, D., Luo, C., Jiang, S., Li, J., & Zhang, M. (2022). Preparation of Mn/Mg/Ce Ternary Ozone Catalyst and Its Mechanism for the Degradation of Printing and Dyeing Wastewater. *Frontiers in Energy Research*, *9*(January), 1–8. https://doi.org/10.3389/fenrg.2021.815633

Zhao, Y., Qin, H., Wang, Z., Wang, H., He, Y., Tian, Q., Luo, Q., & Xu, P. (2022). Facile synthesis of cadmium - doped graphite carbon nitride for photocatalytic degradation of tetracycline under visible light irradiation. *Environmental Science and Pollution Research*, 74062–74080. https://doi.org/10.1007/s11356-022-21051-x

Zhou, W., Yang, B., Liu, G., Xu, C., Ji, Q., Xiang, W., & Sun, D. (2022). Journal of Colloid and Interface Science Perylene diimide supermolecule (PDI) as a novel and highly efficient cocatalyst for photocatalytic degradation of tetracycline in water : A case study of PDI decorated graphitic carbon nitride / bismuth tungstate. *Journal of Colloid And Interface Science*, *615*, 849–864. https://doi.org/10.1016/j.jcis.2022.02.003

APPENDICES

Appendix I: Design specifications of solar parabolic trough collector

a) Parabola design equations and specifications

The parabolic cross-section was modelled using Parabolic calculator software and AutoCAD. The x and y values were verified by the parabolic trough equation $x^2 = 4fy$ where f=focal point.

The geometric concentration ratio (CR) was calculated by the equation $C = \frac{D}{\pi d}$ where D = parabola width, d = collector tube diameter (Gálvez & Rodríguez, n.d.; Khalil & Shaheen, 2011; Yn, Tan; Chen, Sau Soon; Bakar, Izham; Abdullah, 2013).

The rim angle was obtained from the formulae $tan\emptyset = \frac{W/2}{f - Z_R}$ where w=width of receiver, f=focal point and Z_R=Depth of parabola at rim (Lovegrove & Pye, 2012).

Figure I.1: Parabola Dimensions using Parabola Calculator

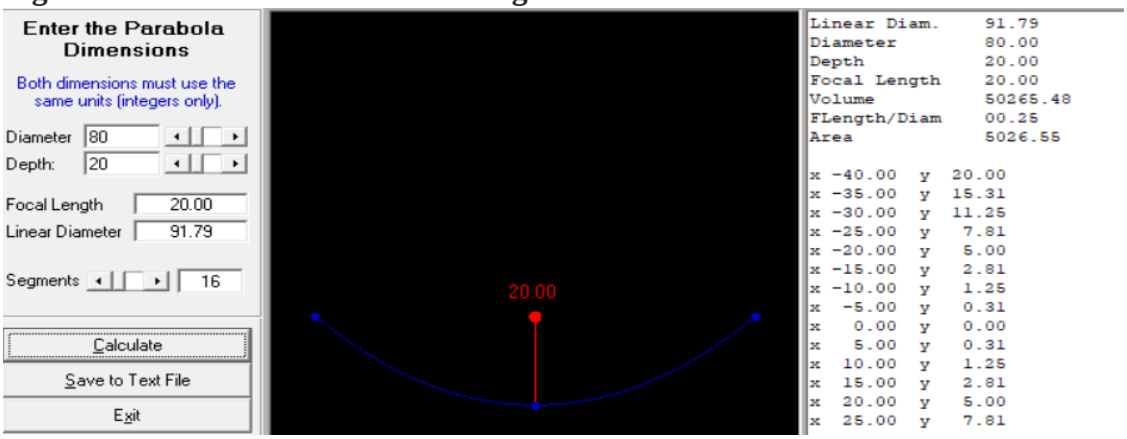

Table I.1: Specifications of the Parabolic Trough Reactor

Parameter	
Absorber tube dimensions(Ø*thickness*L)	2.54cm*0.16cm*100cm
Absorber tube material	Borosilicate glass
Focal point	20cm
Rim angle	90^o
Reflector dimensions (W*Depth*L)	80cm*20cm*80cm
Concentration ratio	8.48
Reflector Area	8261.1cm^2
Reflector material	Aluminum sheet riveted on mild steel support
Aluminum Reflectivity	85%
Metal stand dimensions (L*w*h)	82.50cm*40cm*55.25cm
Metal stand material	Mild Steel

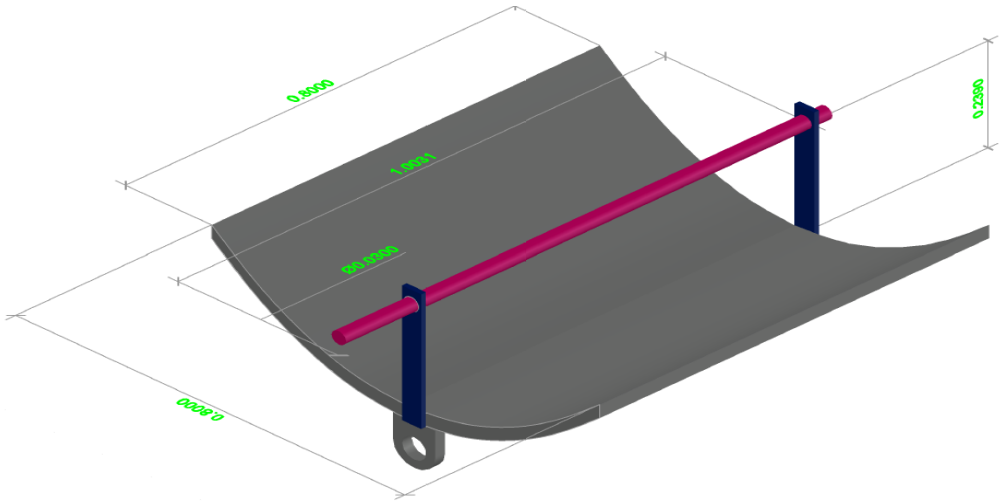

Figure I.2: AutoCAD model of the PTR with the design specifications

b) Fabrication of the Solar PTR

The solar PTR was fabricated at Nairobi Technical Training Institute mechanical workshops based on the design specifications in Table I.1. The framework was constructed from mild steel, with aluminum riveted on the framework to form a parabolic reflector of area 8261.1cm^2. The absorber tube used was made from borosilicate glass of diameter 1 inch and length 90cm. A rectangular mild steel framework fitted with roller wheels was used as the support. Figure I.3, shows the completed setup degrading a model pollutant.

Figure I.3: Completed PTR setup degrading pollutant

Appendix II: Pseudo-second order kinetics for Pollutant degradation

Table I.2: Second Order fitting Data for Tetracycline Degradation for various Photocatalysts

Equation	**y = a + b*x**						
Plot	**5%ZF-GCN**	**15%ZF-GCN**	**25%ZF-GCN**	**Sensitized**	**g-C_3N_4**	**$ZnFe_2O_4$**	**Anatase**
Weight	No Weighting						
Intercept	0.09296 ± 0.02547	0.09196 ± 0.05266	0.1773 ± 0.04218	0.12798 ± 0.06404	0.0265 ± 0.007	0.06779 ± 0.01054	0.02828 ± 0.03559
K_{app} Constant	0.00504 ± 5.02851E-4	0.00916 ± 0.00104	0.01491 ± 8.3287E-4	0.01668 ± 0.00126	0.00101 ± 1.38155E-4	0.00312 ± 2.0821E-4	0.00538 ± 7.02719E-4
Residual Sum of Squares	0.0056	0.02393	0.01536	0.0354	4.22581E-4	9.59797E-4	0.01093
Pearson's r	0.9854	0.98123	0.99535	0.99149	0.97296	0.9934	0.97538
R-Square (COD)	0.97101	0.9628	0.99072	0.98305	0.94665	0.98684	0.95137
Adj. R-Square	0.96135	0.9504	0.98763	0.9774	0.92886	0.98245	0.93515

Table I.3: Pseudo-second order fitting data for degradation at different tetracycline concentration in real wastewater

Equation	**y = a + b*x**			
Plot	**10mg/l-rW**	**10mg/l-rW**	**20mg/l-rW**	**40mg/l-rW**
Weight	No Weighting			
Intercept	0.05764 ± 0.01949	0.05764 ± 0.01949	0.02351 ± 0.00246	0.00975 ± 0.0019
Slope (K_{app})	0.00519 ± 3.84768E-4	0.00519 ± 3.84768E-4	0.00133 ± 4.85728E-5	5.16804E-4 ± 3.75605E-5
Residual Sum of Squares	0.00328	0.00328	5.22352E-5	3.1235E-5
Pearson's r	0.99185	0.99185	0.99802	0.99217
R-Square (COD)	0.98377	0.98377	0.99604	0.9844
Adj. R-Square	0.97837	0.97837	0.99472	0.9792

Table I.4: Pseudo-second order fitting data for performance of various composites in real wastewater

Equation	**y = a + b*x**						
Plot	**5%ZF-GCN-rW**	**15%ZF-GCN-rW**	**25%ZF-GCN-rW**	**Sensitized-rW**	**g-C_3N_4-rW**	**$ZnFe_2O_4$-rW**	**Anatese-rW**
Weight	No Weighting						
Intercept	0.03741 ± 0.02018	0.04963 ± 0.0098	0.06938 ± 0.02261	0.05764 ± 0.01949	0.0097 ± 0.00248	0.02374 ± 0.01047	0.03304 ± 0.01767
Slope (K_{app})	0.00427 ± 3.98515E-4	0.00444 ± 1.93538E-4	0.00462 ± 4.4641E-4	0.00519 ± 3.84768E-4	9.65867E-4 ± 4.90267E-5	0.00244 ± 2.06766E-4	0.00325 ± 3.48975E-4
Residual Sum of Squares	0.00352	8.29299E-4	0.00441	0.00328	5.32162E-5	9.46534E-4	0.0027
Pearson's r	0.98718	0.99717	0.98631	0.99185	0.99616	0.98944	0.98315
R-Square (COD)	0.97452	0.99434	0.9728	0.98377	0.99233	0.97898	0.96658
Adj. R-Square	0.96603	0.99245	0.96374	0.97837	0.98977	0.97198	0.95544

Table I.5: Pseudo-second order fitting data for degradation at different Cl^- concentrations

Equation	**y = a + b*x**			
Plot	**100mg/l-Cl^-**	**300mg/l-Cl^-**	**500mg/l-Cl^-**	**0mg/l-rW**
Weight	No Weighting			
Intercept	0.02738 ± 0.008	0.02749 ± 0.00687	0.02335 ± 0.00639	0.02351 ± 0.00246
Slope (K_{app})	0.00134 ± 1.57975E-4	0.00116 ± 1.35628E-4	0.0011 ± 1.26196E-4	0.00133 ± 4.85728E-5
Residual Sum of Squares	5.5253E-4	4.07264E-4	3.52587E-4	5.22352E-5
Pearson's r	0.97991	0.98018	0.9809	0.99802
R-Square (COD)	0.96022	0.96075	0.96217	0.99604
Adj. R-Square	0.94696	0.94767	0.94956	0.99472

Table I.6: Pseudo-second order fitting data for degradation at different NO_3^- concentrations

Equation	**y = a + b*x**			
Plot	**100mg/l-NO_3^-**	**300mg/l-NO_3^-**	**500mg/L-NO_3^-**	**0mg/l-rW**
Weight	No Weighting			
Intercept	0.01677 ± 0.00745	0.01505 ± 0.00325	0.01427 ± 0.00438	0.02351 ± 0.00246
Slope (K_{app})	0.0014 ± 1.47184E-4	8.22917E-4 ± 6.42552E-5	6.71528E-4 ± 8.649E-5	0.00133 ± 4.85728E-5
Residual Sum of Squares	4.79622E-4	9.141E-5	1.65619E-4	5.22352E-5
Pearson's r	0.98385	0.99098	0.97601	0.99802
R-Square (COD)	0.96797	0.98204	0.95259	0.99604
Adj. R-Square	0.95729	0.97605	0.93679	0.99472

Table I.7: Pseudo-second order fitting data for degradation at different SO_4^{2-} concentrations

Equation	**y = a + b*x**			
Plot	**100mg/l-SO_4^{2-}**	**300mg/l-SO_4^{2-}**	**500mg/l-SO_4^{2-}**	**0mg/l-rW**
Weight	No Weighting			
Intercept	0.01029 ± 0.0039	0.00873 ± 0.00139	0.00612 ± 0.00189	0.02351 ± 0.00246
Slope (K_{app})	0.00102 ± 7.69503E-5	6.6E-4 ± 2.73678E-5	5.66618E-4 ± 3.73492E-5	0.00133 ± 4.85728E-5
Residual Sum of Squares	1.31099E-4	1.65828E-5	3.08844E-5	5.22352E-5
Pearson's r	0.99149	0.99743	0.99355	0.99802
R-Square (COD)	0.98306	0.99487	0.98713	0.99604
Adj. R-Square	0.97741	0.99316	0.98284	0.99472

Appendix III: Experimental Photographs

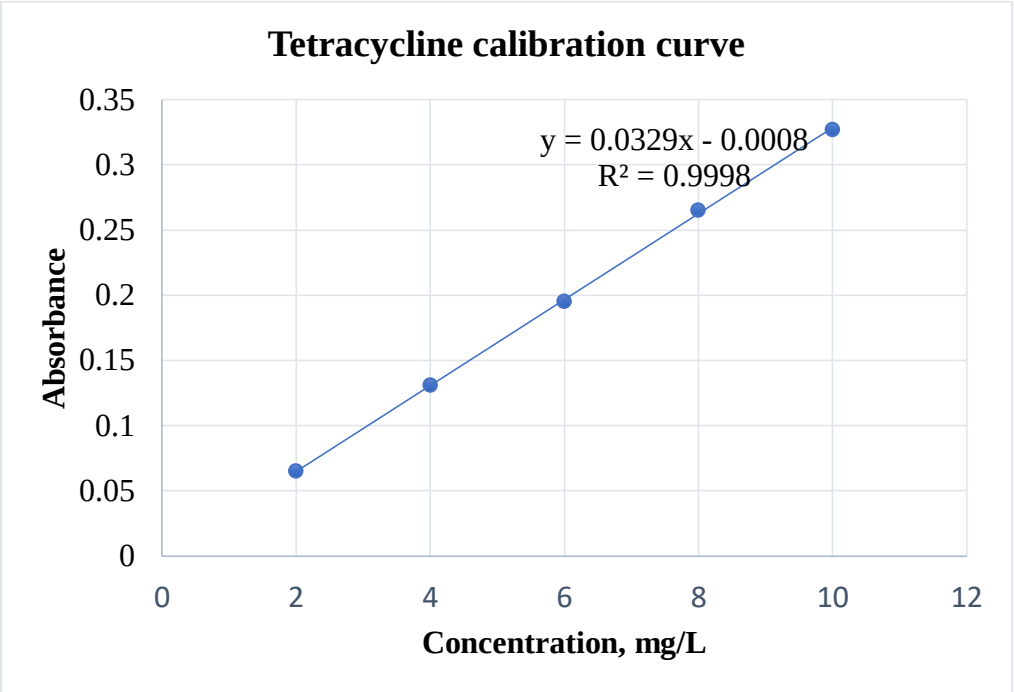

Figure I.4: Tetracycline calibration curve

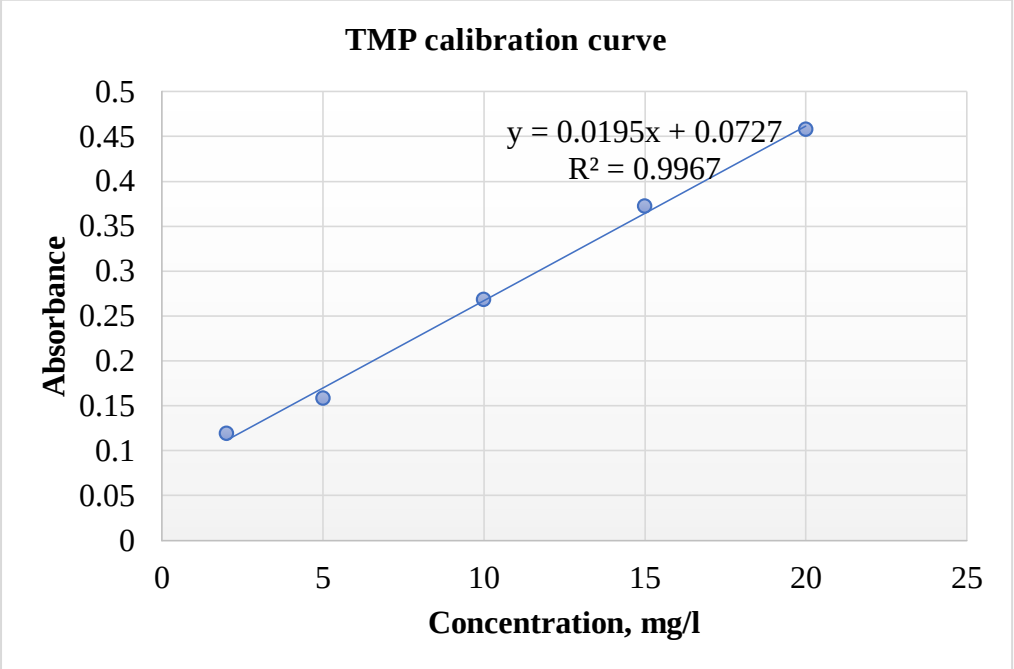

Figure I.5: Trimethoprim calibration curve

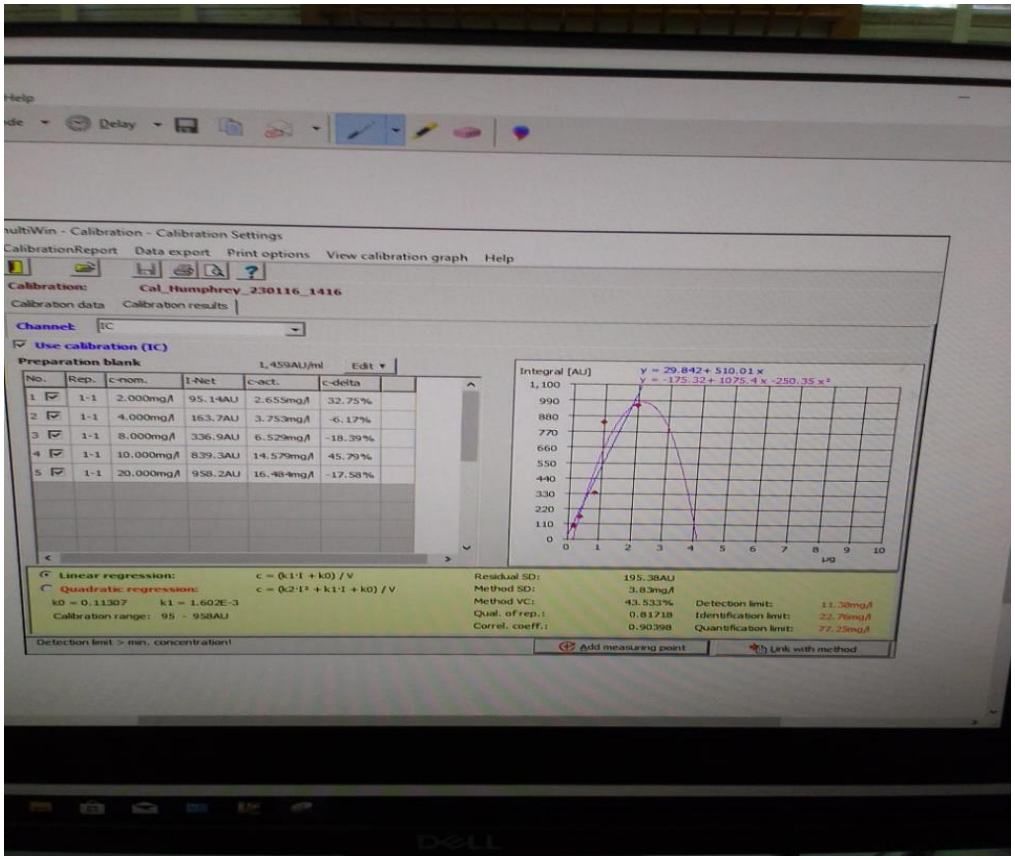

Figure I.6: TOC calibration curve

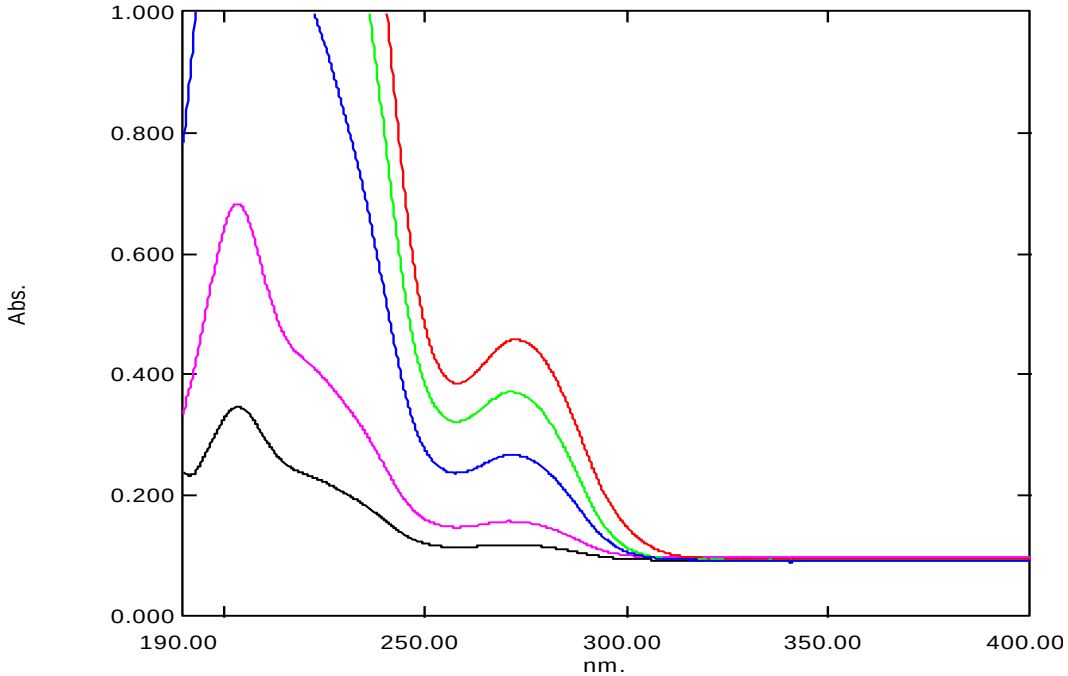

Figure I.7: Decrease of TMP absorbance at different time intervals in the UV-Vis Spectra

Appendix IV: Plagiarism Report

SR349

ISO 9001:2019 Certified Institution

THESIS WRITING COURSE

PLAGIARISM AWARENESS CERTIFICATE

This certificate is awarded to

Mutuma Humphrey Samuel

MSC/CE/5519/21

In recognition for passing the University's plagiarism

Awareness test for Thesis entitled: **PHOTODEGRADATION OF TETRACYCLINE & TRIMETHOPRIM IN WASTEWATER USING SENSITIZED GRAPHITE CARBON NITRIDE AND ZINC FERRITE COMPOSITE** with a similarity index of 1% and striving to maintain academic integrity.

Word count: 34527

Awarded by

Prof. Anne Syomwene Kisilu
CERM-ESA Project Leader Date: 26/10/2023